

2017

3D Building Model-Assisted Snapshot GNSS Positioning Method

Kumar, Rakesh

Kumar, R. (2017). 3D Building Model-Assisted Snapshot GNSS Positioning Method (Doctoral thesis, University of Calgary, Calgary, Canada). Retrieved from <https://prism.ucalgary.ca>. doi:10.11575/PRISM/24620
<http://hdl.handle.net/11023/3666>

Downloaded from PRISM Repository, University of Calgary

UNIVERSITY OF CALGARY

3D Building Model-Assisted Snapshot GNSS Positioning Method

by

Rakesh Kumar

A THESIS

SUBMITTED TO THE FACULTY OF GRADUATE STUDIES
IN PARTIAL FULFILMENT OF THE REQUIREMENTS FOR THE
DEGREE OF DOCTOR OF PHILOSOPHY

GRADUATE PROGRAM IN GEOMATICS ENGINEERING

CALGARY, ALBERTA

MARCH, 2017

© Rakesh Kumar 2017

Abstract

Global Navigation Satellite Systems (GNSS) have proven to be a viable and reliable solution in interference-free environments and in presence of Line-of-Sight (LOS) signals only. However, in urban canyons, multipath signals directly affect the pseudorange measurements resulting in degraded positioning performance of traditional GNSS receivers. Moreover, traditional GNSS receivers cannot distinguish between non-LOS (NLOS) and LOS signals, resulting in even worse performance if the receiver tracks NLOS-only signal. Hence, NLOS and multipath signals remains a dominant source of error in satellite-based navigation.

Most of the existing research has focused on identifying and rejecting NLOS measurements. However, little research has used NLOS signals constructively. In this regard, this research uses snapshots of GNSS data in order to estimate position, utilizing all NLOS signals constructively with the help of a 3D Building Model (3DBM).

Using a 3DBM and a ray-tracing algorithm, the number of reception paths and the corresponding path delays of reflected signals is predicted across a grid of candidate positions. These predictions are then used to compute least-squares fit to the GNSS receiver's correlator outputs and the position with smallest residuals is selected as the position estimate. This approach is termed Signal Delay Matching (SDM) and yields a solution that is nearly unaffected by traditional GNSS error sources, and has capability of providing a position solution using a single satellite only.

The use of snapshots of data mean the receiver need not perform tracking operations, thus making it easier to implement and power efficient.

The feasibility and performance of the algorithm was tested using data collected in downtown Calgary, Canada, where buildings reach heights of over 200 m. Contrary to traditional approaches, results for the proposed method show that positioning error decreases as sky-visibility decreases. For sky-visibility below 20%, the median error was found to be just over 3 m. Compared to two pseudorange-based receivers, the proposed method yields RMS errors improvements of 22% to 48% in the horizontal plane.

Acknowledgements

This dissertation is not only a reflection of myself but also many others who have helped and motivated me directly or indirectly, throughout my studies. Although I am unable to thank each and every one explicitly, their help is embedded inherently in the dissertation.

First and foremost, I would like to express my sincere gratitude to my supervisor, Professor Mark Petovello for his professional guidance and continuous encouragement throughout my journey. Without his motivation and guidance, it would not have been possible to complete my program successfully.

I would also like to express my gratitude to Professor Gérard Lachapelle, Professor Kyle O’Keefe from PLAN group and Professor Ayman Habib (now at Purdue university), for their advice.

My sincere thanks to all current and past post-doctoral fellows of PLAN group and staff members of Geomatics engineering for their help. Special thanks to Ali Broumandan, Negin Sokhandan, Vijay Bellad, Vimalkumar Bhandari, Thayagaraja Marathe, Peng Xie, Srinivas Bhaskar, Naveen Goudayyanadoddi, Zhe He, Paul Gakne, Chnadra Tjhai, and Sashidharan Maa for their help during several data collections and reviewing my thesis chapters and research papers.

Thanks to Vijay & Suvarna, Naveen & Ashwitha, Vimal & Aruna, Niranjana & Shruthi, Thyagaraja & Pavana, Ranjeeth & Kavya, Sashidharan, and Srinivas Tantre, for their wonderful support. Thanks to Rasika & Billy, JingJing, Boxing, Bernhard, Anup, Sergey, Erin, Maryam,

Nahal & Ahmad, Ali P, and Asal for their friendship and for making my stay at PLAN Group memorable.

Finally, this research would not have been possible without the blessings and unconditional love of my parents, my wife, my sisters and in-laws.

The financial support of Alberta Innovate Technology Future (AITF) is also much appreciated.

Dedicated to my parents.

For their unconditional love, support and guidance.

Table of Contents

Abstract	ii
Acknowledgements	iv
Table of Contents	vii
List of Tables	x
List of Figures and Illustrations	xi
CHAPTER ONE: INTRODUCTION	1
1.1 Navigation and Global Navigation Satellite System	1
1.2 GNSS in Urban Canyons: Challenges of Multipath	4
1.2.1 Antenna/hardware-based Technologies	6
1.2.2 Signal Processing Technologies	7
1.2.3 Integration of GNSS and Dead Reckoning System	10
1.2.4 GNSS Aiding With 3D Building Models	14
1.3 Motivation	17
1.4 Objectives	19
1.5 Novelty and Contributions	20
1.5.1 Novelties	20
1.5.2 Contributions	22
1.6 Thesis Outline	24
CHAPTER TWO: BACKGROUND	26
2.1 GNSS System Architecture	26
2.2 GNSS Signal Structure	27
2.3 Traditional GNSS Receiver Architecture	29
2.3.1 RF Section	31
2.3.2 Signal Processing	31
2.3.2.1 <i>Local signal generation and correlation</i>	31
2.3.2.2 <i>Signal Acquisition and Tracking</i>	34
2.3.3 Measurement Generation	37
2.3.4 Navigation Solution	39
2.4 Special GNSS Receivers	41
2.4.1 High Sensitivity GNSS Receivers	41
2.4.2 Snapshot-based Positioning Method	43
2.4.2.1 <i>Coarse Time Problem</i>	44
2.4.2.2 <i>Coarse Time Navigation</i>	45
2.5 Effect of Urban Environments on GNSS Receivers	46
2.5.1 GNSS Signal Characteristics in Urban Areas	46
2.5.2 Effect of a Two-Path Signal on the Signal Processing of a Traditional GNSS Receiver	48
2.6 3D Building Models and Ray-Tracing for Multipath Environments	52
2.6.1 3D Building Models	53
2.6.2 Ray-tracing Technique	53
2.7 Summary	59

CHAPTER THREE: METHODOLOGY	60
3.1 3DBM-Assisted Multipath Parameter Estimation	60
3.1.1 Methodology for 3DBM-Assisted Multipath Parameter Estimation.....	60
3.1.1.1 <i>Predicted Signal Parameters</i>	62
3.1.1.2 <i>Least Squares-based Estimation of Multipath Signal Parameters</i>	62
3.1.2 Validation of 3DBM-assisted Multipath Parameter Estimation Technique....	65
3.1.2.1 <i>Simulated Scenarios</i>	66
3.1.2.2 <i>Results and Analysis for Data Collected in Downtown Calgary</i>	69
3.2 3DBM-assisted Snapshot Positioning Algorithm	71
3.2.1 Overview of the Positioning Algorithm	72
3.2.2 Generation of Observed Signal Parameters.....	74
3.2.3 Generation of Predicted Signal Parameters	76
3.2.4 SDM Algorithm.....	77
3.2.4.1 <i>Compute the SDM Metric Using LSQ</i>	78
3.2.4.2 <i>Effect of Under- and Over-Parameterization Using Least-Squares</i>	78
3.3 Summary	81
CHAPTER FOUR: RESULTS AND ANALYSIS.....	82
4.1 Data Collection	82
4.1.1 Data Set 1	82
4.1.2 Data Set 2	85
4.2 Data Processing.....	87
4.2.1 IF Data Processing.....	87
4.2.2 Predicting Signal Parameters.....	88
4.2.3 Positioning Algorithm (SDM Algorithm)	90
4.2.4 Performance of the Algorithm in Terms of Processing Time	91
4.3 Experimental Results and Analysis	92
4.3.1 In-Depth Analysis of Two Points	93
4.3.1.1 <i>Point 1 (20% Sky-Visibility)</i>	94
4.3.1.2 <i>Point 2 (60% Sky-Visibility)</i>	97
4.3.2 Analysis of Data Set 1	99
4.3.3 Analysis of Data Set 2 and Performance Comparison with Data Set 1.....	105
4.3.4 Statistics for Both Data Sets Combined	111
4.4 Uncertainty of Estimated Position	113
4.5 Summary.....	118
CHAPTER FIVE: SENSITIVITY ANALYSIS OF 3DBM-ASSISTED SNAPSHOT POSITIONING METHOD	120
5.1 Key Processing Parameters.....	120
5.2 Sensitivity to Size of PG.....	121
5.3 Sensitivity to Resolution of PG	126
5.4 Sensitivity to Error in Transmit Time.....	128
5.5 Sensitivity to Coherent Integration Time.....	133
5.6 Summary.....	135

CHAPTER SIX: CONCLUSION AND FUTURE WORK.....	137
6.1 Summary and Novelty of Research	137
6.2 Conclusions Based on Results Analysis	138
6.3 Recommendations for Future Work	140
6.4 Final Panoramic View and Impact of the Proposed Research.....	143
REFERENCES	144
APPENDIX: A.....	153
APPENDIX: B	158

List of Tables

Table 3.1: Correlator model and corresponding states for different signal path	63
Table 3.2: Different scenarios for two-path case	67
Table 3.3: Error statistics of delta path delay error for a downtown Calgary data	70
Table 4.1: Summary of processing parameters for generating observed signal parameters.....	88
Table 4.2: Time required for overall processing for position estimate at one epoch using a laptop with i7 2.4 GHz processor and 6 GB memory	92
Table 4.3: Summary of error statistics for Data Set 1 using different receivers.....	102
Table 4.4: RMS positioning improvement using the proposed algorithm for Data Set 1	102
Table 4.5: Summary of error statistics for Data Set 1 for epochs where vehicle speed was at least 10 m/s and for all epochs	105
Table 4.6: Summary of error statistics for Data Set 2 using different methods.....	106
Table 4.7: RMS positioning improvement using the proposed algorithm for Data Set 2	106
Table 5.1: Comparison of RMS of horizontal error for entire trajectory using different grid sizes.....	126
Table 5.2: Performance comparison for different grid resolutions for a 30x30 m grid.....	127
Table 5.3: Error in path delay, azimuth and elevation of point of intersection of incident ray and reflector as a function of transmit time error.....	132
Table 5.4: Effect of coherent integration time on proposed positioning algorithm.....	134

List of Figures and Illustrations

Figure 1.1: Sky-visibility in downtown Calgary. Left image shows the exact location and right image shows the sky-visibility at that location. As depicted poor sky-visibility poses significant challenges for GNSS-based navigation in urban canyons.	5
Figure 1.2: Signal blockage and signal reflections in urban canyons. A typical urban environment (such as downtown Calgary) would have many buildings. These buildings act as reflectors, contributing to severe multipath effects and signal blockage.	5
Figure 2.1: Generic GNSS receiver block diagram for a single channel. The colored arrows indicates outputs generated at the corresponding stage	30
Figure 2.2: Simplified block diagrams of signal acquisition stage. $f^{D'}$ and τ' represents Doppler frequency and code phase respectively of locally generated signal. S_I and S_Q are the in-phase and quadrature-phase correlation component respectively.....	32
Figure 2.3: Simplified block diagrams of signal tracking inside a traditional GNSS receiver. Usually there are 3 such loops each for early, prompt and Late correlators, however, for simplicity only one loop (for Prompt i.e. P) is shown.	36
Figure 2.4: Simplified block diagrams of open loop architecture-based GNSS receivers	42
Figure 2.5: Signal reception in a typical urban environment. Green line indicates LOS signal, red lines indicate NLOS signals from a satellite, and dashed red line represents blocked signal from another satellite. Because of LOS signal and NLOS signal(s), three in this case, from same satellite, a receiver receives the composite signal in urban environment. These composite signals results in multipath effect at receiver.....	47
Figure 2.6: Correlator outputs corresponding to LOS and NLOS signals. Figure (a) represents a case for NLOS signal, in-phase with LOS signal. Figure (b) represents a case when NLOs signal is in opposite phase of LOS signal.	51
Figure 2.7: Example of ray-tracer output for a single satellite. The blue star indicates receiver position, green face indicates the valid reflector and red face indicates a reflector from which the reflected rays cannot reach the receiver. Yellow rays indicate all the rays from satellite.	57
Figure 2.8: Scenario where a receiver receives a multipath signal. The receiver is at a normal distance of 'D' from the reflector. θ is the angle of incidence, which is a function of azimuth and elevation for a 3D case	58
Figure 3.1: Block diagram depicting Least-Squares fit of the observed correlators with the help of predicted signal information	61
Figure 3.2: RMS error of delta path delay for two-path signal. Comparison is done in presence and absence of assistance from 3DBM.	68

Figure 3.3: RMS error of delta path delay for three-path signal. Comparison is done in presence and absence of assistance from 3DBM related to delta path delay and its variance.	68
Figure 3.4: Generation of estimated and reference delta path delay (true delay) using real data.	69
Figure 3.5: Different set of reflections at two nearby locations ‘A’ and ‘B’. Receiver at location A receives 3 reflections from 3 different reflectors; whereas the receiver receives 2 reflections from 2 totally different reflectors at location B, from the same satellite.	72
Figure 3.6: An architectural depiction of the proposed algorithm. Predicted signal parameters are generated for different candidate points and are <i>matched</i> with observed signal parameters, using a matching algorithm.	74
Figure 3.7: Generation of observed path delay. Dotted box shows a method for obtaining code phase correlators information, used in this research. Observed path delays are obtained from code phase domain correlators.	75
Figure 3.8: Example of correlator grid in the code phase and Doppler domains. Correlators in blue are those in code phase domain corresponding to the Doppler with the maximum power.	76
Figure 3.9: Block diagram depicting generation of predicted path delay.	77
Figure 3.10: Cumulative distribution function (CDF) of estimated MDR values for over-parameterized, correctly-parameterized and under-parameterized cases.	80
Figure 4.1: Sky plot for Data Set 1; circles represent the satellite positions at the middle of data collection	83
Figure 4.2: Trajectory for Data Set 1 collected in downtown Calgary. Figure shows the trajectory along with the building heights throughout the trajectory. Buildings surrounding the trajectory were as high as 200 metres.	84
Figure 4.3: Sky-visibility throughout the trajectory for Data Set 1 collected in downtown Calgary. As depicted the sky-visibility is as low as less than 20 %, indicating deep urban scenarios.	85
Figure 4.4: Sky plot for Data Set 2 during middle of data collection.	86
Figure 4.5: Downtown Calgary data collection trajectory for Data Set 2. Top figure shows the trajectory along with the building heights and the bottom figure shows the percentage sky-visibility at each location throughout the trajectory.	86
Figure 4.6: Processed 3DBM purchased from 3DCAD browser.	89

Figure 4.7: Block diagram of 3DBM processing.....	90
Figure 4.8: Two different points considered for detailed analysis; upper figure (a) shows the surrounding environment with the approximate user location represented as a white triangle for Point 1 and the lower figure is for Point 2. The skyplots shown as sky (blue) and buildings (grey) are computed from the 3DBM.....	94
Figure 4.9: RSS of residuals for different PRNs at Point 1	95
Figure 4.10: Overall RSS of residuals from all PRNs and final estimated position (white star) at the Point 1	97
Figure 4.11: RSS of residuals from PRN 1, 14 and 32 at Point 2.....	98
Figure 4.12: Overall RSS of residuals from all PRNs and final estimated position (white star) at the Point 2	99
Figure 4.13: Horizontal error with respect to sky-visibility for the proposed algorithm and two pseudorange-based high-sensitivity receivers.....	100
Figure 4.14: Box plot of horizontal positioning error as a function of sky-visibility for Data Set 1 along with the number of samples in each bin.....	104
Figure 4.15: Comparison of RMS of horizontal error for the two data sets. Data Set 1 was collected with 20 MHz front-end bandwidth; Data Set 2 was collected with 4 MHz front-end bandwidth.....	107
Figure 4.16: Number of PRNs used for position computation for the two data sets	108
Figure 4.17: Total number of paths observed at estimated position, for the two data sets	109
Figure 4.18: Effect of number of PRNs used on horizontal positioning accuracy	110
Figure 4.19: Effect of number of paths on horizontal positioning accuracy	110
Figure 4.20: Box plot of horizontal positioning error as a function of sky-visibility for combined data sets (Data Set 1 and Data Set 2) along with the total number of combined samples in each bin.	112
Figure 4.21: Relation between easting error and maximum uncertainty in east direction based on the metric for three different factors, 20 %, 30 % and 50 %	115
Figure 4.22: Relation between northing error and maximum uncertainty in north direction based on the metric for three different factors, 20 %, 30 % and 50 %	116
Figure 4.23: Relation between horizontal error and maximum uncertainty in horizontal direction based on the metric for three different factors, 20 %, 30 % and 50 %	116

Figure 4.24: Linear fit between horizontal error and estimated horizontal error based on maximum uncertainty obtained from the pre-defined metric	118
Figure 5.1: RSS of residuals for PRN 1 (Az: 297°, Elve: 42°); size of position grid is 30x30 metres	122
Figure 5.2: RSS of residuals for PRN 1(Az: 297°, Elev: 42°); size of position grid 200x200 metres; shaded regions are buildings and are excluded from position grid for RSS of residuals calculation.....	123
Figure 5.3: RSS of residuals due to all PRNs present at this epoch; size of position grid is 30x30 metres. The white star represents the final estimated position	125
Figure 5.4: RSS of residuals due to all PRNs present at this epoch; size of position grid is 200x200 metres; shaded regions are buildings and are excluded from position grid for RSS of residuals calculation. The white star represents the final estimated position.....	125
Figure 5.5: Scenario with a reflector near-by receiver and reflections reaching the receiver	130
Figure 5.6: Difference in RSS of residuals for PRN 1 (Az: 297°, Ele: 42°), relative to Figure 3, due to a transmit time error of 10 s	132
Figure 5.7: Normalized correlator outputs for 10 ms and 100 ms coherent integration times. The correlator output corresponding to 10 ms is noisier compared to that of 100 ms.....	135

List of Abbreviations

3DBM	3D Building Model
APME	A-Posteriori Multipath Estimation
C/A	Coarse Acquisition
CDMA	Code Division Multiple Access
CIT	Coherent Integration Time
CP	Candidate point
DGPS	Differential GPS
DLL	Delay Lock Loop
DOP	Dilution Of Precision
DR	Dead Reckoning
EGNOS	European Geostationary Navigation Overlay Service
EKF	Extended Kalman Filter
EML	Early-Minus-Late
GAGAN	GPS Aided Geo Augmented Navigation
GLONASS	Global'naya Navigatsionnaya Sputnikovaya Sistema
GNSS	Global Navigation Satellite System
GPS	Global Positioning System
IF	Intermediate Frequency
INS	Inertial Navigation System
IRNSS	Indian Regional Navigation Satellite System
LHCP	Left Hand Circularly Polarized
LiDAR	Light Detection and Ranging

LOS	line-of-sight
LSQ	Least-squares estimation
MEDLL	Multipath Estimating DLL
MEMS	Micro Electro Mechanical Systems
MET	Multipath Elimination Technology
MDR	Multipath-to-Direct ratio
ML	Maximum-Likelihood
MMT	Multipath Mitigation Technique
MSAS	Multi-functional Satellite Augmentation System
NLOS	Non-line-of-sight
PG	Position grid
QZSS	Quasi-Zenith Satellite System
RF	Radio Frequency
RHCP	Right Hand Circularly Polarized
RMS	Root mean square
RSS	Root-sum-squared
SDM	Signal Delay Matching
SBAS	Satellite-Based Augmentation System
WAAS	Wide Area Augmentation System

List of Symbols

C	A scalar
\mathbf{C}	A vector
$(\cdot)(t)$	Quantity (\cdot) as a function of time
\hat{x}	Estimate of quantity x
A	Amplitude of received GNSS signal
A_R	Amplitude of correlated output
c	Speed of light
C/N_0	Carrier to noise power density ratio
f	Carrier-Phase
f^D	Doppler frequency due to relative velocity between satellite and receiver
H	Jacobian matrix (Observation Matrix)
η	Noise comprised of atmospheric noise and receiver thermal noise
ρ	Pseudorange
P_0	Covariance matrix of <i>a priori</i> information
$R(\cdot)$	Auto-correlation function of the ranging code
S_I, S_Q	In-phase and quadrature-phase correlator outputs
τ	Code phase
$\Delta\tau$	Difference between received and locally generated code phase
T_c	Coherent Integration Time
θ	Angle of incidence
t_{rx}	Receiver time

t_{tx}^i	Transmit time of i^{th} satellite
W	Measurement noise covariance matrix
δX	Error in states
Y^r	Received GNSS signal
δZ	Misclosure Vector

Chapter One: **Introduction**

This thesis work presents a novel and innovative positioning technique utilizing all reflected GNSS signals constructively with the help of a 3D Building Model (3DBM). The positioning algorithm is able to provide a reliable navigation solution even in deep urban canyons by using few milliseconds of Global Navigation Satellite System (GNSS) data, without using any filtering and without using any corrections from inertial sensors, networks or Wi-Fi.

This chapter provides an overview of satellite-based navigation systems and recent trends in their wide range of applications. Subsequently, this chapter presents the objectives, novelties and contributions of this dissertation and concludes with the outline of this thesis.

1.1 Navigation and Global Navigation Satellite System

Navigation is the science of guiding a vehicle or person from one place to another (Kaplan, 2006), and satellite-based navigation plays a key role in modern navigation services. Satellite-based positioning is experiencing a quick and fascinating evolution. This fact can be evidenced by the modernization of the Global Positioning System (GPS), and the increasing number of constellations in recent years, hence changing of era from GPS to GNSS. GNSS has proven a viable low cost solution for navigation and positioning in open sky.

A GNSS is a satellite-based navigation system with global coverage that works in all-weather conditions. The USA's NAVSTAR GPS and Russia's Global'naya Navigatsionnaya Sputnikovaya Sistema (GLONASS) are examples of fully operational GNSS. To date, several systems are only partially deployed or only regionally operating, including the European Galileo, the Indian Regional Navigation Satellite System (IRNSS), the Japanese Quasi-Zenith Satellite

System (QZSS) and the Chinese Beidou system. Beidou and Galileo are scheduled to be fully deployed and operational in the next few years.

GNSS has proven to be a viable positioning solution in open sky and the technology is further evolving rapidly as new systems and signals are developing. The day-by-day increase in popularity of GNSS can be evidenced by the increasing number of applications from mobile phones to aircraft landing. In a way GNSS has emerged as a mainstream technology for navigation for several outdoor applications, maintaining high reliability and accuracy demands even while using low cost portable devices.

Significant amount of power is lost due to channel propagation (free-space loss) as GNSS signals have to travel more than 20,000 km. Additionally, these signals are distorted by the atmosphere and by objects that block, attenuate or reflect the signals. Differential GPS (DGPS) significantly helps to reduce errors by cancelling satellite-based and atmospheric errors, however, this does not take care of problems due to signal reflection from nearby surfaces and signal attenuation. With the use of a dual frequency receiver, a major part of the atmospheric propagation delay error, the ionospheric delay, can be estimated. This approach has the advantage of being autonomous; however, the higher cost of receivers and antennas has limited its application so far to markets requiring a high level of accuracy. Differential carrier phase measurements can help a receiver to achieve a position solution with an accuracy of a few centimetres, provided good satellite visibility conditions are met and advanced processing is performed (Misra & Enge 2011). However, in a severe multipath environment such as in an urban canyon, continuous phase locked measurements to a sufficient number of satellite signals are unlikely, limiting the applicability of this technique to unobstructed environments.

As satellite-based navigation technology has matured over years, its application in high accuracy systems has also increased. One way of achieving these accuracy levels are Satellite-Based Augmentation System (SBAS), which are used in order to send local correction data. This service is currently provided by the Wide Area Augmentation System (WAAS) over North America, the European Geostationary Navigation Overlay Service (EGNOS) in Europe, the Multi-functional Satellite Augmentation System (MSAS) over Japan, the Indian GPS Aided Geo Augmented Navigation (GAGAN) system or by commercial satellite systems like John Deere's StarFire or Fugro's OmniSTAR systems. These systems works well, however, still multipath and signal reflection remain unsolved problems using these techniques.

As the technology has matured and expanding demand of GNSS-based positioning for mobile devices has increased, snapshot positioning techniques (Badia-Sole and Iacobescu-Ioan 2010, Fernandez-Hernandez and Borre 2016 and Qian et al. 2008 have turned out to be a viable solution due to its faster position fix ability and low power consumption (Yao et al 2010). Qian et al (2008) has demonstrated that by using 100 ms snapshots of data, the signal processing and hence power consumption was reduced by 60% compared to continuous mode traditional receiver. However, few ms of the snapshot data are not sufficient to decode the navigation data and hence snapshot techniques are associated with the coarse time navigation problem (Van Diggelen 2009). Various code phase-based coarse time navigation methods have been presented in literature such as Lanneloune and Pablos (1998) and Muthuraman et al (2011). The basis of these algorithms is to estimate an additional 5th state called the "coarse time error" (Petovello and Curran 2013, Van Diggelen 2009). Fernandez-Hernandez and Borre (2016) and Petovello &

Curran (2013) have presented a coarse-time Doppler navigation algorithm based on the addition of a fifth state to the instantaneous Doppler equations (Van Diggelen 2009).

As discussed above, snapshot algorithms are capable of reducing power consumption by not doing signal processing continuously; however, these algorithms suffer from the coarse time navigation problem (Petovello & Curran 2013, Van Diggelen 2009). Furthermore, code phase-based coarse time navigation poses challenges in urban environments because the code phase measurements are sensitive to multipath effects. Additionally, in deep urban canyons due to limited satellite visibility the snapshot positioning algorithms are unable to acquire five satellites for a coarse time navigation, hence, limiting performance (Carrasco-Martos et al 2010, Van Diggelen 2009).

As a summary, GNSS-based navigation has proven to be a viable low cost solution to the mass market; however, the system undergoes severe challenges in urban canyons due to multipath problems, which still remains significant source of error, as described in the following section.

1.2 GNSS in Urban Canyons: Challenges of Multipath

According to world urbanization trends, 54 % of the world's population resides in urban areas and this is expected to increase to 66 % by 2050 (United Nations 2014). This alludes towards the increased demand of technologies like GNSS-based positioning in urban areas. However, as indicated in the previous sub-section, GNSS-based positioning becomes challenging in urban environments. To illustrate the challenges of using GNSS-based systems in urban environments, a typical urban canyon environment with related challenges is depicted in Figure 1.1 and Figure 1.2.

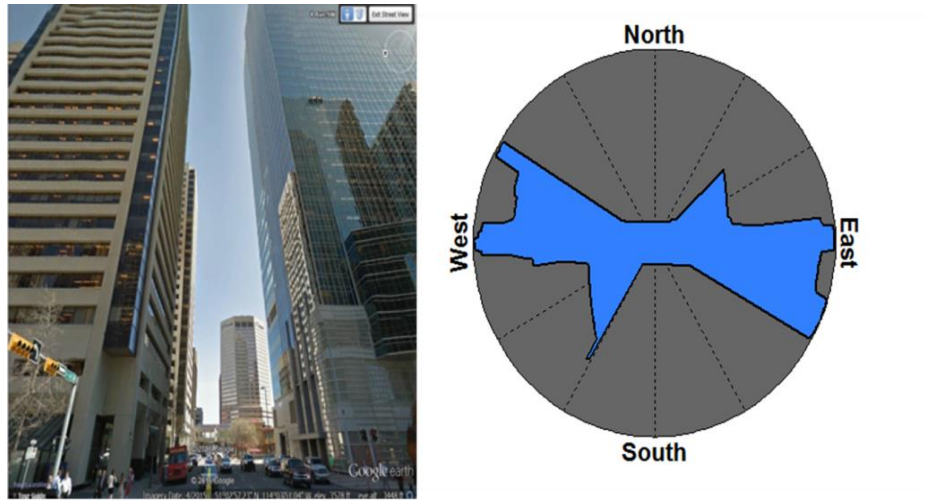


Figure 1.1: Sky-visibility in downtown Calgary. Left image shows the exact location and right image shows the sky-visibility at that location. As depicted poor sky-visibility poses significant challenges for GNSS-based navigation in urban canyons.

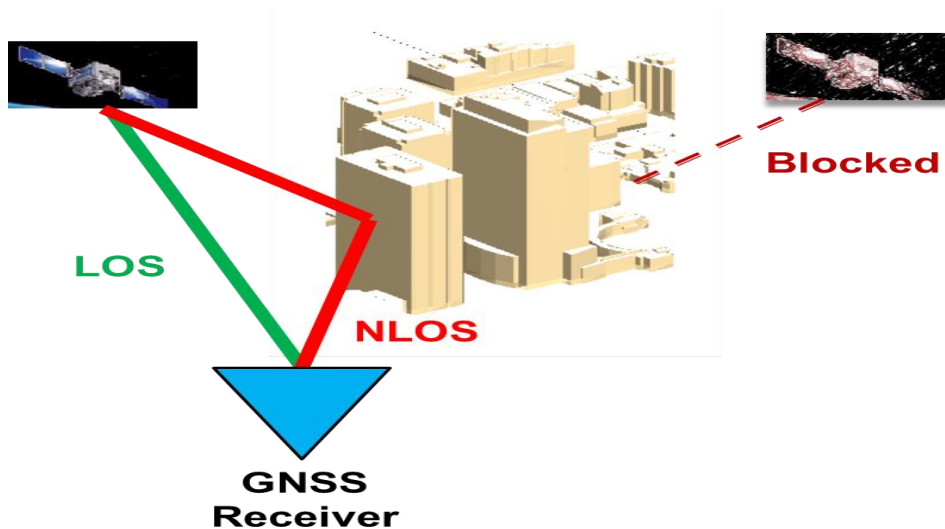


Figure 1.2: Signal blockage and signal reflections in urban canyons. A typical urban environment (such as downtown Calgary) would have many buildings. These buildings act as reflectors, contributing to severe multipath effects and signal blockage.

As depicted in Figure 1.1 and Figure 1.2, GNSS-based navigation suffers from primarily two kinds of problems: poor sky-visibility and reflected signals or non-line-of-sight (NLOS) signals.

These NLOS signals are delayed with respect to line-of-sight or LOS signals and result in multipath effects when combined with LOS signal. More precisely, multipath is a phenomenon whereby a receiver receives signals from multiple paths including reflections and refraction.

Commonly, multipath mitigation techniques are categorized as: antenna/hardware-based mitigation (Townsend and Fenton, 1994; Moelker, 1997; Filippov et al., 1998), improved signal processing (Fenton et al., 1991; Townsend and Fenton, 1994; Weil 1995; McGraw and Braasch, 1999), and technology based on integration of GNSS with dead reckoning system (such as Gu et al 2015 and Angrisano et al 2012). In recent years, research has been done towards integrating GNSS system with 3D city models (Bourdeau 2012, Bourdeau 2012a, Ben-Moshe 2011, Groves 2011, and Bradbury et al 2007).

1.2.1 Antenna/hardware-based Technologies

Antenna/hardware-based technologies attempt to eliminate the multipath signals at the pre-reception stage (i.e., before signal processing stage). Antennas-based multipath mitigation technologies involve spatial processing to improve the antenna gain pattern to counter the multipath effect (Ray 2000). The most common methods are to use choke rings and dual polarization antennas to prevent secondary reflections from entering the receiver's front-end (such Manandhar & Shibasaki 2004). The main purpose of the choke ring design is to eliminate the signals reflected from the Earth surface (Filippov et al., 1998). Since the GNSS signal has a right-hand circular polarization (RHCP), by designing a specific gain pattern to attenuate left-hand circular polarization (LHCP) signals, significant improvements has been achieved (Bartone and Van Graas, 1998). However, these suffer from problems of high cost involved in design and large size and weight. Moreover, since most of NLOS signals arrive from above the horizontal

plane in urban canyons these methods do not help in eliminating NLOS signals and multipath effects. A novel multipath mitigation technique was proposed by Groves et al (2010). In this technique, a dual-polarization antenna was used for multipath detection using carrier to noise power density ratio, C/N_0 , from separately correlating the Right Hand Circularly Polarized (RHCP) and Left Hand Circularly Polarized (LHCP) outputs. However, the sensitivity was observed to be much better for higher elevation satellites than for lower elevation satellites. Utilizing this type of antenna, an approach for multipath and NLOS mitigation is proposed by Groves et al (2013). Therein a multipath mitigation technique using multi-frequency C/N_0 measurements is proposed along with a portfolio approach which uses multiple techniques including antenna design, code discriminator design, consistency checking, and dual-polarization technique to eliminate multipath effect.

1.2.2 Signal Processing Technologies

Since multipath effects distorts the shape of correlation function inside the receiver, multipath mitigation approaches at the signal processing level can be achieved utilizing correlator information (Irsigler and Eissfeller, 2003). The most conventional correlation-based code structure is based on Early-Minus-Late (EML) technique. The choice of correlator spacing usually depends on the receiver's available front-end bandwidth along with the associated sampling frequency (McGraw and Braasch 1999, Irsigler and Eissfeller 2003, Van Dierendonck et al 1992). Multipath mitigation approaches at the signal processing level take advantage of the correlation shape in the code phase domain. Some well-known examples of this category are the narrow correlator method (Van Dierendonck et al 1992, Fenton et al., 1991), multipath elimination technology (MET), strobe and edge correlator (Garin & Rousseau 1997), and

enhanced strobe correlator (McGraw and Braasch, 1999). Another category uses estimation techniques, which treat the multipath as something to be estimated from the correlators (Lentmaier et al., 2008), and using different efficient maximization strategies over the likelihood function, e.g., multipath mitigating technique (MMT) (Weil, 1995), multipath estimating delay lock loop (MEDLL) (Van Nee et al 1994; Van Nee 1992), and vision correlators (Fenton and Jones, 2005) were proposed and are less susceptible to the multipath. These techniques, however, are not very effective for small multipath, due to close-by reflectors. The techniques mentioned above employ some specific discriminators to take full advantage of the correlation shape in the code phase domain, but the multipath peak still exists in the correlation function.

Stone & Chansarkar (2004) have provided an approach to deal with multipath in urban environments using a statistical model in which the user location can be estimated by maximizing likelihood or minimizing expected squared error. However, the likelihood function presented there assumes that the true code phase is known. Sleewaegen & Boon (2001) have proposed A-Posteriori Multipath Estimation (APME) technique, which relies on a-posteriori estimation of the multipath error affecting the code tracking. The multipath estimation methods estimate multipath signal parameters and then compensate it with the incoming signal to obtain direct signal. More specifically, the tracking is done in a conventional narrow correlator Delay Lock Loop (DLL), offering a low tracking noise and the multipath error affecting the narrow correlator tracking is estimated in an independent module on the basis of different signal amplitude measurements. Comparison of several multipath mitigation techniques with a deconvolution algorithm is done by Pratt (2004), Kumar & Ahmad (2004), and Dragunas &

Borre (2011). It is shown that the performance of their optimum deconvolution-based algorithm exceeds conventional techniques in terms of residual multipath error.

Several efficient in-receiver multipath mitigation methods have also been proposed by Sahmoudi & Amin (2008), Ward et al (2006), Irsigler and Eissfeller (2003), Braasch (2001), and Van Dierendonck et al (1992). These methods include the narrow correlator, the strobe correlator, the multipath estimating delay lock loop, the multipath elimination technology, the vision correlator and the fast iterative maximum-Likelihood algorithm. Sokhandan (2013) has proposed a receiver design which adaptively alternates between full channel characterization and recursive channel refinement, depending on the severity of the variations of the channel to provide a robust and efficient multipath mitigation. Furthermore, Sokhandan (2013a) has proposed different approaches based on Maximum-Likelihood (ML) estimator, modified adaptive filters and subspace-based methods for multipath mitigation using channel parameter estimation. The results shown there indicate that the proposed algorithm outperforms the classical delay lock loops and conventional ML-based algorithms.

An incredible amount of research has been directed towards improving positioning accuracy in harsh environments using enhanced receiver sensitivity. Watson (2005) demonstrated benefits of longer coherent integration to achieve better sensitivity in weak signal environments. A block processing approach was demonstrated by Ujit de Haag(1999), to improve the positioning performance by fine searching in code and Doppler domain. Xie and Petovello (2015), have demonstrated that the multipath signals can be separated in the Doppler domain by increasing coherent integration time. However, for these works to achieve the required signal processing gain, the signal should either have a data-less pilot channel, or otherwise requires the knowledge

of data bits from external aiding or from bit estimation schemes to wipe off the data bits during the longer integration process. Further, it also requires a good clock source which can provide undrafted pulse during the integration process.

Lin et al (2011) have utilized a combined approach of block processing and centralized vector-based tracking for robust indoor navigation. The processing load of the receiver and measurement weighting were optimized using a context-aware approach in order to provide seamless outdoor-indoor navigation. Chan & Petovello (2011) have shown the improvement in the performance of Vector-based GNSS receivers by using Ultra-Wideband (UWB) ranging and Differential GPS (DGPS) corrections. Therein it was shown that by taking advantage of DGPS observations between two nearby receivers as well as UWB range observations, the collaborative vector-based receiver was able to achieve a more accurate navigation solution.

In order to improve the accuracy of GNSS systems in multipath prone areas various options have been explored, for example, integrating GNSS with Dead Reckoning (DR) systems, explained in section 1.2.3 and integrating with 3D building models, explained in section 1.2.4.

1.2.3 Integration of GNSS and Dead Reckoning System

inertial navigation systems, which provide very accurate directional information, use dead reckoning and are very widely used as aiding source to GNSS in multipath prone areas (Lin et al 2016, Soloviev et al 2011, Petovello et al 2008, Petovello & Lachapelle 2006, and Li et al 2011).

Unlike GNSS systems, an Inertial Navigation System (INS) is used for autonomously determining position using inertial angular rate sensors, acceleration sensors, a data processing computer and an initial position, velocity and orientation. The change in orientation is obtained

from the gyroscopes while the position and velocity is obtained by double and single integration of the acceleration (Noureldin et al 2013, Jekeli 2001). Hence INS is essentially immune to the external interference and multipath. Moreover, the accuracy of an INS is limited by the sensor quality, which introduces position and velocity errors in terms of drifts that increase with time. GNSS provides better long term accuracy and INS provides better short term accuracy. Several approaches have been researched based on GNSS/INS integrated navigation systems to take advantage of such complementary characteristics (such as Scherzinger 2015, Soloviev et al 2011, Petovello 2003). The combined system offers a significant gain in performance in terms of accuracy and robustness compared to the standalone usage of either system (Wendel et al 2004). In this regard, there are mainly three strategies employed to integrate GNSS and INS together, which are normally classified as loosely-coupled, tightly-coupled, and ultra-tightly-coupled systems (Petovello 2003).

Loosely-coupled strategy is straightforward and relatively simple to implement because the position and velocity from the GNSS receiver are utilized as the measurement in the navigation filter, generally a Kalman filter, and augmented directly with the states of INS (Noureldin 2013, Petovello 2003). In the tightly-coupled system, the raw measurements such as pseudorange and carrier Doppler are utilized directly in the GPS/INS Kalman filter as the measurements (Petovello 2003). In ultra-tight configuration, INS is used to aid the GNSS receiver tracking loops while the GPS updates are used to calibrate the INS (Petovello 2003). Moreover, Groves et al (2007) have used a non-coherent approach of GPS/INS integration where the in-phase and quadrature-phase correlator values are passed through code and carrier discriminator functions, similar to those used in conventional GNSS receiver. Further to this, benefits of a vector-based

ultra-tight scheme are discussed in Petovello & Lachapelle (2006). The simulated results shown there indicate that a velocity solution accurate to few centimeters per second was maintained and the proposed configuration was able to track the carrier phase up to an attenuation of about 15 dB. Godha et al (2005), and Mezentsev et al (2002) have explored the use of low cost sensors in urban canyons.

Soloviev et al (2007) have demonstrated a deep integration of GPS/INS for urban canyon navigation applications. Therein it has been shown that up to 6 satellites were tracked and velocity accuracy in range of cm/s was achieved for a real data collected in downtown Athens, Ohio. Soloviev & Van Graas (2009) have shown that the multipath signal can be detected and the NLOS signal can be segregated from LOS signals using a Laser scanner and deeply integrated GPS/INS system. O'Driscoll et al (2010) have shown the benefits of GPS/GLONASS in urban environments and an improvement of 10% in terms of availability of signals was reported. Lehner & Steingass (2008) have characterized signal reflections in urban and suburban areas using reflector scenarios simulation.

Recent advances in Micro Electro Mechanical Systems (MEMS) technology have enabled development of a new generation of low cost inertial sensors. These systems are characterized by their small size and light weight, which represents an attractive option for mass-market applications such as vehicular and pedestrian navigation. In this regard, positioning performance enhancement of MEMS INS/GPS integrated system was analyzed by Yang (2008) and Noureldin et al (2009). Yang (2008) used Extended Kalman Filter (EKF) to control MEMS sensors errors and by so doing the position accuracy was improved by 60%. Noureldin et al (2009) have used autoregressive processing for modeling the stochastic modeling of MEMS-based inertial sensor

error for improving the overall performance of GPS/MEMS INS systems. Likewise, Gao et al (2008) have integrated information from steering angle sensors to GPS and MEMS-based INS systems. Improvement in horizontal position accuracy was 50% for open sky scenarios (GPS outage case) and about 30% in real-time tests in suburban environments.

Furthermore, multi-sensor systems that integrate sensors from vehicles have been studied and implemented to reduce the errors due to MEMS sensors in GPS/MEMS INS integration (Iqbal et al 2009, Cossaboom et al 2012). An improvement of 45% in position accuracy was obtained as compared to KF only method. Benefits of combined GPS/GLONASS with low cost MEMS IMU for vehicular navigation were also investigated by Angrisano et al (2012). Results shown indicate that the benefit of adding GLONASS could be achieved only for tight integration algorithms in case of poor visibility. Moreover, for benign environments, it was observed that loosely coupled GPS/GLONASS/INS system offered comparable performance with tightly coupled GPS/INS system.

A unique quasi-tight integration of GNSS and INS was proposed by Scherzinger (2015) for single point positioning. The proposed quasi-tightly coupled integration is a method of loosely coupled integration that has the salient characteristic of continued aiding with fewer than four satellites that a tightly coupled integration typically exhibits. More precisely, a quasi-tight method is intended for the integration of an existing GNSS navigation engine into a GNSS-INS closed-loop configuration with little or no modification of the GNSS navigation engine (Scherzinger 2015). Some recent researches have also focused on improving the positioning performance and processing time (Abd Rabbou and El-Rabbany 2015) and improving availability of integrated solution (Aftatah et al 2016).

Although low-cost GNSS/DR systems perform well in some vehicular applications, they are still vulnerable to weak signals and multipath environments. More precisely, if a standard GNSS receiver or high sensitivity receiver is utilized in the GNSS/DR system, the limits for the GNSS receivers also limit the ultra-tight GNSS/DR system. In particular, the positioning errors will be accumulated in the GNSS/DR system when the update information is not available.

1.2.4 GNSS Aiding With 3D Building Models

Beyond using standalone GNSS systems or DR-integrated GNSS systems, research is ongoing towards using external information from 3D building models (3DBMs) for improving GNSS-based positioning in urban canyons (such as Bradbury et al 2007, Groves 2011, Hsu et al 2016). 3DBMs are digital representations of cities containing relevant geospatial information (Frere et al 1998). Using a 3DBM, the location of buildings/reflectors in the area surrounding a receiver can be identified and once the reflectors' positions are known the extra delay of the NLOS signal (with respect to LOS signal) for a particular reflector at particular receiver position can be computed and provided as additional information to the receiver or navigation filter. This delay information can be used either for identifying the NLOS signal and removing it from receiver measurements; or the delay information can be utilized to use NLOS signals constructively. It is highly likely that, in urban canyons, rejecting any measurements would lead to reduced availability and poor dilution of precision (DOP), hence the later approach for using NLOS signals constructively would be beneficial in terms of improved availability and hence better accuracy. The following paragraphs describe how 3DBMs have been utilized for improving position accuracy in urban canyons.

Bradbury et al. (2007) used a 3DBM for determining satellite availability and analyzing signal degradation in multipath environments based on simulated test cases. Lee et al (2008) have used a spatial statistics-based simulation system for mitigating multipath and improving the accuracy in GNSS positioning. The metric of NLOS signal exclusion using an elevation enhanced map, extracted from a 3D map was developed and tested using real vehicular data by Pinana-Diaz et al (2011). Obst et al. (2012) used a 3DBM to detect and predict GNSS multipath situations in urban areas without any additional hardware. A forecast satellite visibility based on a 3D urban model to exclude NLOS signals in urban areas was developed in Peyraud et al. (2013). The above approaches aim to exclude the NLOS signal which, as mentioned above, is likely to cause large horizontal DOP values in urban canyons due to the blockage of buildings along both sides of streets.

A shadow matching technique to compare measured satellite visibility with predicted satellite visibility, using a 3DBM has been used for improved positioning accuracy in urban canyons (Groves 2011, Ben-Moshe et al. 2011). The algorithm was further incorporated with scoring matrix for improving the classification of LOS and NLOS signals and for real time applications (Wang et al 2015, 2013). However, these algorithms depend highly on the ability to correctly classify LOS and NLOS signals based on C/N_0 . Moreover, not all satellites are utilized for positioning; only those satellites which experience LOS and NLOS across the width of a street can be used for this method. A robust shadow matching method was proposed by Yozevitch and Ben Moshe (2015), however, this method requires a secondary antenna for LOS-NLOS classification. Still this does not utilize all NLOS signals from all satellites. An intelligent positioning technique utilizing shadow matching was proposed by Groves et al (2012), where an

approximate user position computed using available signals was refined using shadow matching to eliminate NLOS signals, thus providing final solution using LOS only signals.

Suzuki & Kubo (2012) and Suzuki and Kubo (2013) proposed an SNR matching based positioning and multipath and NLOS delay estimation method based on particle filter respectively. Later, Suzuki (2016) had used shadow matching and particle filter for refining positioning accuracy in urban environments with the help of a 3DBM. Moreover, 3DBMs have been used for, reliable positioning in LOS/NLOS mixed signals' environments, by estimating pseudorange biases (Ahmad et al 2013). Bourdeau et al. (2012) showed that a 3DBM can be used constructively for GNSS-based positioning in urban canyons using an extended Kalman filter. Adjrd and Groves (2015) have obtained real-time metre-level mobile positioning in outdoor urban environments by making use of spatial data in the form of 3D city models. Hsu et al (2016, 2016a) have used 3D building model for pedestrian positioning using GPS/GLONASS/QZSS in urban canyons and for autonomous driving position applying differential GNSS. A probabilistic approach for LOS and NLOS signal classification, for 3DBM-based position estimate is proposed by Bauer et al (2013). All these methods are based on traditional pseudorange-based approach and correcting the pseudorange using 3DBM.

3DBMs are also used along with other sensors for positioning in urban canyons. Ramalingam et al. (2009, 2010) used 3DBM and omni-images for skyline-based positioning. Petovello & He (2016) have demonstrated unique usage of 3DBM for skyline positioning method. Gu et al (2015) have used 3DBM along with onboard sensors for self-localization of a vehicle in urban canyons.

1.3 Motivation

GNSS-based positioning poses several challenges in urban environments. Most of the traditional methods are either costly due to involvement of hardware changes or sophisticated antenna, or use external sensors utilizing the benefit of the combined system. However, in deep urban environments GNSS/INS integration does not provide reliable solutions due to limited or no visibility of satellite and hence GNSS outage. Methodologies at the signal processing level have shown interesting and promising results, however, much work has been done towards identifying or mitigating multipath effects and little work has focused on using NLOS signals from all satellites constructively in order to derive or improve position determination. In this regard, aiding information from 3DBM has shown promising results but still the technology has not yet matured to exploit maximum information from multipath signals in efficient way. As a summary:

- Much research has been done towards mitigating the multipath effect but considerably less work has been done towards using NLOS signal constructively for improving accuracy in urban canyon based navigation
- All the research so far is focused on the *dominant* correlator peak and how to use it either directly, in case of LOS signals, or after correcting for excess path delay, in case of NLOS signals. More precisely, no research has attempted to utilize all correlator outputs towards constructive use of all NLOS signals.
- 3DBMs can be used to identify NLOS signals and remove them from the navigation solution, however, these methods result in poor HDOP in deep urban areas where satellite visibility is a concern and rejecting satellites often results in degraded performance or no navigation solution

- 3D city models can be used to extract the path delay associated with NLOS signals (extra path of NLOS signal with respect to LOS signal). This extra delay can be compensated in order to obtain corrected measurements for navigation solution. This is one way to utilize NLOS signal constructively (Bourdeau et al. 2012, Ahmad et al. 2013 and Hsu et al 2016), but their research only considered continuously tracking receivers based on traditional pseudorange method. These methods based on traditional pseudorange-based approaches suffer from pseudorange-based methods limitations.
- 3DBMs-based shadow matching algorithms have been widely used (Groves 2011, Wang et al 2015), however, the algorithm to date can only use those satellites which experience LOS and NLOS as you move across a street (at a given location). Moreover, the C/N_0 -based approach for declaring LOS signals is not always reliable in all urban scenarios (Ahmad et al 2013).
- Snapshot-based positioning approaches (Fernandez-Hernandez and Borre 2016 and Qian et al. 2008) are increasing in popularity relative to continuously tracking receivers; 3DBM-assisted snapshot positioning technique is still missing in order to exploit the advantages of both, i.e. aiding information and snapshots methods simultaneously.

These factors motivate the need to develop a positioning technique utilizing all embedded information from all NLOS signals that can provide improved positioning accuracy in deep urban canyons, by using a snapshot of GNSS data and without tracking the GNSS signal continuously.

1.4 Objectives

This thesis proposes a novel positioning algorithm that provides a reliable solution in deep urban canyons, addressing problems of standalone GNSS-based positioning in urban canyons. With this in mind, the primary objective of this research was to develop a snapshot-based GNSS positioning algorithm that can provide reliable positions in deep urban canyons, utilizing the path delay from all NLOS signals constructively with the help of a 3DBM. Secondly, the performance of the algorithm is tested and analyzed using real data collected in downtown Calgary, Canada and is compared with a receiver representing commercial (mass-market) GNSS receivers. Finally, a detailed sensitivity analysis of the proposed algorithm, with respect to various algorithm parameters, is presented using real data collected in downtown Calgary. In summary, the objectives and goals envisaged by this research can be summarized in following points:

- To design and develop a novel positioning algorithm based on *matching* “path delay(s)” of NLOS signal(s) *observed* in correlators with *predicted* path delays, as explained in Chapter 3. The use of path delay enables the constructive use of all NLOS signals and has several advantages compared to traditional pseudorange-based approach, as highlighted in section 1.5.1.
- To design and develop a low cost (without additional sensors or costly hardware), power efficient (snapshot-based; no continuous tracking), novel positioning technique (not based on traditional pseudorange-based) utilizing all NLOS signals constructively, using readily available 3D building models, in order to improve position accuracy

- Performance analysis and comparison (in terms of accuracy) of the proposed algorithm with a commercial receiver, using real data collected in downtown Calgary, for different kinds of urban environments. The purpose of doing this analysis was to obtain a relationship between accuracy of the proposed algorithm with respect to sky-visibility.
- Sensitivity analysis of the proposed algorithm with respect to various algorithm parameters using real data. The purpose of this is to find some of the crucial parameters which can affect the algorithm towards its performance to maximum extent in different kind of environment or in other words to find some parameters which would affect mildly.

1.5 Novelty and Contributions

This section provides the novelties and contributions of this research in two separate subsections as described below.

1.5.1 Novelties

The novelties of the algorithm proposed in this thesis can be summarized as below:

1. Development of a unique snapshot-based GNSS positioning algorithm integrated with 3DBM, utilizing all NLOS signals constructively. The proposed algorithm offers the following benefits:
 - By using a snapshot technique the receiver need not perform tracking operation. Although previous work has demonstrated constructive use of NLOS signals using corrected pseudoranges (such as Hsu et al 2016 and Miura et al 2013), the use of pseudoranges still requires the signal be tracked over time.

- Removing the tracking loops avoids challenging issues such as: loss of lock due to signal attenuation and/or user motion, tracking loop instabilities when tracking weak signals (Van Graas et al 2009), cross-correlation tracking, locking on to side peaks (e.g., for BOC signals) and filtering effects when NLOS-only signals are received/tracked.
 - The proposed method is different from the existing shadow matching techniques as it does not need C/N_0 -based LOS/NLOS signal classification, which is known to be ambiguous (Ahmad et al 2013). Furthermore, the proposed algorithm utilizes all NLOS signals as opposed to shadow matching which does not use all NLOS signals from all satellites, as mentioned in 1.2.4.
 - By only using snapshots of data, the proposed method tends to be more power efficient (compared to signal tracking), can be used on an as-needed basis and can provide a solution more quickly because a C/N_0 estimate is unnecessary
2. The proposed algorithm is based on matching path delays of NLOS signals with respect to the shortest path for any given satellite, using a unique *Signal Delay Matching* (SDM) technique, as explained in Chapter 3. The proposed positioning algorithm is thus virtually unaffected by traditional GNSS error sources (receiver clock, atmospheric errors, orbit errors, etc.), since these errors are nearly exactly the same across multiple received paths.
 3. The proposed algorithm has the capability of providing a position solution using a single satellite only, in theory; however, the performance using single satellite would depend on several factors and is presented in this thesis using real data from downtown Calgary.
 4. The proposed algorithm is based on using all correlator information corresponding to all NLOS signals and LOS signals, as input (as explained in Chapter 3). The method avoids

the loss of information resulting from reducing all correlator data into a single pseudorange (or code phase) measurement (He and Petovello 2014)

5. The proposed algorithm provides *best* performance in terms of horizontal position error, in deep urban canyons with sky-visibility as low as 20%; this contrasts with traditional standalone receiver performance which fails to provide position estimate in deep urban canyons. The detailed error analysis of the proposed algorithm, for different sky-visibility is presented in Chapter 4.
6. The proposed algorithm is nearly insensitive to various processing parameters, most notably coherent integration time and coarse time errors. The detailed sensitivity analysis is presented in Chapter 5.
7. One of the by-products as a result of the proposed novel technique is a *3DBM-assisted multipath parameter estimation technique*, which can estimate multipath parameters more accurately and faster as compared to traditional multipath parameter estimation techniques mentioned above in 1.2.2.

1.5.2 Contributions

This research consists of novel part (core research) as mentioned in 1.5.1 and some development part to support the proposed research. This sub-section highlights the contributions of this thesis:

1. This is first time a positioning algorithm is presented utilizing all NLOS signals constructively using a snapshot of GNSS data. It is expected that this will spur additional research in this area in the future.

2. As by-products of this thesis, the following software were developed in-house apart from the core software (GNSS-3DBM integration, mentioned in ‘*point 1*’ above):
 - A robust ray-tracer in MATLAB, which identifies all nearby reflectors in vicinity of the receiver and provides a set of *valid reflectors*, after verifying that the corresponding reflected signal to the receiver is not obstructed by other reflectors in the vicinity. Furthermore, the ray-tracer also provides number of valid reflectors and path delay(s) associated with each reflected signal.
 - A MATLAB-based 3DBM reader to read the wavefront file in object format and directly provide building coordinates in ECEF coordinates.
3. Since the 3DBM was purchased from a UK-based company (<http://www.3dcadbrowser.com>), a validation was done to check the accuracy of the 3DBM. The validation for the accuracy was done with a fairly precise 3DBM obtained from City of Calgary (Appendix B). The accuracy of the 3DBM was found to be 3 m, which can be used as a-priori information for this 3DBM in the future.
4. This thesis provides a performance comparison, in terms of horizontal position error, of the proposed algorithm with a representative mass market receiver. Furthermore, the results and analysis presented in this thesis, based on data collected from Downtown Calgary, can be used as a-priori information for continuing future research using 3DBMs.
5. Finally, four research papers were published out of this thesis, as mentioned below:
 - Kumar, R., and M. Petovello (2016), “3D Building Model-assisted Snapshot Positioning Method ”, conditionally accepted GPS Solutions 2017; peer reviewed journal

- Kumar, R., and M. Petovello (2016), “Sensitivity Analysis of 3D Building Model-assisted Snapshot Positioning Method”, ION GNSS+ 2016, 12-16 Sep. 2016, Portland, OR, USA; peer reviewed conference
- Kumar, R., and M. Petovello (2015), “3D Building Model-Assisted Multipath Signal Parameter Estimation”, IEEE IPIN 2015, 13-16 Oct. 2015, Banff, AB, Canada; peer reviewed conference
- Kumar, R., and M. Petovello (2014), “A Novel GNSS Positioning Technique For Improved Accuracy in Urban Canyon Scenarios Using 3D City Model”, ION GNSS+ 2014, 8-12 Sep. 2014, FL, USA

1.6 Thesis Outline

The remainder of the thesis is structured as follows:

1. *Chapter 2* provides the relevant background to understand the proposed algorithm. The chapter starts with a brief GNSS overview including GNSS signal structure in open sky and in urban canyons, followed by an introduction to traditional GNSS receivers, signal processing and navigation solution computation. Since the proposed algorithm is a snapshot-based positioning method integrated with 3DBMs, snapshot positioning methods and associated coarse time problem are also discussed, followed by introduction to 3DBMs, ray-tracing methods and their applications in urban environments.
2. *Chapter 3* describes the novel positioning algorithm. The chapter starts with a high level description of the algorithm with a block diagram. A detailed description of each component is presented in the following sections.

3. *Chapter 4* describes the results and performance analysis of the algorithm using live data collected in downtown Calgary. Furthermore, a comparison is done in terms of horizontal error performance of the proposed algorithm with a commercial receiver with a highly accurate reference solution. The highlight of this chapter is that the proposed algorithm's is shown to perform better in deep urban canyons with sky-visibility as low as 20 %, compared to a standalone traditional or mass market receiver, which performs poorly (if at all) in deep urban canyons.
4. *Chapter 5* contains the sensitivity analysis of the algorithm with various processing parameters such as coherent integration time and coarse time errors. It is found that the proposed algorithm is nearly insensitive to coherent integration time and coarse time errors. The chapter includes sensitivity analysis to other processing parameters as well.
5. The thesis concludes with *Chapter 6*, which includes a discussion, conclusions, and recommendations for future research and an outlook into the future potential integration of LOS-based method to the proposed algorithm

Chapter Two: **Background**

This chapter provides an overview of relevant background required to understand the proposed methodology presented in the following chapters. The chapter is divided into six major sections: GNSS system architecture, GNSS signal structure, traditional GNSS receivers, special GNSS receivers, effect of urban environments on GNSS receivers, and 3D building models and ray-tracing for urban environment applications.

2.1 GNSS System Architecture

GNSS are satellite-based radio navigation systems formed by three constituent segments: the space segment, control segment and user segment (Misra & Enge 2011). The space segment consists of a constellation of orbiting satellites in different orbital planes. The control segment is formed by ground-based control stations that primarily monitor the satellites' orbits, maintains GNSS time and update navigation messages. The user segment is formed by the civilian and military users who employ receivers capable of receiving the signals transmitted by the satellites and obtaining navigation and timing solutions. Traditionally, in order to obtain the navigation and timing information, a receiver must simultaneously track at least four satellites, and extract the required navigation data from the transmitted satellite signal. However, due to free space loss, the received satellite signal power is extremely weak and is below receiver noise level (Van Diggelen 2009). Hence, the receiver's task becomes challenging in order to extract the navigation data from the satellite signal. Before delving into details of the receiver architecture and position computation, the following section describes the structure of GNSS signals. Although the development in the following section corresponds to GPS L1 signal, the general

form of the equations would hold for other GNSS signals as well. By extension, the implementation of the proposed methodology (Chapter 3), is not limited to GPS L1 signal alone.

2.2 GNSS Signal Structure

All GNSS signals consist of a carrier frequency, a ranging code and, optionally, navigation data. The carrier frequency is used to *modulate* the ranging code and navigation data. The ranging code allows range measurements using correlation (explained in section 2.3.2.1) and the navigation data is a binary-coded data consisting of satellite health status, ephemeris (satellite position and velocity), clock-bias parameters and an almanac giving reduced precision ephemeris data on all satellites in the constellation.

The GNSS signal presented below corresponds to GPS L1 code signal, representing the most widely used signal. This signal is available to all civilian users and practically all consumer GNSS products track only these signals (Van Diggelen 2009). The GPS L1 signal has a centre frequency of 1575.42 MHz and is modulated by a civilian ranging code (Coarse Acquisition, or C/A) using Code Division Multiple Access (CDMA) techniques (Ward et al 2006 a). The C/A code is also called Pseudorandom or PRN code (Misra and Enge 2011). As explained in section 2.3.2.1, the correlation properties of the C/A code (Parkinson & Spilker 1996, and Ward et al 2006 a) is exploited by a traditional GNSS receiver in order to track the signal and ultimately provide a position solution (Parkinson & Spilker 1996, and Misra and Enge 2011).

GNSS signals reaching directly to the receiver are called Line-of-sight (LOS) signals. On the other hand, GNSS signals reaching receiver after reflections from nearby objects are called

reflected or Non-line-of-sight (NLOS) signal. The LOS-based received signal is presented in this section but NLOS signals, and their effect on GNSS receivers, is deferred until Section 2.5.1.

The received signal is a time delayed version of the transmitted signal along with noise. A typical received GNSS signal ($Y^r(t)$) can be represented as shown in equation (Misra & Enge 2011), with the subscript ‘ $_{LOS}$ ’ indicating the direct (LOS) signal.

$$Y^r_{LOS}(t) = A_{LOS} D x(\tau_{LOS}) \cos(2\pi(f + f^D_{LOS})t + \theta_{LOS}) + \eta_{LOS} \quad (2.1)$$

where D , τ_{LOS} , f^D_{LOS} and θ_{LOS} are all functions of time, and

A : Received signal amplitude

D : Navigation data bit (for GPS data rate: 50 Hz)

$x(\tau)$: Ranging code (C/A chip rate: 1.023 MHz)

τ : Code phase

f : Carrier frequency (1.57542 GHz, for GPS L1 signal)

θ : Carrier phase

f^D : Doppler frequency due to relative velocity between satellite and receiver

η : Composite noise comprised of atmospheric background noise and receiver thermal noise

Since Y_{LOS}^r corresponds to the receipt of only one signal, it is referred to as a single-path signal.

The following sections use the above model to describe how a GNSS receiver acquires and track signals and then computes a position.

2.3 Traditional GNSS Receiver Architecture

The primary objective of a traditional GNSS receiver is to extract the navigation data (D) from minimum four different satellites, to estimate position of the receiver. In order to extract the navigation data, a traditional receiver demodulates the received GNSS signal and generates measurements (explained in section 2.3.3), in order to estimate position of the receiver. More precisely, a traditional GNSS receiver first estimates the unknown *signal parameters* for each satellite consisting of code phase (τ), Doppler frequency (f^D) and, optionally, carrier phase (θ). These parameters are used by the GNSS receiver to generate the measurements and position information (Ward et al., 2006 and Braasch 1999).

A typical GNSS receiver's block diagram is depicted in Figure 2.1 for a single satellite (a receiver will have several such blocks in parallel). The heart of the receiver is the *signal processing* (section 2.3.2) that acquires (using *acquisition* process) and tracks (using *tracking* process) the satellites' signals (Braasch 1999).

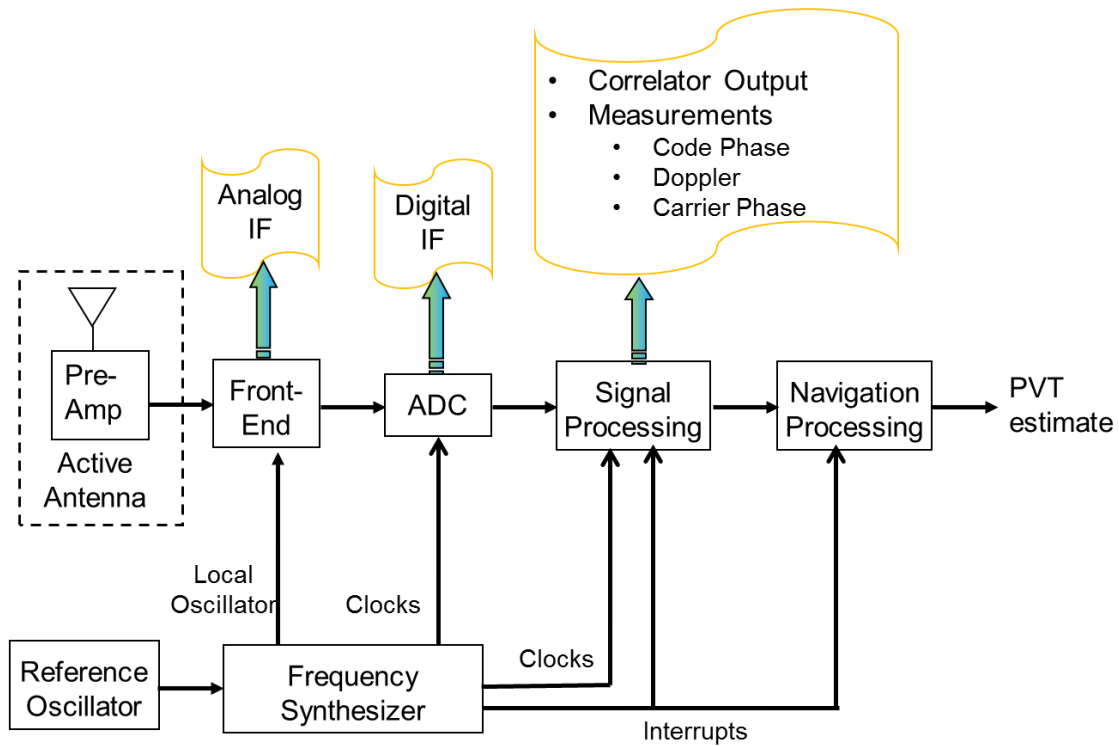


Figure 2.1: Generic GNSS receiver block diagram for a single channel. The colored arrows indicates outputs generated at the corresponding stage

GNSS receiver's task can be divided into the following parts, which are described in more detail in the following sub-sections:

- Radio Frequency (RF) section, to down-convert the incoming high frequency signal to an Intermediate Frequency (IF) signal and then convert the signal to the digital domain using sampling and quantization
- Signal processing, consisting of local signal generation and correlation, acquisition and tracking
- Measurement generation, and
- Navigation solution

2.3.1 RF Section

The RF section consists of an active antenna, and a low noise amplifier, which boosts the desired signal power while adding as little noise and distortion as possible. The active antenna section is followed by a RF front-end, which down converts the incoming signal frequency to IF. The ADC converts the IF signal from analog to digital domain.

2.3.2 Signal Processing

At a high level, the signal processing block of a GNSS receiver aims to replicate the incoming signal as accurately as possible. By extension, this yields the *best* estimate of the unknown signal parameters (τ_{LOS} , f_{LOS}^D and θ_{LOS}). The receiver does this by first generating a local version of the incoming (received) signal, which is then correlated with the incoming signal. The output of the correlation process is then used for signal acquisition then signal tracking. This section describes these various steps in more detail.

2.3.2.1 Local signal generation and correlation

The first step of signal processing is to generate a local replica of the incoming signal. More precisely, an in-phase ($Y_I^l(t)$) and a quadrature-phase $Y_Q^l(t)$ component of the local replica of GNSS signal are generated as shown in equation (2.2) and (2.3) respectively.

$$Y_I^l(t) = Ax(\hat{\tau}) \cos\left(2\pi\left(f + \hat{f}^D\right)t + \hat{\theta}\right) \quad (2.2)$$

$$Y_Q^l(t) = Ax(\hat{\tau}) \sin\left(2\pi\left(f + \hat{f}^D\right)t + \hat{\theta}\right) \quad (2.3)$$

These equations are similar to equation except the fact that the superscript ‘l’ in represents locally generated signal and $\hat{\tau}$, \hat{f}^D and $\hat{\theta}$ are the receiver’s current estimated values for τ_{LOS} , f_{LOS}^D and θ_{LOS} respectively, generated using a Numerically Controlled Oscillator (NCO).

The next step is to *correlate* the received signal with the locally generated signal. This step results in in-phase and a quadrature phase *correlator outputs* corresponding to values of locally generated code phase ($\hat{\tau}$), Doppler (\hat{f}^D) and carrier phase ($\hat{\theta}$).

A simplified block diagram representing the correlation of incoming and locally generated signal is shown in Figure 2.2. Although the signal processing is done on digital IF, for simplicity, the equations presented here corresponds to continuous signal model.

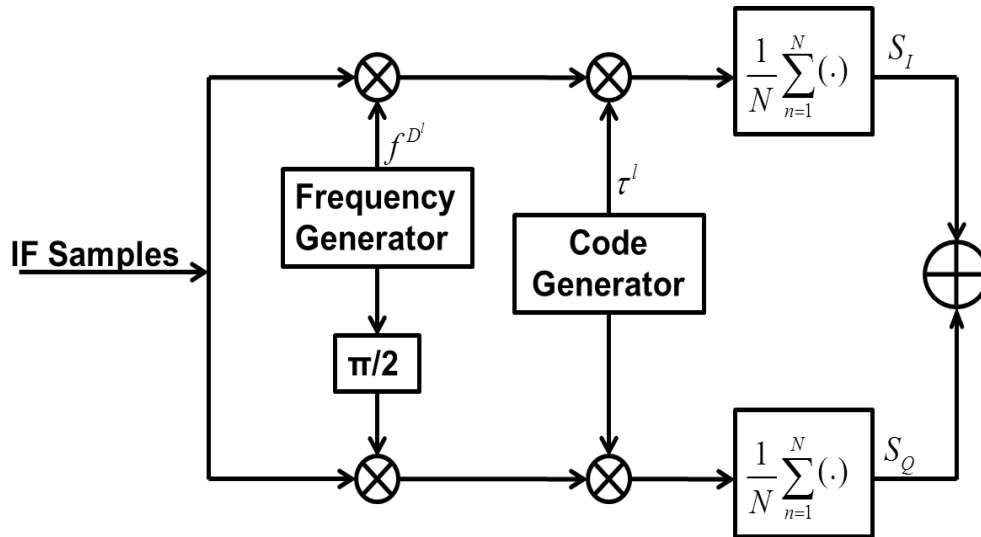


Figure 2.2: Simplified block diagrams of signal acquisition stage. f^{D^l} and τ^l represents Doppler frequency and code phase respectively of locally generated signal. S_I and S_Q are the in-phase and quadrature-phase correlation component respectively.

The in-phase (S_I) and quadrature-phase (S_Q) correlator outputs are respectively given by equation (2.4) and (2.5).

$$S_I = A_R R(\Delta\tau) D \text{sinc}(\pi T_c (\Delta f^D)) \cos(\Delta\theta) \quad (2.4)$$

$$S_Q = A_R R(\Delta\tau) D \text{sinc}(\pi T_c (\Delta f^D)) \sin(\Delta\theta) \quad (2.5)$$

where

A_R : is amplitude of correlated output

$R(\cdot)$: is auto-correlation function of the ranging code

$\Delta\tau$: is difference between received and locally generated code phase,

$\Delta\tau = \tau - \tau_{nc0}$, where τ_{nc0} is locally generated code phase

Δf^D : is difference between received and locally generated Doppler

$\Delta\theta$: is difference between received and locally generated carrier phase

T_c : is coherent integration time (CIT)

The correlator value in equations (2.4) and (2.5) corresponds to one code phase, frequency and carrier phase of locally generated signal. In general, there will be several correlators, each corresponding to a local signal generated with a different code phase and/or frequency. These correlators are used for acquisition and tracking as explained in following sub-section.

2.3.2.2 Signal Acquisition and Tracking

The primary objective of acquisition and tracking is to estimate the unknown parameters (τ_{LOS} , f_{LOS}^D and, optionally θ_{LOS}), which is done in two stages. The first stage is a global search for approximate values of $\{\tau_{LOS}, f_{LOS}^D\}$ which is known as signal acquisition. The second stage is a local/refined search for more accurate estimates of $\{\tau_{LOS}, f_{LOS}^D\}$ and optionally θ_{LOS} , known as signal tracking. If the carrier phase is known with sufficient accuracy, then coherent signal processing can be used (these only need the in-phase correlator outputs), otherwise non-coherent processing (requiring both in-phase and quadrature-phase correlator outputs) is employed. This thesis exclusively considers non-coherent processing.

During signal acquisition, the generated correlator outputs S_I and S_Q are squared and summed to yield the correlator power follows

$$S(t) = S_I^2(t) + S_Q^2(t) = A_R^2 R^2 (\Delta\tau) \text{sinc}^2(\pi T_c (\Delta f^D)) \quad (2.6)$$

The correlator power is compared against a pre-defined threshold (Borio 2012, Misra and Enge 2011) to decide whether a signal with the locally generated signal parameters (f^{D^l} and τ^l) is present or not. Different combinations of Doppler frequencies and code phase are considered until the signal is declared present (signal acquired) or not present (Misra and Enge 2011, Borio 2012). The output of acquisition stage is a coarse estimate of code phase and Doppler, which is used by tracking stage to obtain a fine estimate.

Following acquisition, the receiver transitions to tracking the signal, aiming to refine the acquired signal parameters and, in the process, demodulate the navigation data from the received signal (Borio 2012, Misra and Enge 2011, Van Diggelen 2009). This is achieved using two or three separate feedback loops, namely, Delay Lock Loop (DLL), Phase Lock Loop (PLL) and Frequency Lock Loop (FLL).

Figure 2.3 represents a simplified block diagram of the signal tracking inside a single channel of a traditional GNSS receiver. The code is tracked using the DLL which uses a feedback loop to align the locally generated ranging code with the received signal by minimizing the difference between them. The code tracking loop is shown in light blue blocks in Figure 2.3. DLL consists of a discriminator to find the difference between the local and received code phase and a loop filter, which together provide the feedback to the code phase NCO. The DLL inside a traditional receiver generates three correlators corresponding to Early (E), Prompt (P) and Late (L) versions of the local code replica.

The carrier tracking loop is shown in faded orange blocks in Figure 2.3. The carrier tracking loop also consists of a discriminator and a filter to provide necessary feedback to the carrier NCO. The carrier tracking is done using FLL and/or PLL for tracking frequency and/or phase respectively.

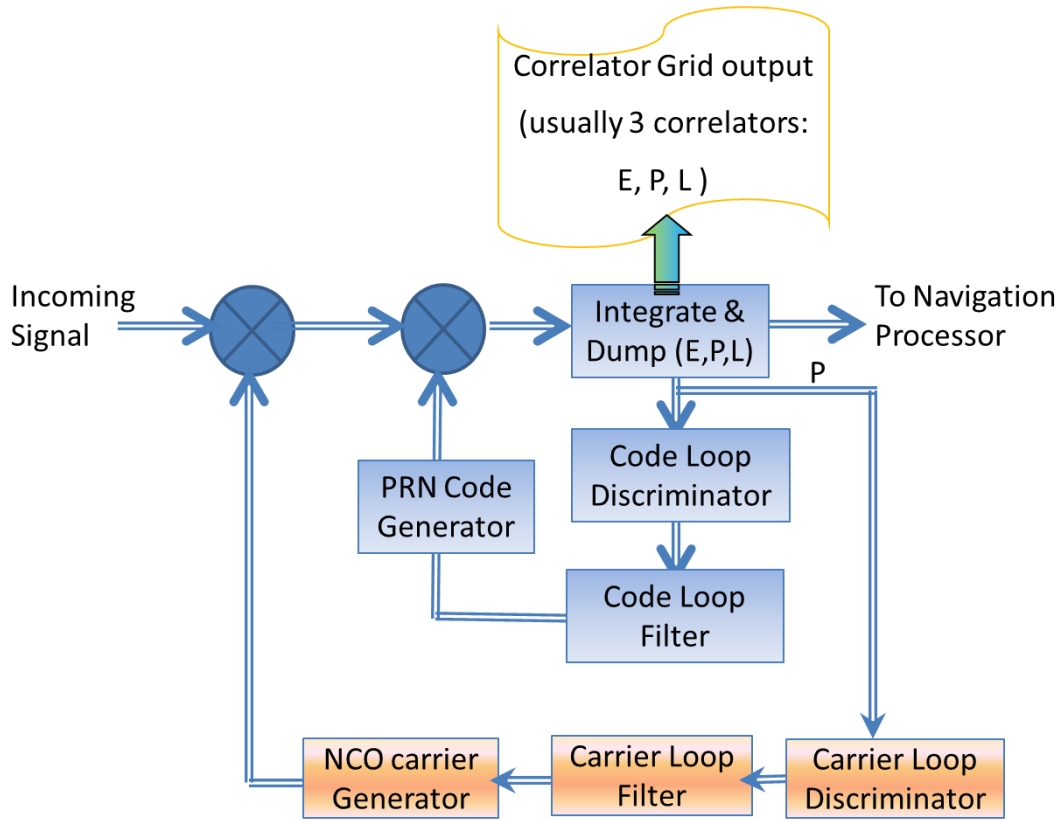


Figure 2.3: Simplified block diagrams of signal tracking inside a traditional GNSS receiver. Usually there are 3 such loops each for early, prompt and Late correlators, however, for simplicity only one loop (for Prompt i.e. P) is shown.

The proposed research is based on the correlator power given by equation (2.6), which is re-written as follows

$$S(t) = S_I^2(t) + S_Q^2(t) = A_1^2 \cdot R^2(\Delta\tau) \quad (2.7)$$

where $A_1 = (\text{sinc}(\pi T_c(\Delta f^D))) \cdot A_R$ represents the *effective* amplitude of the signal after correlation. It is interesting to note that equation (2.7) is free from phase information, which is

the main reason for adopting this approach; it avoids the need to track the carrier phase of the incoming signal.

Finally, due to the fact that GNSS satellites are always in motion, the receiver has to continuously acquire (new satellites or lost satellites) and track the signals from the satellites in view, to compute an uninterrupted position solution. After synchronization of the locally generated carrier and code with the incoming signal, the navigation data is demodulated. Once the navigation data is decoded the traditional receiver computes the measurements (code phase, Doppler and carrier phase measurements) corresponding to each tracking satellite (Misra & Enge 2011, Ward and Hegarty 2006). Since this research focuses on code phase data, the generation of code phase measurement is presented in following sub-section. Interested readers can refer (Misra and Enge 2011) for details on carrier phase-based measurement and positioning.

2.3.3 Measurement Generation

In a traditional receiver, a pseudorange measurement is generated by differencing the transmit time of the current signal (i.e., the time the currently received signal was transmit from the satellite) from the receiver's current estimate of time and scaling by the speed of light. This is written mathematically as follows:

$$\rho_i(t) = c(t_{rx}(t) - t_{tx}^i(t)) \quad (2.8)$$

where c is the speed of light, $t_{rx}(t)$ is the estimated receiver time and $t_{tx}^i(t)$ is the transmit time.

The transmit time is computed as the sum of three components:

- Transmit time within one navigation data bit (T_{Bit}^i ; 20 ms in the GPS C/A case)

- Number of ranging code periods into the current data bit (N_{PRN}^i : equivalent to number of milliseconds into the current bit in the GPS C/A case)
- Estimated code delay ($\hat{\tau}^i$) and ranging code's chipping rate (f_c^i)

$$t_{tx}^i = T_{symbol}^i + N_{PRN}^i \cdot T_{PRN} + (\hat{\tau}^i / f_c^i) \quad (2.9)$$

where 'i' represents values corresponding to ith satellite and T_{PRN} is the duration of the period code (1 ms in case of GPS L1 C/A).

In addition to allowing for the computation of a pseudorange measurement, computing the transmit time using equation (2.9) means that the precise position of the satellite at the true time of transmission can be computed. This concept becomes important when discussing coarse-time problem in Section 2.4.2.1.

For estimating position, the following pseudorange measurement model is used

$$\rho_i(t) = r + c(b_{rx} - b_{tx}) + I_p + T_p + \varepsilon_p \quad (2.10)$$

where r is true geometric range, b_{rx} is receiver clock bias, b_{tx} is satellite clock bias, I_p and T_p are delay associated with transmission of signal through ionosphere and troposphere respectively, and ε_p is propagation delay associated with any unmodeled error (effect of multipath will be addressed in Section 2.5). These generated measurements are used by navigation processor to estimate the position of the receiver.

2.3.4 Navigation Solution

This section briefly describes the position computation using pseudorange observations usually done in traditional receivers (Misra & Enge 2011, Pany 2010 and Van Diggelen 2009). The simplified process of obtaining a navigation solution using an estimator consists of the following steps:

1. Start with an a-priori estimate of receiver position (X_{rx_0})
2. Predict the pseudorange observations ($\hat{\mathbf{Z}}$) at X_{rx_0} , where $\hat{\mathbf{Z}}$ is a vector of 'n' predicted pseudoranges ($\hat{\rho}$) (equation) at X_{rx_0} , corresponding to 'n' different satellite. $\hat{\mathbf{Z}}$ is shown in equation (2.11).

$$\hat{\mathbf{Z}} = [\hat{\rho}_1 \quad \cdots \quad \hat{\rho}_n] \quad (2.11)$$

3. Get the actual observations (\mathbf{Z}), where \mathbf{Z} is a vector of 'n' received pseudorange (ρ) corresponding to 'n' different satellites as shown in equation (2.12).

$$\mathbf{Z} = [\rho_1 \quad \cdots \quad \rho_n] \quad (2.12)$$

4. Update the a-priori position estimate using the difference between the actual and predicted measurements, also called the misclosure vector ($\delta\mathbf{Z} = \mathbf{Z} - \hat{\mathbf{Z}}$). This update step is given by equation

where X represents states ($\mathbf{X} = [X_{rx_0} \quad b]$); b is receiver clock bias; and δX is the error in the current estimate of the state

$$\delta \mathbf{Z} = \begin{bmatrix} \delta \rho_1 \\ \delta \rho_2 \\ \delta \rho_3 \\ \vdots \\ \delta \rho_k \end{bmatrix} = \begin{bmatrix} -e_1 & 1 \\ -e_2 & 1 \\ -e_3 & 1 \\ \vdots & \vdots \\ -e_k & 1 \end{bmatrix} \begin{bmatrix} \delta X_{rx} \\ \delta b \end{bmatrix} + \varepsilon \quad (2.13)$$

where

- $\delta \rho_k$: A-priori pseudorange residual for kth satellite
- e_k : Unit vector from the a-priori position to the satellite
- $\delta X_{rx} = [\delta x \quad \delta y \quad \delta z]^T$: Position state error;
- δb : Receiver clock bias error update
- $\delta X = [\delta X_{rx} \quad \delta b]^T$: State error update
- ε : Measurement errors (Misra & Enge 2011)

Provided there are sufficient number of independent measurements (Misra and Enge 2011), equation can be solved for the state update using a LSQ, KF or any other estimator. The LSQ solution can be denoted as shown in equation (2.14):

$$\delta X = (H^T W^{-1} H)^{-1} H^T W^{-1} \delta Z \quad (2.14)$$

where, H is the observation matrix given by equation (2.15) and W is covariance matrix (Misra & Enge 2011, Van Diggelen 2009, Petovello 2003)

$$H = \begin{bmatrix} -e_1 & 1 \\ -e_2 & 1 \\ -e_3 & 1 \\ \vdots & \vdots \\ -e_k & 1 \end{bmatrix} \quad (2.15)$$

After each iteration, the state (X) is updates as shown in equation (2.16).

$$X = X + \delta X \quad (2.16)$$

It is obvious from above equations that any error in the pseudorange from any satellite would lead to wrong position estimate.

2.4 Special GNSS Receivers

In the context of this thesis, two other kinds of GNSS receivers are explained. These two receivers are high sensitivity GNSS receivers and snapshot GNSS receivers, which perform tracking and/or positioning in different ways than a traditional receiver. A brief working principle of these special GNSS receivers is presented in the following sub-sections.

2.4.1 High Sensitivity GNSS Receivers

In context of this thesis, a high sensitivity receiver is a special GNSS receiver which is different than the traditional GNSS receiver as follows:

- Longer coherent integration time (longer than the navigation data bit duration) to improve the sensitivity (in terms of C/N_0) of the acquired signal (Van Diggelen 2009). In traditional GNSS receivers, the coherent integration time is limited by duration of navigation data bit.

- The tracking is based on open loop architecture (Van Graas et al 2009, Uijt de Haag 1999) as shown in Figure 2.4, which is different than the tracking loops inside a traditional GNSS receiver (Figure 2.3).

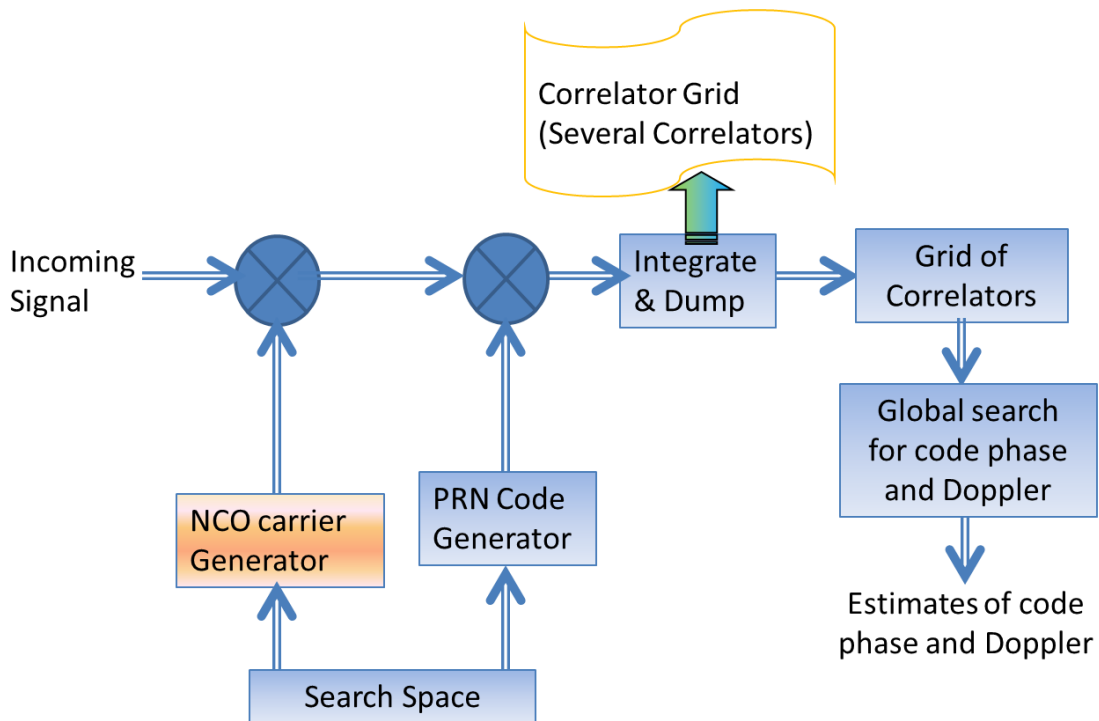


Figure 2.4: Simplified block diagrams of open loop architecture-based GNSS receivers

An open loop architecture for signal processing is similar to the acquisition process in traditional receivers. More specifically, unlike in traditional receivers where (typically) three correlators (early, prompt and late) are generated for tracking the signal, a grid of correlators are generated in the open loop processing case, each corresponding to a correlation of the received signal with local signals generated using different code phase and Doppler.

Since the receiver uses longer coherent integration and is based on open loop processing, the following advantages and disadvantages are apparent for the high sensitivity receiver in context of this research:

- The receiver is capable of tracking a weaker signal due to longer coherent integration (Van Diggelen 2009); however, external data bit aiding is required in order to achieve longer coherent integration time, making the receiver implementation more complex.
- The open loop architecture eliminates the use of local channel filters (code and carrier) which in turn evades any filter stability issues. However, due to large number of correlators used, the computational load increases (Van Graas et al 2009, Uijt de Haag 1999).

2.4.2 Snapshot-based Positioning Method

In the context of GNSS, a “snapshot” is a short recording (few milliseconds) of the digitized IF signal in the front-end. As opposed to traditional receivers, where the receiver runs continuously to track a minimum of four satellites to provide a PVT estimate, a snapshot receiver computes the PVT solution using only a few milliseconds of IF data (Qian et al 2008, Knight et al 1998). Typically, in snapshot mode, a receiver hibernates most of the time in order to save power. When a position fix is requested, the receiver takes a snapshot of incoming signal samples and then calculates the position fix from these samples, either directly on the device or using an off-site processor.

2.4.2.1 Coarse Time Problem

As discussed in section 2.3.3, a traditional receiver computes the pseudorange measurement using the computed transmit time, which can be computed after decoding navigation data. However, snapshot techniques do not use enough data to allow the navigation message to be decoded, thus preventing computation of the transmit time of the currently received signal. The inability to compute transmit time has two main consequences.

First, pseudorange measurements cannot be generated. This is not particularly problematic since code phase measurements can also be used for position determination. Second, and more important for the current discussion, the position of the satellite requires that the transmit time be *estimated* from the receiver's current time. However, since the receiver time is, in general, incorrect, the estimated transmit time is also incorrect by the same amount as the receiver time. In turn, this results in a ranging error that is proportional to the product of the range rate to the satellite and the receiver timing error ($\dot{\rho} \cdot \delta t_{rx}$) where δt_{rx} is error in transmit time and $\dot{\rho}$ is range rate. Satellite motion induces range rates of up to 800 m/s for a static receiver, which implies ranging errors of hundreds of metres per second of receiver timing error. Moreover, since range rates to different satellites are different, the error is not common between measurements. This problem is typically referred to as the coarse-time problem and is usually solved by adding an extra coarse-time state to the navigation filter, briefly explained in section 2.4.2.2.

2.4.2.2 Coarse Time Navigation

The navigation solution in case of coarse time error would be similar to that presented above in section 2.3.4, except with following changes due to inclusion of the coarse time error (δ_{T_c}) into the state vector:

State error update:

$$\delta X = [\delta X_{rx} \quad \delta b \quad \delta_{T_c}] \quad (2.17)$$

$$\delta Z = \begin{bmatrix} \delta z_1 \\ \delta z_2 \\ \delta z_3 \\ \vdots \\ \delta z_k \end{bmatrix} = \begin{bmatrix} -e_1 & 1 \\ -e_2 & 1 \\ -e_3 & 1 \\ \vdots & \vdots \\ -e_k & 1 \end{bmatrix} \begin{bmatrix} \delta X_{rx} \\ \delta b \end{bmatrix} + \begin{bmatrix} v_1 \\ v_2 \\ v_3 \\ \vdots \\ v_k \end{bmatrix} \cdot \delta_{T_c} + \varepsilon \quad (2.18)$$

$$H = \begin{bmatrix} -e_1 & 1 & v_1 \\ -e_2 & 1 & v_2 \\ -e_3 & 1 & v_3 \\ \vdots & \vdots & \vdots \\ -e_k & 1 & v_k \end{bmatrix} \quad (2.19)$$

where v_k is range rate for corresponding to k^{th} satellite.

The final state estimate can be computed in similar way as in equation (2.14), but the required number of independent measurements would be increased by one, due to additional state. By extension, this could be a limiting factor and a challenge in urban environments, due to poor satellite visibility.

2.5 Effect of Urban Environments on GNSS Receivers

Until now, all of the received signals were considered to consist of a direct LOS signal only, and no reflected signals were considered. In urban environments, however, due to surrounding buildings, a GNSS receiver might receive one or more NLOS signals and may or may not receive the LOS signal. Due to presence of NLOS signal(s) and signal blockages, a traditional receiver might not provide a position solution or provides poor quality position solution. In order to explain this, the following section details the signal characteristics in a typical urban environments, followed by its effect on GNSS receivers.

2.5.1 GNSS Signal Characteristics in Urban Areas

In urban canyons some of the signals are blocked, some of signals are reflected and some are received directly. A typical signal reception in urban canyons is depicted in Figure 2.5.

In typical urban environment, a receiver receives a composite signal comprising of LOS (possibly) and one or more non-LOS (NLOS) signals. Mathematically, the composite signal resulting from an LOS and ‘ n ’ NLOS signals, can be written as

$$Y_{composite}^r(t) = Y_{LOS}^r(t) + \sum_1^n Y_{NLOS_k}^r(t) + \eta_{composite} \quad (2.20)$$

where $Y_{LOS}^r(t)$ is defined in equation and $Y_{NLOS_k}^r(t)$ is the received signal corresponding to k^{th}

NLOS signal as defined below

$$Y_{NLOS_k}^r(t) = A_{NLOS_k} Dx(\tau_{NLOS_k}) \cos(2\pi(f + f_{NLOS_k}^D)t + \theta_{NLOS_k}) + \eta_{NLOS_k} \quad (2.21)$$

where all the terms have same meaning as in equation and the subscript ‘ τ_{NLOS_k} ’ denotes the k^{th} NLOS signal.

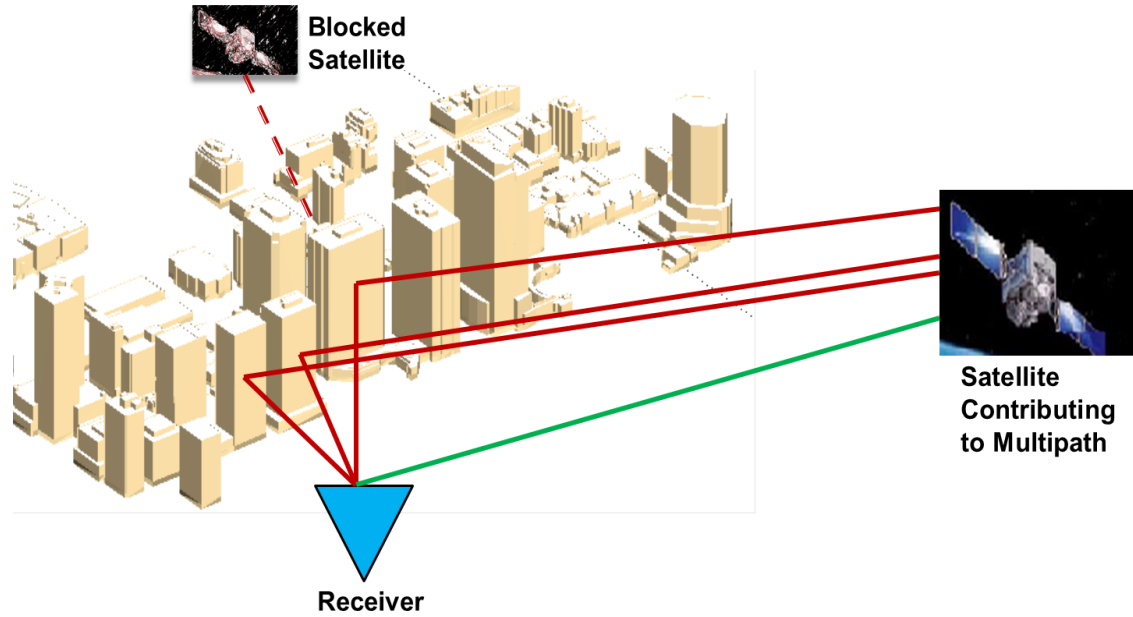


Figure 2.5: Signal reception in a typical urban environment. Green line indicates LOS signal, red lines indicate NLOS signals from a satellite, and dashed red line represents blocked signal from another satellite. Because of LOS signal and NLOS signal(s), three in this case, from same satellite, a receiver receives the composite signal in urban environment. These composite signals results in multipath effect at receiver.

Also, by definition, the NLOS signal is time delayed with respect to the LOS signal; hence τ_{NLOS} for the k^{th} satellite is different than τ_{LOS} for the same satellite

$$\tau_{NLOS} = \tau_{LOS} + \delta\tau \quad (2.22)$$

where $\delta\tau$ is referred as the *delta path delay*. Similarly, the difference between NLOS signal phase and LOS signal phase for the same satellite is referred as *delta phase* ($\delta\theta$):

$$\theta_{NLOS} = \theta_{LOS} + \delta\theta \quad (2.23)$$

Since $Y_{composite}^r$ consists of an LOS signal in addition to ‘k’ NLOS signals, it is referred as a (k+1)-path signal; more generally, this can be called a N-*path* (multipath) signal. By extension if k=1, $Y_{composite}^r$ represents a two-path signal and if k=2 then $Y_{composite}^r$ represents a three-path signal, and so on. It is also worth mentioning here that two-path (and by extension higher-path) signals need not necessarily include LOS signal, but in the absence of LOS signal $Y_{composite}^r$ would represent a two-path case for k=2 (not k=1, as above).

Comparing equation (2.1) and equation (2.20), it follows that a traditional GNSS receiver unaware of a higher number of signal paths ends up extracting wrong signal parameters and hence provides wrong position estimates. This is explained in more detail in the following subsection, for the specific case of a two-path case.

2.5.2 Effect of a Two-Path Signal on the Signal Processing of a Traditional GNSS Receiver

The effect of a two-path signal on a traditional receiver can be related to the signal processing acquisition as described in section 2.3.2 More precisely, due to additional signal paths in $Y_{composite}^r$ (equation (2.20)), as compared to Y_{LOS}^r (equation (2.1)), the signal acquisition and tracking (section 2.3.2.2) ends up extracting an erroneous code phase estimate ($\hat{\tau}$) that, in turn, produces a wrong pseudorange measurement and, by extension, a wrong position estimate. More precisely,

the effect of a two-path signal on erroneous navigation solution can be associated with the wrong estimate of signal parameters (such as $\hat{\tau}$). In order to elaborate on this the correlator model in presence of two-path signal is explained first.

The in-phase and quadrature-phase correlator output for a two-path signal is shown in equations (2.24) and (2.25) respectively; For simplicity, the navigation data is excluded from the equation, since the effect of NLOS is seen in the cross-correlation function, as shown later in this section.

$$S_I(t) = A_1 R(\Delta\tau_1) \cos(\Delta\theta_1) + A_2 R(\Delta\tau_2) \cos(\Delta\theta_2) \quad (2.24)$$

$$S_Q(t) = A_1 R(\Delta\tau_1) \sin(\Delta\theta_1) + A_2 R(\Delta\tau_2) \sin(\Delta\theta_2) \quad (2.25)$$

where A_k is the effective amplitude of k^{th} -path signal after correlation; $\Delta\tau$ and $\Delta\theta$ are difference between locally generated and estimated code phase and carrier-phase, $\Delta\tau_k = \tau_k - \tau_{nc0}$ is mismatch between local and received code phase; τ_{nc0} is locally generated code phase; $\tau_k = \tau_1 + \delta\tau$ is k^{th} path signal ($k>1$) and τ_1 is smallest delay.

Squaring and summing equations 2.24 and 2.25 removes the dependence on the input phase (Borre et al., 2006) and the result is given by equation (2.26).

$$\begin{aligned} S(t) &= S_I^2(t) + S_Q^2(t) \\ &= \underbrace{A_1^2 R^2(\Delta\tau_1)}_1 + \underbrace{A_2^2 R^2(\Delta\tau_2)}_2 \\ &\quad + \underbrace{2A_1 A_2 R(\Delta\tau_1) R(\Delta\tau_2) \cos(\delta\theta_{12})}_3 \end{aligned} \quad (2.26)$$

where, $\delta\theta_{1k}$ is delta phase of k^{th} path signal ($k>1$).

Before moving forward, note the following points regarding equation (2.26):

1. This correlator model ($S_I^2(t) + S_Q^2(t)$) is independent of absolute phase of LOS and NLOS signals
2. In absence of higher-path signals (two-path, three-path etc.), the correlator output corresponds to 1st part of equation (2.26), i.e. the 2nd and 3rd terms in equation are due to presence of one additional path. In other words, equation (2.7) is a special case of equation (2.26) with $A_2 = 0$.

The correlator outputs for a LOS-only signal (one-path signal), NLOS-only signal and sum of the two, i.e. composite signal (two path signal), are shown in Figure 2.6 for two cases; one where NLOS signal is in-phase with LOS signal (top plot) and other where NLOS signal is in opposite phase of LOS signal (bottom plot).

From Figure 2.6, it is apparent that the correlator outputs have a very different shape in the presence of NLOS signals compared to the desired LOS-only case. That means the estimated signal parameters using a traditional receiver would be different for the composite signal as compared to the LOS only signal. Moreover, the effect of the in-phase and opposite-phase NLOS signals on the composite signal is entirely different. Hence, the traditional receiver, which effectively extracts the code phase measurement corresponding to the prompt (P) correlator after balancing the power in the early (E) and late (L) correlators, would be wrong as compared to the true code phase (corresponding to the peak of LOS only signal).

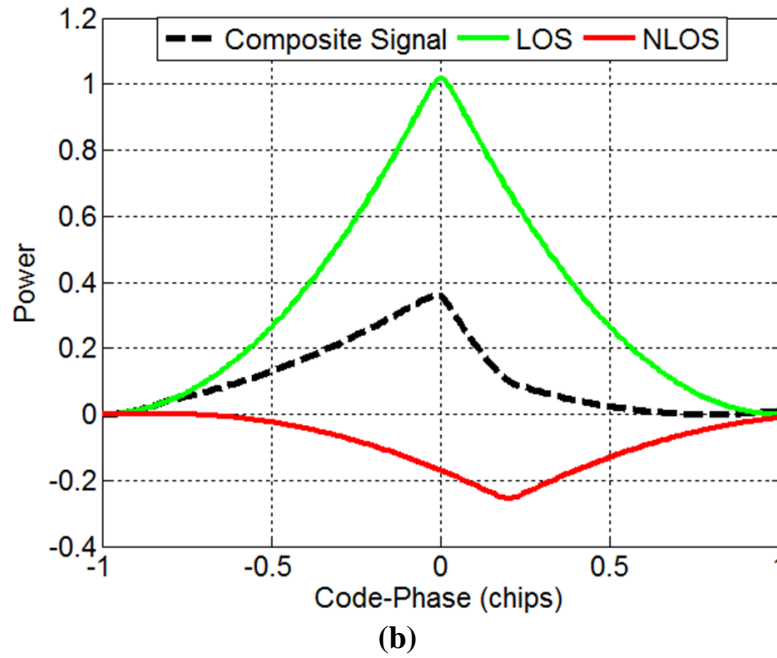
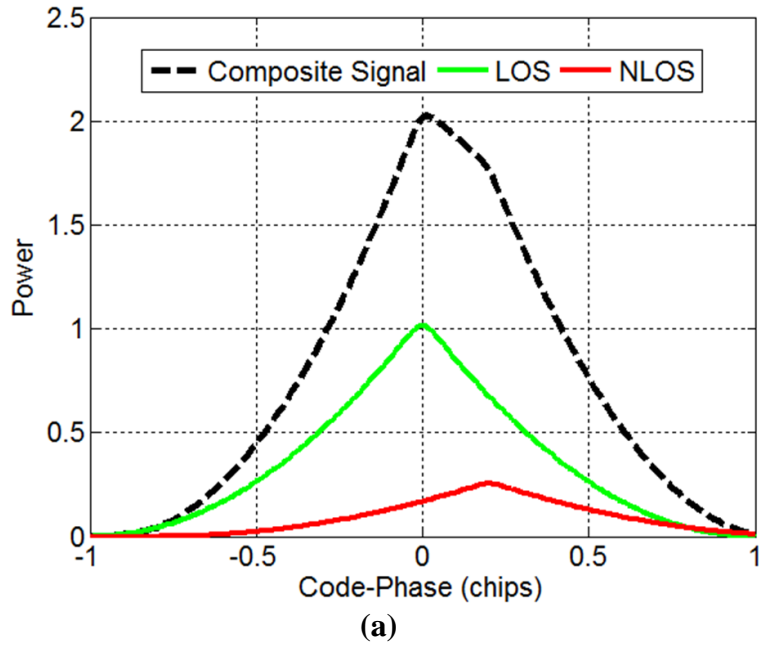


Figure 2.6: Correlator outputs corresponding to LOS and NLOS signals. Figure (a) represents a case for NLOS signal, in-phase with LOS signal. Figure (b) represents a case when NLOS signal is in opposite phase of LOS signal.

Furthermore, the receiver might receive many NLOS signals with different phases relative to the LOS signal, resulting in a more complex composite signal, very different from the LOS signal's correlator output.

As an example the correlator model for a three path signal is shown in equation (2.27)

$$\begin{aligned}
S(t) &= S_I^2(t) + S_Q^2(t) \\
&= A_1^2 R^2(\Delta\tau_1) + A_2^2 R^2(\Delta\tau_2) + A_3^2 R^2(\Delta\tau_3) + \\
&\quad 2A_1 A_2 R(\Delta\tau_1) R(\Delta\tau_2) \cos(\delta\theta_{12}) \\
&\quad + 2A_2 A_3 R(\Delta\tau_2) R(\Delta\tau_3) \cos(\delta\theta_{23}) + \\
&\quad 2A_1 A_3 R(\Delta\tau_1) R(\Delta\tau_3) \cos(\delta\theta_{13}) + \zeta
\end{aligned} \tag{2.27}$$

Similar to the two path case above, it is evident that due to the two additional paths, a traditional receiver will estimate the wrong signal parameters resulting in erroneous position estimates.

Having explained the basic signal processing steps of a traditional receiver and the effect of NLOS signals on the performance of the traditional receiver, a brief description of 3D building models and their application in urban canyon is presented below.

2.6 3D Building Models and Ray-Tracing for Multipath Environments

According to a United Nations study (United Nations 2014), the number of people living in urban areas is steadily increasing. It follows that positioning and navigation in urban areas is also increasing. Due to challenges involved with GNSS-based positioning in urban areas, use of 3D Building Models has received more attention in recent years. In addition, with more accessible location-based and personal navigation services now available to the general public, the need for automated, realistic, and efficiently-generated 3D models has become more urgent than ever

(Brenner, 2005). This section provides an introduction to 3DBMs and their applications along with a ray-tracing method.

2.6.1 3D Building Models

3D building models or 3DBMs consists of geospatial information of an area. The base features for a building model, are undoubtedly the surface model of the area, as well as ortho-imagery which can be used to add texture information to the model. In addition to these crucial layers, most models contain roads, trees, parks, and street signs (Ranzinger, 1997). Common methods of obtaining three-dimensional positional information for the 3D model features are photogrammetry, LiDAR (Light Detection and Ranging), and surveying techniques (Kwak 2013, Habib et al 2007 and Jensen et al 1994,). This thesis does not involve generation of a 3DBM, but rather focuses on the application of 3DBMs to GNSS positioning in urban canyons.

In general, 3DBMs consists of a number of triangles (more generally, polygons), where each triangle represents part of the face of a building. Each triangle is associated with three vertices containing 3D Cartesian coordinates. These coordinates are used along with a ray-tracer to determine if a particular surface can reflect a signal from a particular satellite, towards the user.

2.6.2 Ray-tracing Technique

3DBMs can be used in conjunction with a ray-tracing algorithm to find information about LOS and NLOS signals (Bradbury et al 2007 and Lau & Cross 2007). In context of the proposed research, ray tracing is a method to simulate the *ray* from a satellite to the receiver. While doing so a ray-tracer can provide the following information corresponding to each ray:

- Whether the ray reaches the receiver directly or not (i.e. LOS signal is present or not)

- If the ray reaches the receiver after being reflected (i.e. if there is NLOS signal or not)
 - Find number of such reflected (NLOS) signals reaching the receiver
 - Compute the delta path delay of each NLOS signal

In order to accomplish above tasks, a basic ray tracer launches a signal from each satellite towards each triangle and checks for all possible ray-triangle intersections before it reaches the receiver. This is done using the following steps:

1. Find Normal to the Plane, which is formed by vertices of the triangle:

The first step in a ray-tracing algorithm is to construct the equation of the plane corresponding to each triangle, given the coordinates of the vertices of the triangle from the 3DBM. Given a plane formed by vertices \mathbf{a} , \mathbf{b} and \mathbf{c} , the normal (\mathbf{n}) to the plane can be obtained using:

$$\mathbf{n} = (\mathbf{b} - \mathbf{a}) \times (\mathbf{c} - \mathbf{a}) \tag{2.28}$$

where $(\mathbf{b} - \mathbf{a})$ and $(\mathbf{c} - \mathbf{a})$ are vectors defining two edges of the polygon.

The normal is used to find the incidence and reflected angle for the ray launched from the satellite towards each triangular face.

2. Find Valid Reflectors and Reflected Rays:

The objective of this step is to find whether or not the ray reaches the receiver after reflecting from triangular face. If the ray reaches the receiver, then a reflection is declared for that satellite and the corresponding face is declared as a *reflector*. The process is repeated for all triangles

inside the building model and for all satellites. The critical step involved in this process is to find the ray-triangle intersection, which is explained briefly below.

Ray-triangle intersection:

Consider a plane as defined in equation (2.29)

$$a_1x + b_1y + c_1z = d \quad (2.29)$$

The coefficients a_1 , b_1 and c_1 define the normal to the plane, $\mathbf{n} = [a_1 \ b_1 \ c_1]^T$; hence the plane equation can be written as in (2.30):

$$\mathbf{n} \cdot \mathbf{X} = d \quad (2.30)$$

where $\mathbf{X} = [x \ y \ z]^T$.

Defining the ray $\mathbf{R}(t)$ as in (2.31), the unknown value of t can be computed as shown in (2.32)

$$\mathbf{R}(t) = P + t\mathbf{d} \quad (2.31)$$

where P is the origin of the ray launched in the direction \mathbf{d} and the unknown; t can be solved by substituting $\mathbf{X} = \mathbf{R}(t)$ in equation (2.31) and

$$t = (d - \mathbf{n} \cdot P) / (\mathbf{n} \cdot \mathbf{d}) \quad (2.32)$$

The case $\mathbf{n} \cdot \mathbf{d} = 0$ implies that direction \mathbf{d} is parallel to the plane and the ray would not intersect the plane.

The intersection point Q can be obtained by plugging the resulting t into ray equation. Finally, the intersection point needs to be checked to see whether it is inside the plane of the triangle or not.

All triangles which satisfy the above ray-triangle intersection criteria are declared as reflectors and corresponding rays reaching the receiver after intersecting the polygon, as reflected rays.

A similar ray-triangle intersection can be followed to identify if the LOS signal from a particular satellite reaches the receiver or not. If the LOS ray reaches the receiver then the LOS is declared present else LOS is declared absent.

Figure 2.7 illustrates an output of the ray-tracer developed as part of this work. The blue star indicates receiver position, green face indicates the valid reflector and red face indicates a reflector from which the reflected rays cannot reach the receiver. Yellow rays indicate all the rays from satellite.

After having identified a reflector for a given satellite at a given user location, the next step is to compute the delta path delay of the reflected signal, as explained in the next step.

3. Find Path Delay of Reflected Rays:

In order to calculate the delta path delay of the reflected signal, a delay model is used as defined in (Ebner 2008). For a single bounce case, the delta path delay ($\delta\tau$), can be written as below for a scenario depicted in Figure 2.8

$$\delta\tau = 2 \cdot D \cdot \cos \theta \quad (2.33)$$

where,

D : Distance to the receiver measured perpendicular to the reflector plane

θ : Angle of incidence, which can be found by doing cross product of satellite-triangle ray and normal to the plane

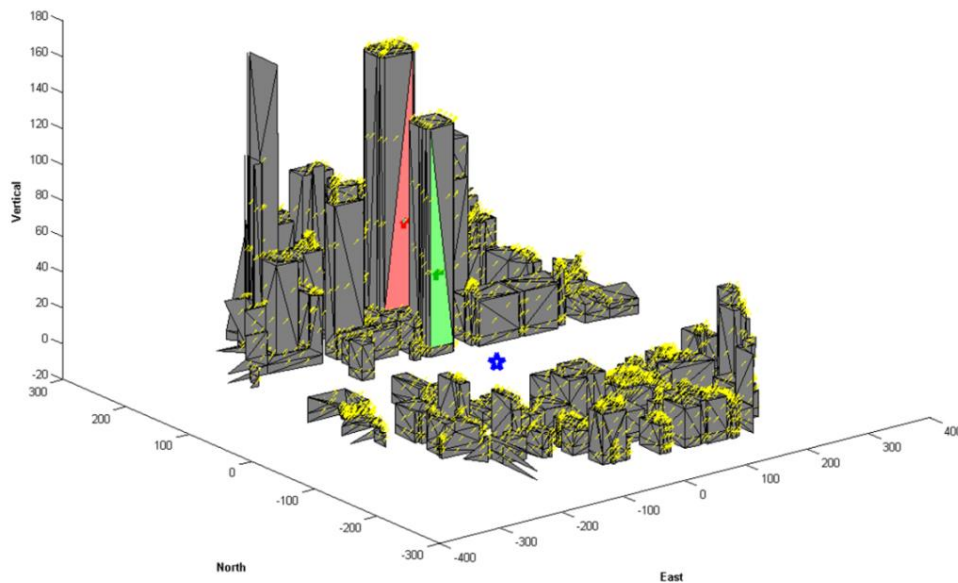


Figure 2.7: Example of ray-tracer output for a single satellite. The blue star indicates receiver position, green face indicates the valid reflector and red face indicates a reflector from which the reflected rays cannot reach the receiver. Yellow rays indicate all the rays from satellite.

In summary, using a 3DBM and a ray-tracer, the following information can be obtained:

- If the receiver receives a LOS signal from the satellite or not
- Number of NLOS signals reaching the receiver from a satellite and delta path delay of each NLOS signal
-

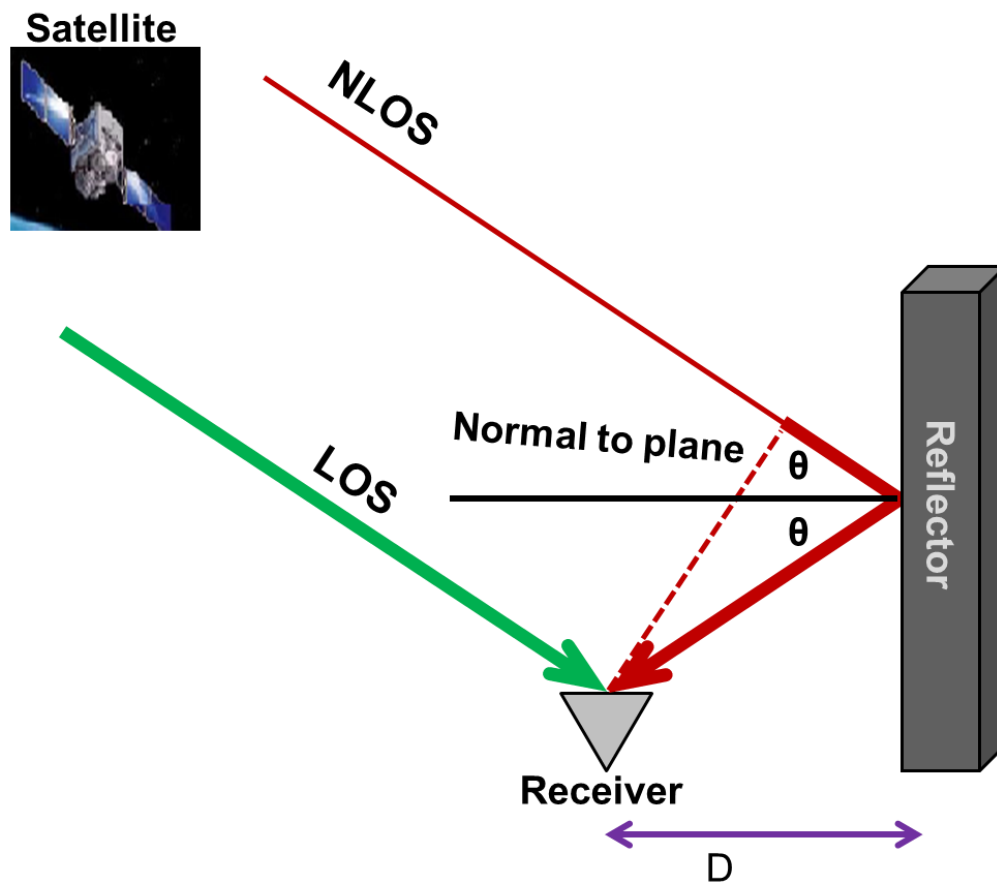


Figure 2.8: Scenario where a receiver receives a multipath signal. The receiver is at a normal distance of 'D' from the reflector. θ is the angle of incidence, which is a function of azimuth and elevation for a 3D case

2.7 Summary

This chapter provided the required technical background required to understand the methodology presented in chapter 3. The chapter described one-path and two-path GNSS signals in detail. It also described the operation of a traditional GNSS receiver, a high-sensitivity receiver based on longer coherent integration time, and open loop processing receivers. Snapshot GNSS receivers, along with their associated coarse time navigation problem was also described. Finally the chapter introduced 3DBMs and ray-tracing methods and their applications to extract some of multipath signal information.

Due to presence of NLOS signals and multipath signals, a traditional GNSS receiver ends up estimating erroneous navigation solution, due to distorted correlator shapes. However, a 3DBM and a ray-tracer can provide relevant information related to multipath signals such as if LOS signal is present or not, the number of NLOS signals and delta path delay of each NLOS signal, all of which are unknown in case of a traditional GNSS receiver. By extension, this information can be used as *a priori* information which is basis of the proposed methodology presented in detail in Chapter 3.

More specifically, Chapter 3 introduces a novel positioning method based on a snapshot of GNSS data that constructively utilizes all NLOS signals with the help of 3DBM. Results based on data collected in downtown Calgary are shown in Chapter 4 and Chapter 5 assesses the sensitivity of the algorithm to various processing parameters.

Chapter Three: **Methodology**

This chapter provides the detailed methodology for the proposed positioning algorithm that uses snapshots of GNSS data and utilizes all NLOS signals with the help of a 3DBM. The fundamental principle of the algorithm is based on matching *predicted* and *observed* signal parameters, using a novel *Signal Delay Matching* (SDM) algorithm. The required background to understand the proposed algorithm was provided in the previous chapter (Chapter 2). The proposed methodology inherently involves multipath parameter estimation using a 3DBM, which was researched as part of this thesis. Hence the chapter first describes a method for 3DBM-assisted multipath parameter estimation followed by the positioning algorithm, which utilizes the estimated multipath parameters.

3.1 3DBM-Assisted Multipath Parameter Estimation

The primary objective of this section is to present a methodology for multipath parameter estimation using 3DBM data and to validate its accuracy. In order to do so, the section is further divided into two main sub-sections; one explaining the methodology and another validating the methodology.

3.1.1 Methodology for 3DBM-Assisted Multipath Parameter Estimation

At a high level, the 3DBM-assisted multipath parameter estimation process can be depicted as shown in Figure 3.1 and consist of two parts: first, predicting the number of NLOS signals and their corresponding delta path delay(s), collectively referred as *predicted signal parameters* in this thesis, and second, estimating the unknown multipath parameters using the predicted parameters as *a priori* information to an *estimator*.

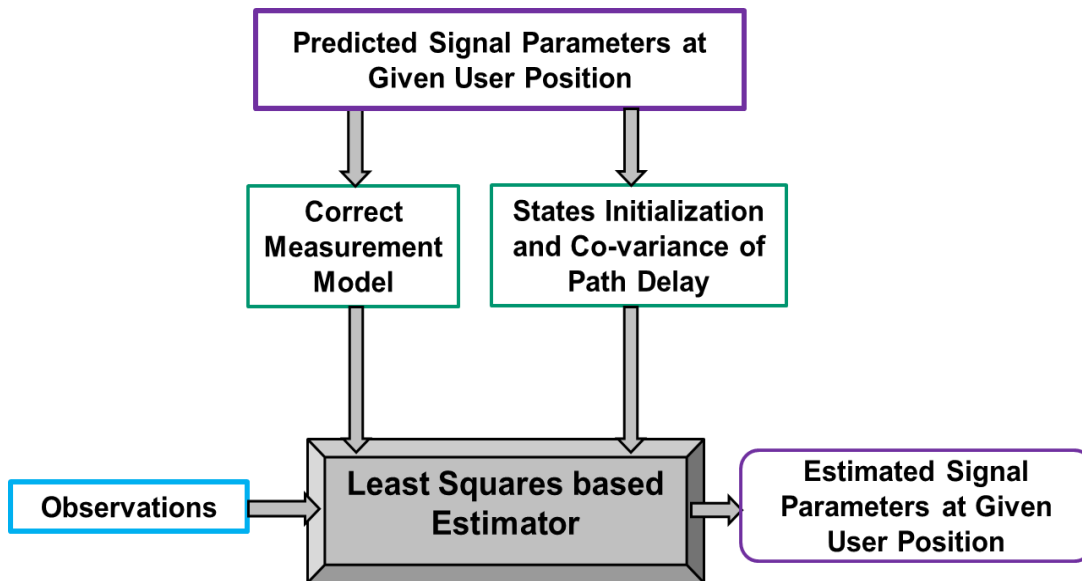


Figure 3.1: Block diagram depicting Least-Squares fit of the observed correlators with the help of predicted signal information

The estimation of multipath parameters involves following steps:

1. Use the 3DBM to compute predicted signal parameters, as described in Section 3.1.1.1
2. Obtain observed signal parameters from correlator outputs of a GNSS receiver
3. Use a least-squares estimator to estimate multipath parameters using observations and using predicted signal parameters as aiding information to the estimator

The details of generating observed signal parameters is deferred until section 3.2.2; the predicted signal parameter generation and the process of multipath parameter estimation are described below.

3.1.1.1 Predicted Signal Parameters

As described in section 2.6, a 3DBM and a ray-tracer can be used to predict the following, at a given user position with known satellite positions:

- Whether LOS signal is present or not
- Number of NLOS signals
- Delta path delay of each NLOS signal

The satellite positions can be computed *a priori* using ephemeris data. However, the predicted parameters are also dependent on user position which is unknown. The methodology for the 3DBM-assisted multipath parameter estimation (i.e., Section 3.1) assumes that *the true user position is known*, and Section 3.2.3 discusses how to handle the case where the true position is unknown.

The number of NLOS signals along with the presence or absence of the LOS signal collectively provides the number of signal paths. For this thesis, a maximum of three paths is considered; however, the methodology could be extended to any number of paths. The predicted number of paths and some corresponding signal parameters are used as *a priori* information for an estimator to estimate the unknown multipath signals' parameters, as described below.

3.1.1.2 Least Squares-based Estimation of Multipath Signal Parameters

For this research a LSQ estimator was used to estimate the unknown multipath parameters using correlator outputs as observations. The LSQ was provided with predicted signal parameters as *a priori* information in order to: (a) select the proper model for the correlators based on the number of predicted paths, and (b) to initialize the delta path delay states. This represents a key

difference compared to traditional LSQ-based multipath parameters estimation techniques (He and Petovello 2013, Van Nee 1992).

A detailed signal model in the presence and absence of NLOS signal(s), along with corresponding correlator output was presented in Sections 2.2 and 2.6. For convenience, the correlator (observation) models (i.e., $Z = S$) for a one-path, two-path and three-path signal from Equations 2.7 , 2.26, 2.27 are reproduced in Table 3.1 along with the corresponding unknown state vector (X) to be estimated in each case.

Table 3.1: Correlator model and corresponding states for different signal path

# Signal Paths	Correlator Model	States
1	$Z = A_1^2 R^2(\Delta\tau_1)$	$X = [A_1 \ \tau_1]^T$
2	$Z = A_1^2 R^2(\Delta\tau_1) + A_2^2 R^2(\Delta\tau_2) + 2A_1 A_2 R(\Delta\tau_1) R(\Delta\tau_2) \cos(\delta\theta_{12})$	$X = [A_1 \ \tau_1 \ A_2 \ \delta\tau_2 \ \delta\theta_{12}]^T$
3	$Z = A_1^2 R^2(\Delta\tau_1) + A_2^2 R^2(\Delta\tau_2) + A_3^2 R^2(\Delta\tau_3) + 2A_1 A_2 R(\Delta\tau_1) R(\Delta\tau_2) \cos(\delta\theta_{12}) + 2A_2 A_3 R(\Delta\tau_2) R(\Delta\tau_3) \cos(\delta\theta_{23}) + 2A_1 A_3 R(\Delta\tau_1) R(\Delta\tau_3) \cos(\delta\theta_{13})$	$X = [A_1 \ \tau_1 \ A_2 \ \delta\tau_2 \ A_3 \ \delta\tau_3 \ \delta\theta_{12} \ \delta\theta_{13}]^T$ and $\delta\theta_{23} = \delta\theta_{13} - \delta\theta_{12}$

The predicted number of signal paths is used to select which of these correlator models should be used in the LSQ estimator. It is noted that the *absolute* code phase of the shortest path is estimated, but for longer paths, only the delay *relative* to the shortest path is estimated, even if the shortest path is NLOS.

The autocorrelation function $R(\cdot)$, used in this research is based on the hyperbolic model proposed by Sharp (2009), taking into account the effect of front-end bandwidth. The accuracy of the hyperbolic correlator model was confirmed by comparing it to the correlator outputs obtained when using a Spirent hardware simulator as input. Comparing the correlators output against the model yielded correlation coefficient of approximately 0.99; which is considered to be more than good enough.

Since the observation model for the LSQ is highly non-linear, the initial estimate of states becomes an important factor for convergence towards the (hopefully) true values. With that in mind, the LSQ estimation was performed using several different initial values of the states (details below) and the state estimates corresponding to the minimum root-sum-of-squared (RSS) of residuals was selected as the final solution. In particular, the predicted delta path delay ($\delta\tau$) was used as the initial point of expansion and its uncertainty was determined from the quality of the 3DBM. In addition, since the delta phase and multipath-to-direct ratio (MDR) ($MDR_k = A_k/A_1$; $k>1$) information cannot be predicted from the 3DBM, these states were initialized with the following range of values:

- MDRs values: 0.1 to 0.9 with a step size of 0.2
- Delta phase ($\delta\theta$): -180° to 180° with a step size of 45°

- A_1 and τ_1 were initialized to the maximum correlator power and to the corresponding code phase value, respectively

Since the observation model is non-linear, the linearized LSQ estimate of the corrections to the state is given by equation (3.1)

$$\delta X = (H^T W^{-1} H + P_0^{-1})^{-1} (H^T W^{-1} \delta Z) \quad (3.1)$$

where terms are the same as in equation (2.14).

For this research, the element of P_0 corresponding to the delta path delay state was set based on the accuracy of the 3DBM; for all other states, the P_0 term was set to infinity (actually the terms of P_0^{-1} were set to zero). The equations for the observation matrix were derived for the one, two and three-path cases and are shown in Appendix A. The appendix also summarizes the form of the covariance matrix (W), which is available in the literature (Misra & Enge 2011, Van Diggelen 2009).

3.1.2 Validation of 3DBM-assisted Multipath Parameter Estimation Technique

The 3DBM-assisted multipath parameter estimation technique was validated using simulations and with real data collected in downtown Calgary. The primary reason for simulations was to prove the concept by having a control on the desired parameters, especially the delta phase due to high degree of non-linearity associated with this state. The validation of the method is performed by assessing the accuracy of the estimated delta path delay since, as described in Section 3.2, this is the key parameter used for computing a final position estimate.

3.1.2.1 Simulated Scenarios

For simulated data, MATLAB-based software was used to generate correlator grids based on the models defined in Table 3.1. The uncertainty associated with the available delta path delay was considered to be 3 m, which is the accuracy of the 3DBM used in this thesis. In case of no assistance (i.e., the default case), the LSQ measurement model was assumed to be the two-path model and the initial estimate of delta path delay was set to 60 m (Xie 2013). It is worth mentioning that for the simulated scenario presented here, the code phase delay of LOS signal was set to zero, hence NLOS delay (τ_k) and delta path delay ($\delta\tau$) were the same in this case (since $\tau_k = \tau_1 + \delta\tau$).

The different scenarios considered for analyzing the two-path case are shown in Table 3.2. For the three-path case, the MDR and delta phase of second NLOS signal were set be as same as that of first NLOS signal, and the delta path delay of the second NLOS signal was 0.1 chips (~ 30 m) longer than the first NLOS signal. Front-end bandwidths of 2 MHz, 5 MHz and 10 MHz were considered for the analysis, which together capture a wide spectrum of GNSS applications.

In order to add the effect of noise, each combination of parameters presented in Table 3.2 was run 100 times, each with a different simulated noise sequence; which resulted in a total of 21,000 different runs. The results and analysis were done using parameters of the GPS L1 C/A signal, however it is expected that key findings will translate to other GNSS signals as well. In order to see the effect of bandwidth loss on the accuracy of estimated parameters, the error statistics are provided separately for each of the three bandwidths considered (corresponding to 7,000 runs per bandwidth value).

Table 3.2: Different scenarios for two-path case

Parameters	Unit	Range	Step
MDR	N/A	0.1 to 0.5	0.1
Delta Path Delay	metre	15 to 90	15
Delta Phase	degree	0 to 180	30
Front-end Bandwidth	MHz	2, 5 and 10	N/A

The results presented in this section are based on two different scenarios. The first scenario is based on a true two-path signal. The second scenario is based on a true three-path signal. The RMS error of the estimated delta path delay for the two-path signal and three-path signal is presented in Figure 3.2 and Figure 3.3 respectively.

For the two-path case, using the assistance data yields an improvement of approximately 10% in the RMS delta path delay errors, as compared to the unassisted case. This was observed for all the three front-end bandwidths (2 MHz, 5 MHz and 10 MHz). Although the improvement with assistance was same for all the three front-end bandwidth case, the absolute errors were larger in case of 2 MHz front-end bandwidth as compared to other two front-ends; due to the practical limitation of smaller front-end bandwidth-based receivers to resolve path delays. Furthermore, although the accuracy improvement was minimal, 30% of the solutions (out of 21,000) were unavailable for the unassisted case because the LSQ estimator did not converge. As expected, significant improvement was observed in the case of the three-path signal since the default observation model in the unassisted case was a two-path model. These results suggest that providing assistance data from 3DBM improves the estimation performance of the LSQ.

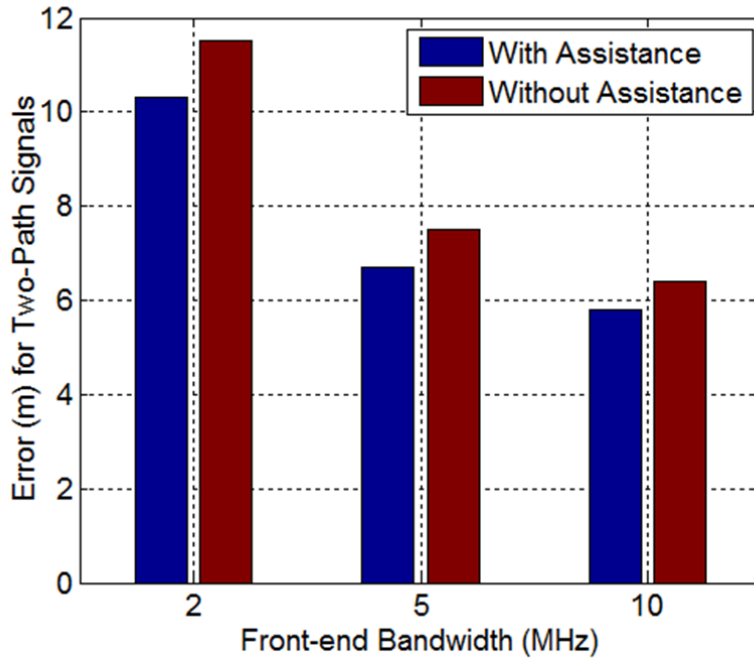


Figure 3.2: RMS error of delta path delay for two-path signal. Comparison is done in presence and absence of assistance from 3DBM.

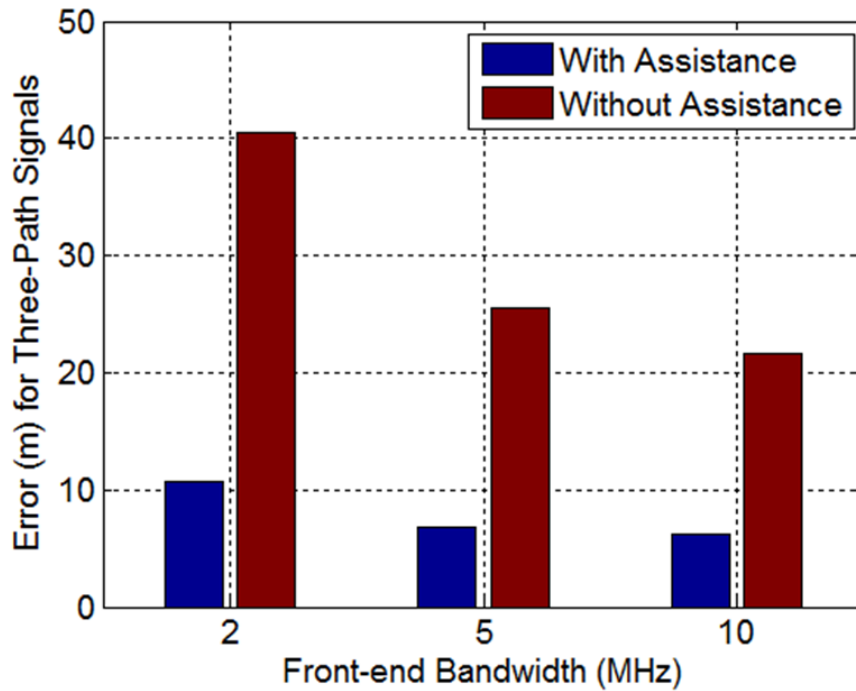


Figure 3.3: RMS error of delta path delay for three-path signal. Comparison is done in presence and absence of assistance from 3DBM related to delta path delay and its variance.

3.1.2.2 Results and Analysis for Data Collected in Downtown Calgary

To augment the analysis based on simulated data, the benefit of assistance data was validated using real data collected in downtown Calgary on 14th January 2014. The detailed description of the data collection and sky plot is presented in section 4.1.1. Before presenting the results, Figure 3.4 shows the block diagram depicting the generation of reference delta path delay for real data. First, the true delta path delay was generated using a reference position (accuracy of few decimeters; detail in section 4.1.1). Second, the delta path delay was estimated as described above using predicted signal parameters from the reference position. Finally, the difference between the estimated delta path delay and true delta path delay was declared as estimation error.

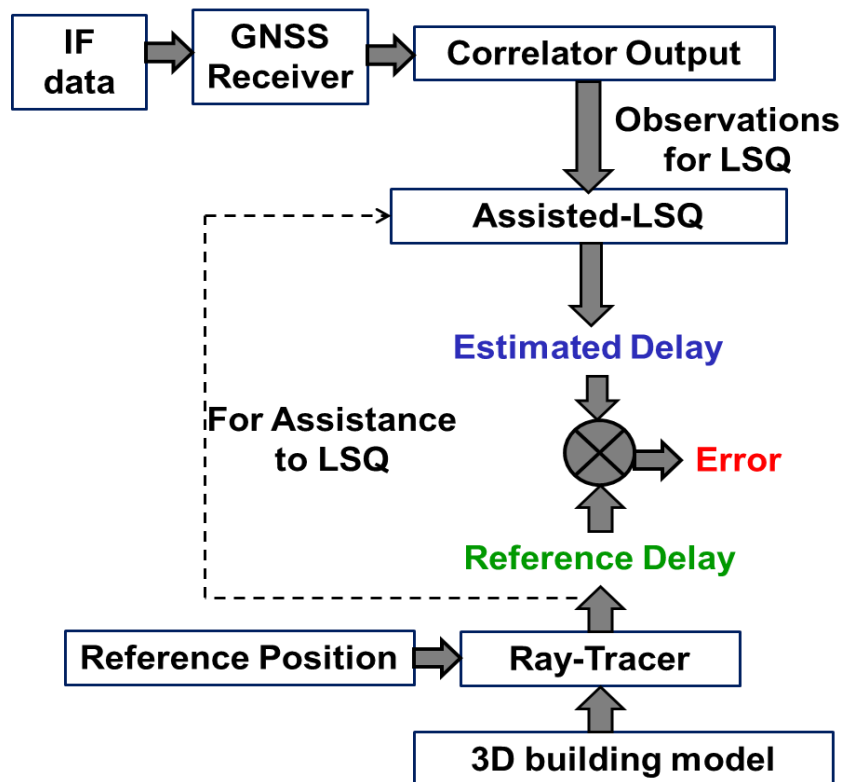


Figure 3.4: Generation of estimated and reference delta path delay (true delay) using real data.

The error statistics for four PRNs, PRN 31 (azimuth: 166°, elevation: 35°), PRN 32 (azimuth: 290°, elevation: 49°), PRN 11 (azimuth: 260°, elevation: 40°) and PRN 1 (azimuth: 300°, elevation: 40°) are presented in Table 3.3. Error statistics are presented for the case with and without assistance data from 3DBM.

Without assistance to LSQ a default case for number of paths and delta path delay (see Section 3.1.2.1) was used by LSQ to estimate the delay. By extension, in case of no assistance the error in estimated delay is expected to be large due to the fact that although there might be more than two-paths signals, the LSQ estimates delay based on default two-path case (Section 3.1.2.1); this can be corroborated by results presented in Table 3.3. Also shown in the table is the number of epochs where assistance was available.

Most importantly, an improvement of 54%, 53%, 32% and 23% in terms of RMS was observed for PRN 31, PRN 32, PRN 11 and PRN 1 respectively when using assistance. Furthermore, the benefit of assistance is more profound for PRNs with more epochs where assistance is available.

Table 3.3: Error statistics of delta path delay error for a downtown Calgary data

PRN	With assistance		Without assistance		Number of epochs where assistance was available
	Mean	Standard Deviation	Mean	Standard Deviation	Total Epochs : 110
PRN 31	9.3	6.2	21.1	12.7	101
PRN 32	13.1	7.1	25.1	19.4	93
PRN 11	15.8	9.8	24.5	12.4	61
PRN 1	17.5	15.4	26.5	14.3	40

To summarize, the LSQ-based estimator provides accurate delta path delay when using assistance data. In particular, since the mathematical model for the observation is highly non-linear, initializing the states with at least known delta path delay helps with the convergence of the LSQ algorithm.

The next section describes how the algorithm described above is used to enable the main contribution of this thesis: a positioning algorithm called 3DBM-assisted snapshot positioning algorithm.

3.2 3DBM-assisted Snapshot Positioning Algorithm

At a high level, the positioning algorithm is based on matching the *observed* GNSS signal parameters manifested in GNSS receiver correlators' output with *predicted* GNSS signal parameters obtained using 3DBM and a ray-tracing algorithm. The correlators are generated using a snapshot of GNSS data. A description of predicted signal parameters was provided in section 3.1.1.1, however, as depicted in Figure 3.5, the predicted parameters are highly dependent on receiver's position which is unknown.

To handle this, predictions are performed at several points called Candidate Points (CP) as explained in section 3.2.3. With this in mind, the basic premise of the algorithm is that the candidate point closest to true location would presumably be the *best match* between the predicted and observed parameters and will thus be declared as the final position estimate.

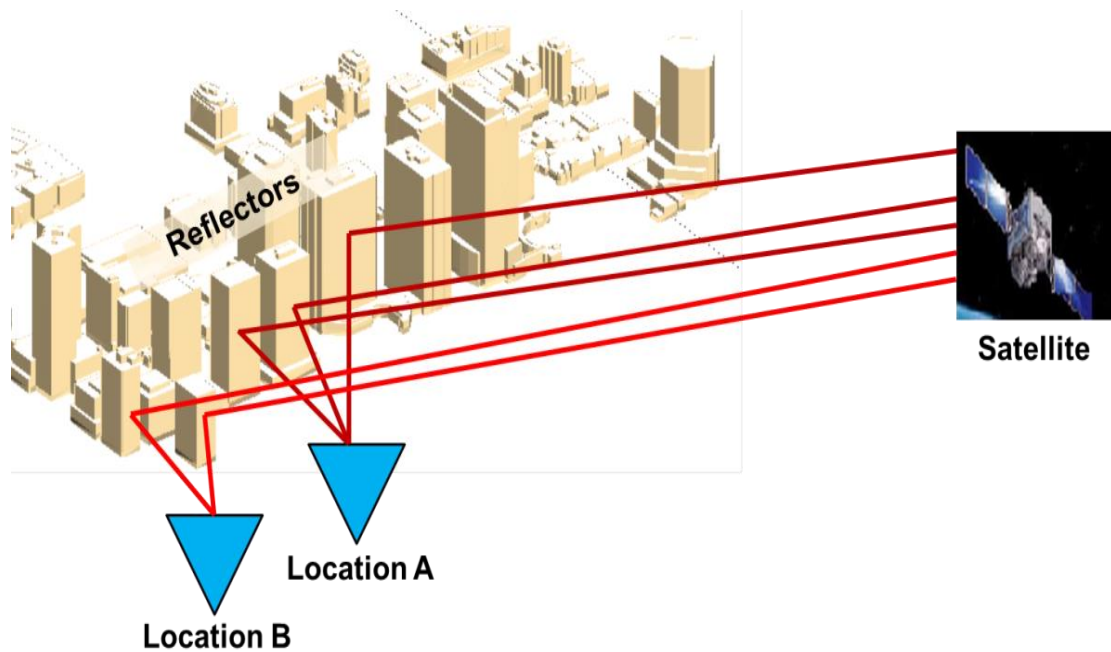


Figure 3.5: Different set of reflections at two nearby locations ‘A’ and ‘B’. Receiver at location A receives 3 reflections from 3 different reflectors; whereas the receiver receives 2 reflections from 2 totally different reflectors at location B, from the same satellite.

3.2.1 Overview of the Positioning Algorithm

The block diagram of the SDM algorithm is shown in Figure 3.6 and consists of the following steps:

1. Obtain an approximate initial position using any available positioning method (e.g., a standard GNSS receiver or WiFi).
2. Define a position grid (PG) around the initial position obtained in Step 1. Using the uncertainty of the initial position, the size of the PG is made large enough to contain the true position with sufficiently high probability. Each point in the PG is referred as a candidate point.

3. Use the 3DBM to compute predicted signal parameters at each CP, as described in Section 2.6.2. By varying the input position, different signal parameters are predicted which result in either better or worse matches with the received signal.
4. Obtain correlator outputs from a GNSS receiver using a snapshot of the IF samples. By definition, the correlator outputs contain the true signal parameters (including any LOS or NLOS signal) corresponding to the true location of the receiver and are thus referred to as observations, or “observed signal parameters”, in the following. This research only considers the correlator power (S , Table 3.1) but the algorithm is acquiescent to using in-phase and quadrature-phase correlator outputs (S_I and S_Q) separately. The implementation used for this research generates a grid (or block) of correlators spanning a range of code phase and Doppler values.
5. Match the predicted and observed signal parameters using a Signal Delay Matching (SDM) algorithm, which is based on the 3DBM-assisted multipath parameter estimation approach described in Section 3.1; further details are provided in section 3.2.4. Although a grid of correlators is generated, the peak correlator output is identified and only the correlators from the Doppler shift corresponding to the largest value in the correlator grid are extracted and used (i.e., correlators spaced in the time, or code phase, domain at a single frequency only are used). In other words, a block of correlators is not strictly required from the GNSS receiver if a sufficiently good estimate of the signal Doppler is available (e.g., from aiding sources).

Although not used in this work, the Doppler shift of the signal could conceivably be used to also estimate velocity, but this is left as future work. Details of obtaining observed and predicted

signal parameters and the signal delay matching algorithm is presented in the following sub-sections.

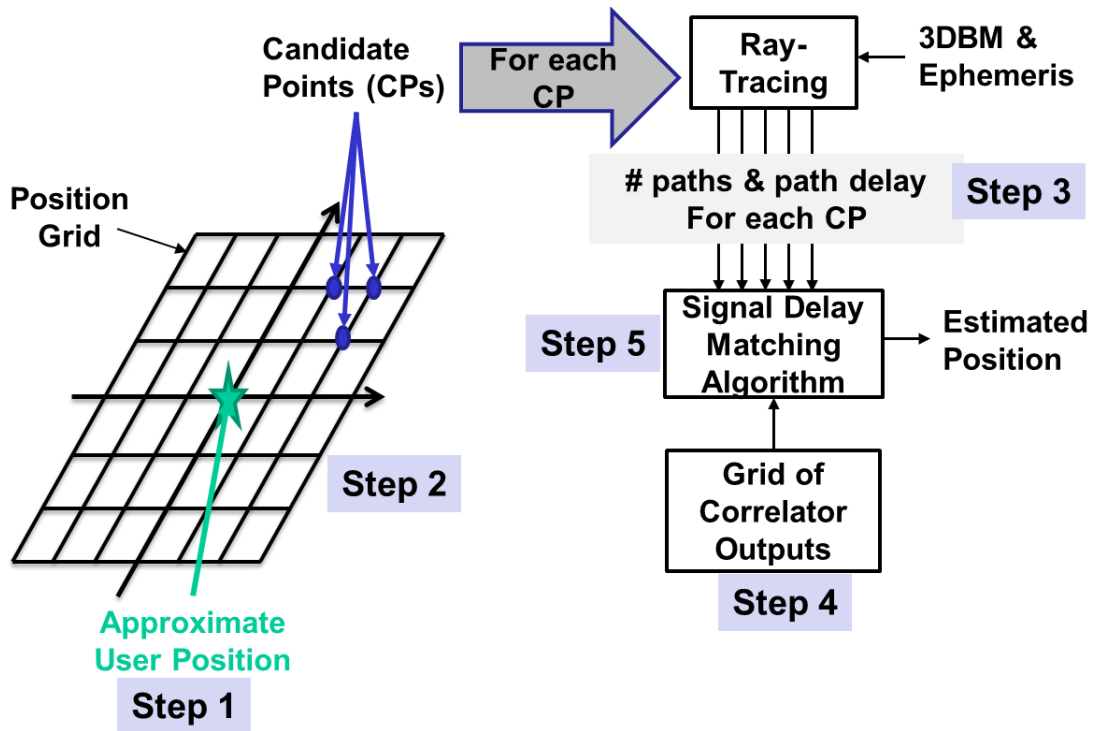


Figure 3.6: An architectural depiction of the proposed algorithm. Predicted signal parameters are generated for different candidate points and are *matched* with observed signal parameters, using a matching algorithm.

3.2.2 Generation of Observed Signal Parameters

The observed signal parameters are obtained from the receiver's correlator outputs. As indicated in Figure 3.7, the GNSS input samples are processed by the receiver and a grid of correlators is generated.

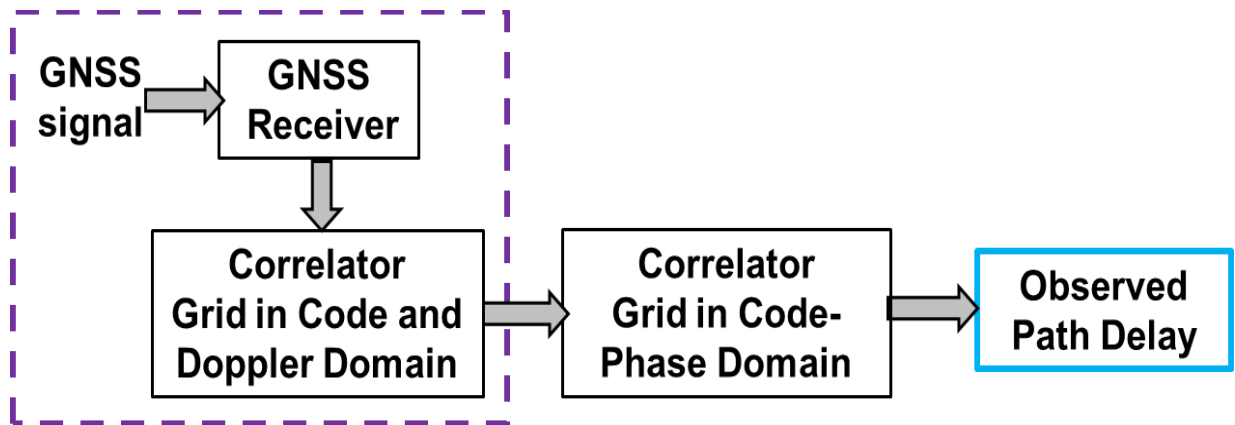


Figure 3.7: Generation of observed path delay. Dotted box shows a method for obtaining code phase correlators information, used in this research. Observed path delays are obtained from code phase domain correlators.

The correlator grid encompasses all the signals, i.e., LOS and NLOS signal(s) corresponding to each satellite in the Doppler and code phase domains. However, as mentioned above, all code phase domain correlators corresponding to the Doppler yielding maximum power was selected as “observed signal parameters”. More precisely all correlators in code domain corresponding to one particular Doppler is used as observations; by extension all the signals’ parameters are embedded inherently in the correlator grid including the path delay relative to the shortest path. An example is shown in Figure 3.8, where the entire correlator grid is shown along with the values that are used as observations to the LSQ estimators, denoted with a blue line projected onto the back plane of the plot.

Since the SDM algorithm is based on code phase delay, correlators in code phase domain are used for observed path delays. For this research a two-dimensional correlator grid in code phase and Doppler is obtained first; the correlator grid in code phase domain corresponding to largest value among all correlators is used for observed path delay.

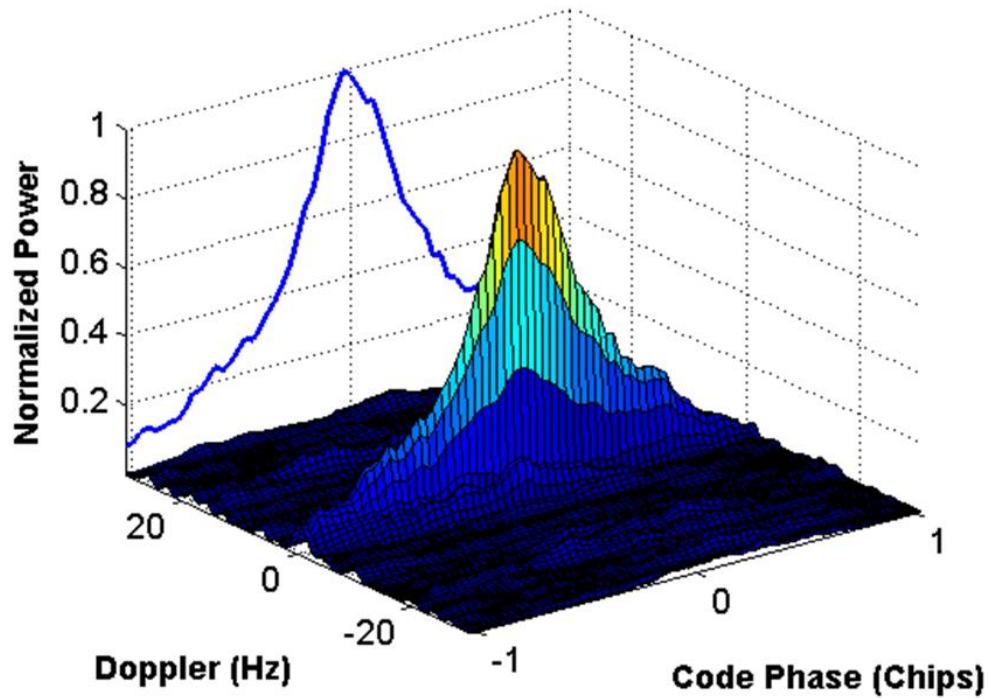


Figure 3.8: Example of correlator grid in the code phase and Doppler domains. Correlators in blue are those in code phase domain corresponding to the Doppler with the maximum power

3.2.3 Generation of Predicted Signal Parameters

Generation of the predicted signal parameters for different CPs is depicted in Figure 3.9. The predicted delta path delay was defined mathematically in equation 2.31. The delta path delay is predicted for each satellite at each CP along with the availability of the LOS signal. Once the observed and predicted signal information is obtained, the signal delay matching algorithm uses this information to provide estimated position, as described in the following section.

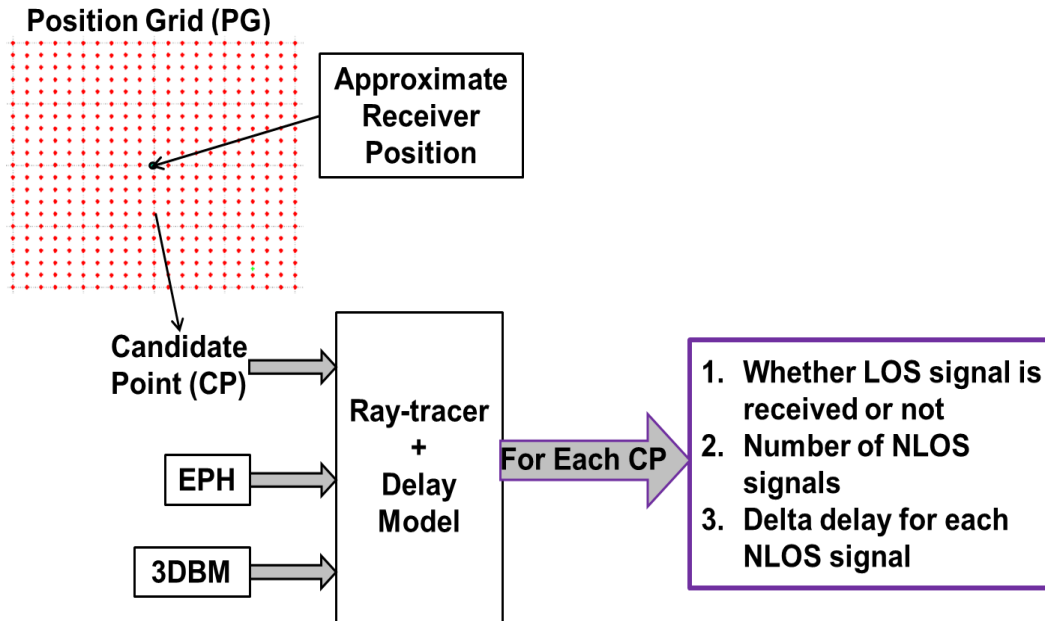


Figure 3.9: Block diagram depicting generation of predicted path delay.

3.2.4 SDM Algorithm

The objective of the SDM algorithm is to generate a metric for each CP based on the degree of matching between observed and predicted signal parameters. The CP with best metric is declared as final estimated position.

With this in mind, the SDM algorithm matches observed and predicted path delays by doing a LSQ fit as described in Section 3.1.2. Once this is done, the SDM metric is computed as explained in the following sub-section.

Before moving on, it is important to mention the importance of the *a priori* covariance matrix in the SDM algorithm. Without it the LSQ algorithm would theoretically converge to the same estimate for all CPs. In turn, the residuals for all CPs would be the same meaning the various CPs would be indistinguishable from each other in the context of the proposed positioning

algorithm. The *a priori* covariance effectively limits how much a path delay estimate can change from its predicted value, meaning that predicted path delays with larger errors will converge to a more erroneous final estimate, thus yielding larger residuals.

3.2.4.1 Compute the SDM Metric Using LSQ

Following the LSQ fit of the correlators to the selected mathematical model, the final step is to compute the RSS of residuals at each CP for each satellite. The RSS of residuals at each CP are then root-sum-summed across all satellites at a given epoch to yield an overall RSS of residual value. This overall RSS of residuals at each CP is used as the metric for final position estimation. More precisely, the CP with the smallest overall RSS is selected as the final position estimate.

Using the above approach, if the signal model is correctly parameterized at all CPs, the LSQ residuals will nominally be smallest for the CP closest to the true location and will increase for CPs further from the true location. However, since most CPs are not at the true position, the number of predicted signal paths will differ across CPs for a given satellite but the received signal contains a fixed number of signal paths. This means there will be instances where the LSQ model is either over- or under-parameterized relative to the true signal. The effect of these two cases is explained in the following sub-section.

3.2.4.2 Effect of Under- and Over-Parameterization Using Least-Squares

An under-parameterized model (i.e., predicting fewer signal paths than are actually received) will yield much larger residuals than a correctly-parameterized model, meaning selecting CPs with under-parameterized models as the final solution is very unlikely. In other words, no special steps are needed to handle this specific case.

In contrast, the over-parameterized model (i.e., predicting more signal paths than are actually received) will yield artificially small residuals because of the increased degrees of freedom in the model. Since incorrectly predicting the total number of signal-paths will only occur at incorrect CPs, this situation needs to be identified in order to avoid accidentally selecting these “incorrect CPs” as the final estimate.

Since an over-parameterized model should estimate a very small (ideally zero) amplitude for signal-paths that are not actually present in the observed data, a threshold for the MDR was used to identify over-parameterization. The MDR threshold was selected using the same simulations described in Section 3.1.2.1.

For each simulated correlator grid, LSQ estimates were obtained using all of the models in Table 3.1, thus including under-, over- and correctly-parameterized solutions. The cumulative distribution function (CDF) of the estimated MDR values is shown in Figure 3.10, where all over-, under- and correctly parameterized *MDR values* are grouped together. In this context, the following definitions are used:

- An “over-parameterized MDR” refers to MDR values corresponding to unnecessary states, that is, values of MDR_k for when k exceeds the true number of paths
- A “correctly-parameterized MDR” refers to all MDR estimates computed when the number of predicted paths matches the true number of paths
- An “under-parameterized MDR” refers to all MDR values when the number of predicted paths is less than the true number of paths

As shown in Figure 3.10, there is no overlap between the over-parameterized case compared to other two cases, meaning a threshold can be defined that clearly (i.e., without false alarms) identifies over-parameterized cases. It is noted that the results for the correctly-parameterized case appear discrete because, for the correct model, the estimated MPDR values match the input, which are discrete (see Table 3.2).

Based on these results, a MDR threshold of 0.09 was selected. If an over-parameterization is detected at a given CP (i.e., the MDR falls below the threshold) then that CP's RSS of residuals is set to ten times the largest RSS of residuals across the other CPs. This easily distinguishes the RSS values CPs with and without correctly-parameterized models.

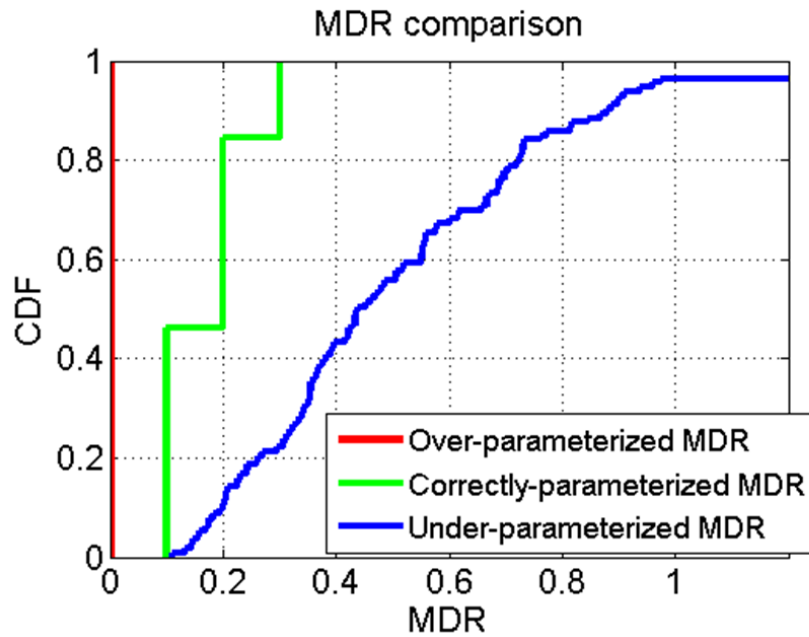


Figure 3.10: Cumulative distribution function (CDF) of estimated MDR values for over-parameterized, correctly-parameterized and under-parameterized cases.

3.3 Summary

This Chapter introduced a novel positioning algorithm using snapshots of GNSS data with the help of a 3DBM. The 3DBM was used to provide *a priori* information to the LSQ estimator to correctly select the mathematical model and to initialize the delta path delay, which resulted in accurate estimated parameters. The heart of the positioning algorithm is a SDM-based matching technique, which estimates position based on matching a set of predicted and observed signal parameters at several CPs inside a PG (defined around an approximate given user position). Including information presented in Chapter 2, the novel features of the proposed algorithm are:

- The proposed algorithm utilizes all NLOS signals from all satellites constructively
- The algorithm is based on using snapshot of GNSS data, not using tracking; by extension does the algorithm is resistant to problems like loop instability, loss of lock etc., which occurs frequently in urban environments
- The proposed algorithm is based on a novel SDM algorithm, matching observed and predicted delta path delay which is unaffected by traditional pseudorange-based method errors (such as atmospheric error, clock bias, tracking loop errors etc.). By extension the algorithm has the capability of providing a position solution using a single satellite only, in theory; however, the performance in that case would depend on several factors and is presented in detail in Chapter 4
- The proposed algorithm is based on using all correlator information corresponding to all NLOS signals and LOS signals, as input; the method avoids the loss of information resulting from reducing all correlator data into a single pseudorange (or code phase) measurement (He and Petovello 2014)

Chapter Four: **Results and Analysis**

This chapter provides results and analyses of the *3D Building Model-assisted Snapshot GNSS Positioning* algorithm presented in the previous chapter. Positioning performance is based on positioning accuracy and associated uncertainty bounds. Results of the algorithm are compared with a high-sensitivity software receiver and with a mass-market commercial receiver, in two different regions of downtown Calgary using two different front-ends.

The chapter first describes the data collection and data processing followed by the performance analysis of the proposed positioning algorithm. It concludes with an investigation of how to quantify the uncertainty in the estimated position.

4.1 Data Collection

In order to test and analyze performance of the proposed algorithm, two different data sets were collected in downtown Calgary on 14th January 2014 (Data Set 1) and 23rd December 2015 (Data Set 2). The data sets used different front-end bandwidths of 20 MHz and 4 MHz respectively, and were collected in two different regions of downtown Calgary. Details of each test are provided in the following sub-sections.

4.1.1 Data Set 1

This data set was collected using a front-end bandwidth of 20 MHz, on 14th January 2014 in downtown Calgary. The corresponding sky plot showing the distribution of satellites is shown in Figure 4.1. The data collection setup consisted of a NovAtel SPAN-LCI reference system, a National Instruments (NI) front-end for IF GNSS data sample collection, a NovAtel antenna and a base station receiver. The IF data was collected using the NI front-end with a stable Oven

Controlled Crystal Oscillator (OCXO). The IF samples were collected at a complex sampling rate of 20 mega samples per second.

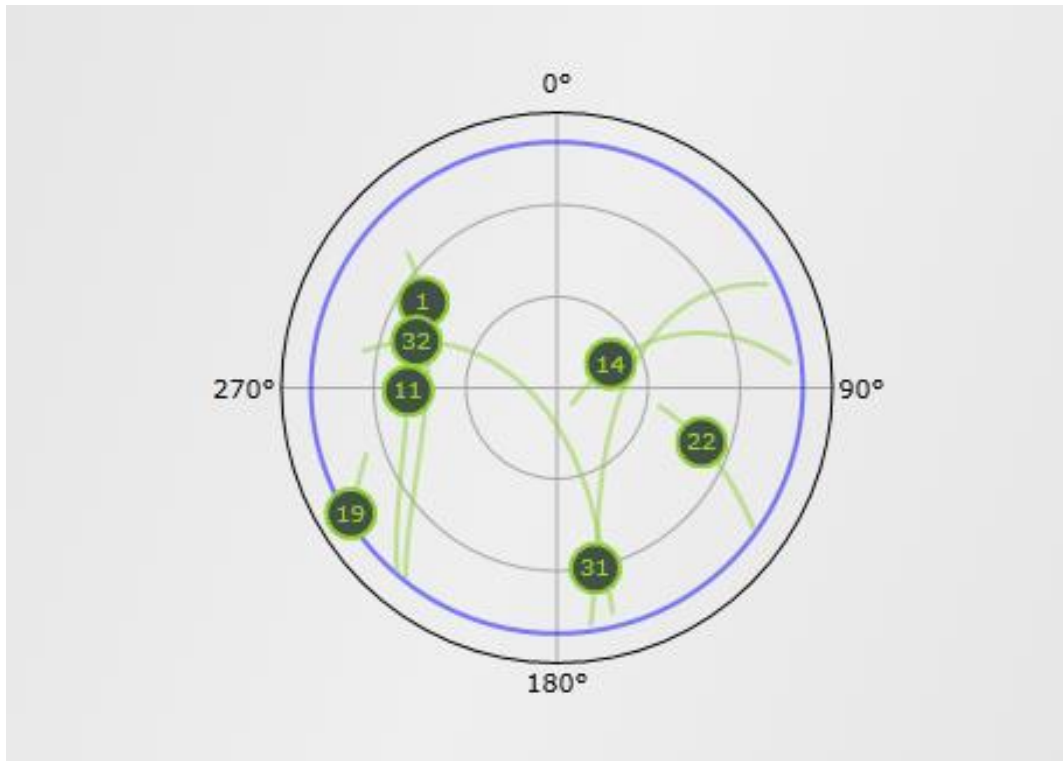


Figure 4.1: Sky plot for Data Set 1; circles represent the satellite positions at the middle of data collection

All of the mobile equipment were mounted on a test van. The base station was set up in the Position, Location And Navigation (PLAN) lab in the Calgary Centre for Innovative Technology (CCIT) building at the University of Calgary.

A differential GNSS/INS reference trajectory (typically accurate to few decimeters but with a worst case uncertainty of about 1 m) was obtained from NovAtel Inertial Explorer™ software using a tightly coupled forward and backward smoothing configuration and is depicted by the

magenta colored line in Figure 4.2. Positions were also logged from a u-blox-6 receiver for performance comparison.

In total, the trajectory lasted approximately 15 minutes and spanned approximately 3.5 km of road. The maximum speed during the test was about 15 m/s.

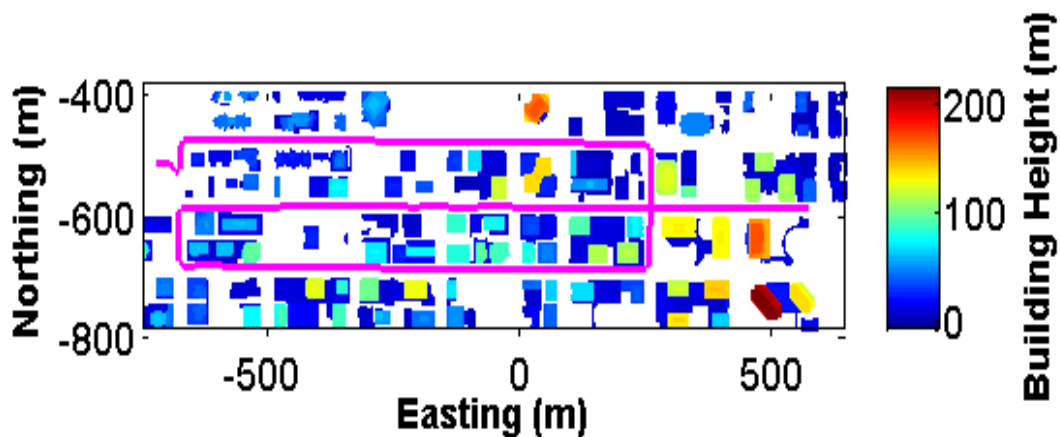


Figure 4.2: Trajectory for Data Set 1 collected in downtown Calgary. Figure shows the trajectory along with the building heights throughout the trajectory. Buildings surrounding the trajectory were as high as 200 metres.

The data was collected in downtown Calgary where buildings as high as 200 m are present (building heights are also shown in Figure 4.2). Figure 4.3 shows the “sky-visibility” along the trajectory, that is, the percentage of sky visible above zero degrees elevation as computed from the 3DBM at the reference positions. As can be seen, the sky-visibility is as low as 15 % and thus positioning using traditional GPS receiver is expected to have significantly degraded performance, which is confirmed later in this chapter.

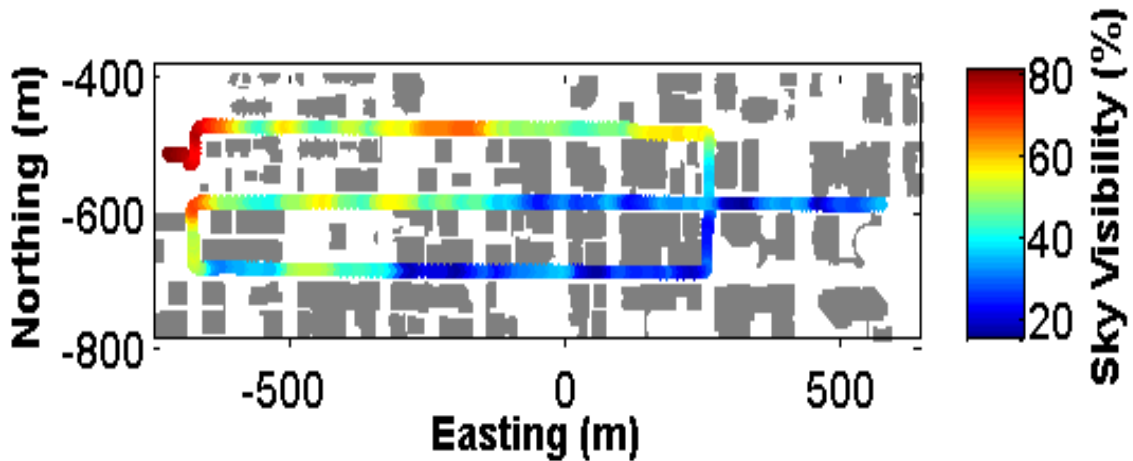


Figure 4.3: Sky-visibility throughout the trajectory for Data Set 1 collected in downtown Calgary. As depicted the sky-visibility is as low as less than 20 %, indicating deep urban scenarios

4.1.2 Data Set 2

This data was collected on 23rd December 2015 in downtown Calgary and the sky plot is shown in Figure 4.5. The data collection setup was same as described for Data Set 1, except a Leapfrog front-end (Morrison 2010) was used instead of a NI front-end. The Leapfrog front-end was developed in-house and has a bandwidth of 4 MHz and a sampling rate of 10 Msps. The reference trajectory was obtained in a similar way as for Data Set 1 (with similar accuracy) and is shown in Figure 4.5.

The top plot in Figure 4.5 shows the trajectory along which the data was collected along with the building heights. The bottom plot of Figure 4.5 depicts the sky-visibility along the trajectory.

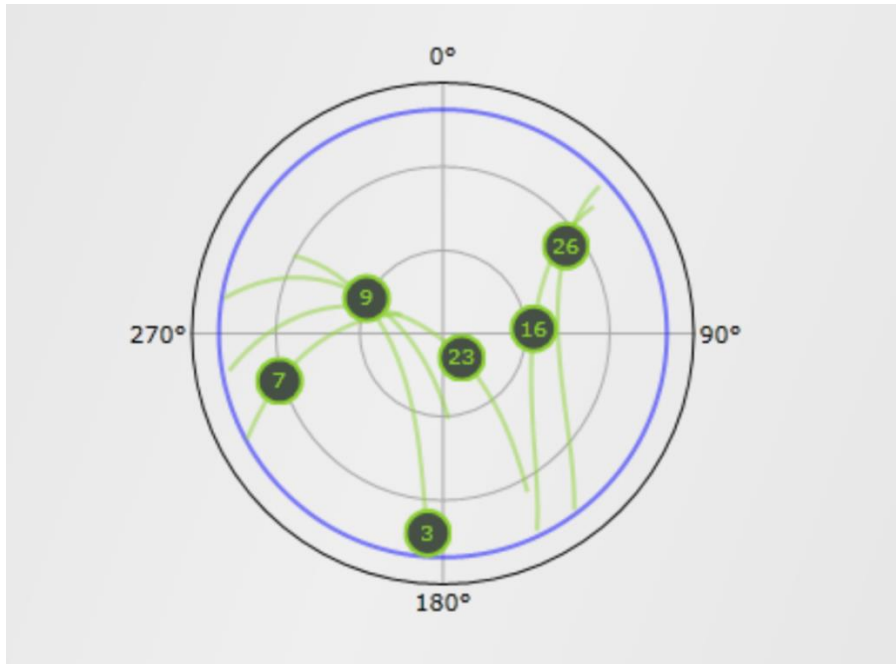


Figure 4.4: Sky plot for Data Set 2 during middle of data collection

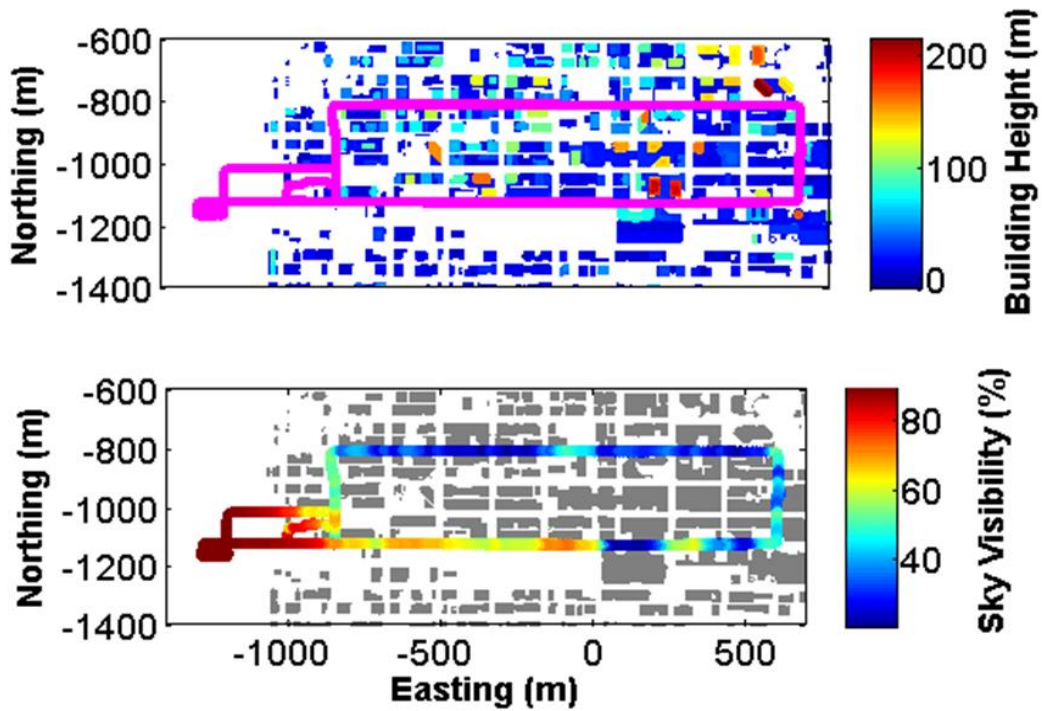


Figure 4.5: Downtown Calgary data collection trajectory for Data Set 2. Top figure shows the trajectory along with the building heights and the bottom figure shows the percentage sky-visibility at each location throughout the trajectory

This data set lasted 18 minutes and covered approximately 3.5 km of road. The maximum speed was 15 m/s.

4.2 Data Processing

This section describes: how the IF data was processed to generate correlator outputs; the software used for predicting signal parameters using a ray-tracer and 3DBM; and the software developed for implementing the SDM positioning algorithm.

4.2.1 IF Data Processing

The IF data was processed to generate a grid of correlator outputs that serve as inputs/observations to the SDM algorithm, as discussed in Chapter 3. GSNRx™, a software receiver developed at the University of Calgary (Petovello et al 2009) was used to process the IF data to generate the correlators output. The version of GSNRx™ used was based on a block processing strategy and provides a convenient user interface to define the two dimensional (code phase domain and Doppler domain) correlator grid via an option file. The parameter configuration used for block processing is summarized in Table 4.1. As shown, the correlator spacing in Doppler and code phase domain was 50 Hz and 10 m respectively, whereas the search space in Doppler and code phase domain was set as ± 150 Hz and ± 300 m. The coherent integration time was set to be 10 ms meaning external data bit aiding was not required, although the data was still aligned to the data bit boundaries—in a practical implementation, two 10-ms integrations could be performed (per satellite) and the one yielding the largest power would be selected to avoid integrating over data bit boundaries.

It is also noted that the GSNRx™ software was able to extract the true transmit time from the satellite signals, meaning there is no coarse-time error. This was done initially to focus on development of the SDM algorithm, but Section 5.4 addresses the case where the coarse-time error is present.

Table 4.1: Summary of processing parameters for generating observed signal parameters

Parameter	Value
Doppler search space	± 150 Hz in steps of 50 Hz
Code phase search space	± 300 m in steps of 10 m
Coherent integration time	10 ms

As mentioned in chapter 3, the positioning algorithm does not require two dimensional correlators, rather it requires code phase-domain correlators only. As such, the code phase-domain correlators corresponding to Doppler yielding the maximum correlator power were extracted as used as measurements for the SDM algorithm (positioning algorithm) described in section 4.2.3.

4.2.2 Predicting Signal Parameters

Predicted signal parameters were generated using a 3DBM and a ray-tracer as explained in Chapter 2. The 3DBM, purchased from 3DCAD browser (www.3dcadbrowser.com), consisted of faces in the form of triangles. The model has a quoted accuracy of 3 m and contains 400,668 triangles and 362,951 vertices. The complete model is shown in Figure 4.6.

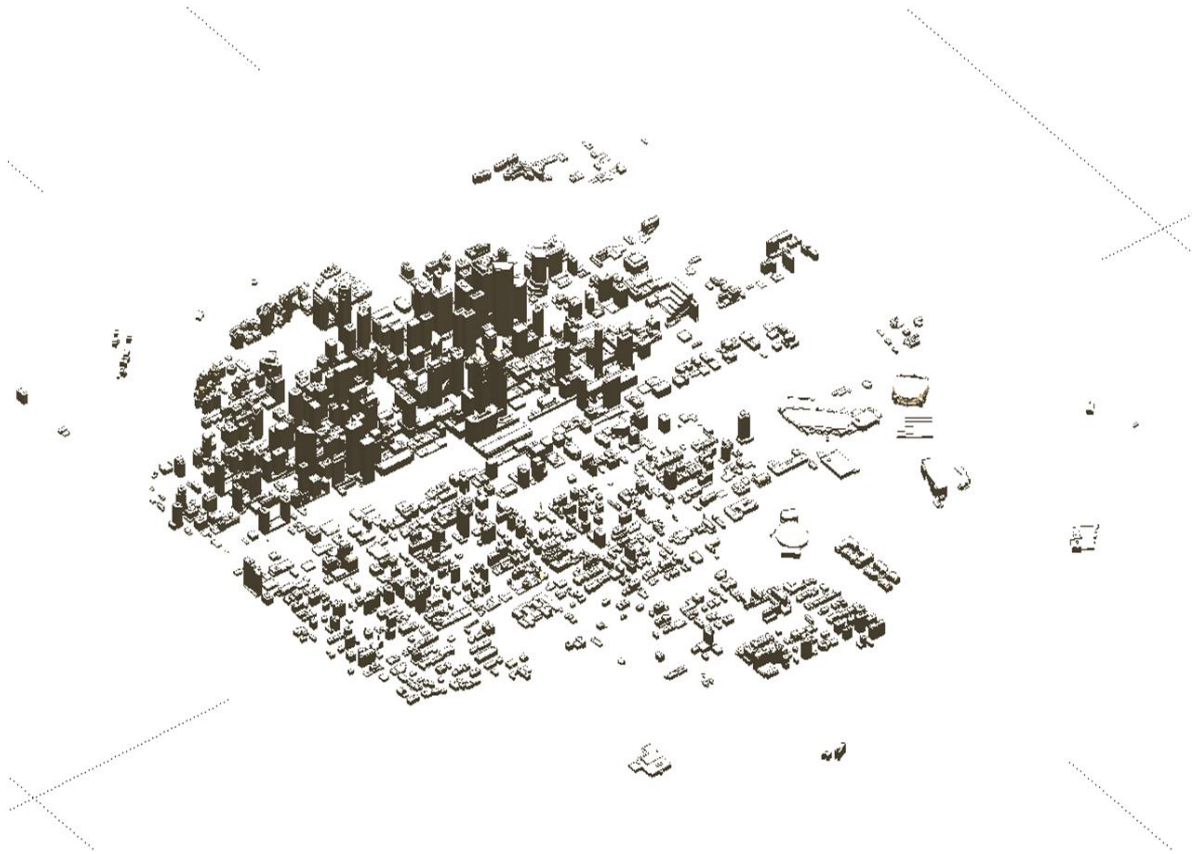


Figure 4.6: Processed 3DBM purchased from 3DCAD browser.

The first step for predicting signal parameters was to pre-process the 3DBM to obtain the coordinates of the buildings in a convenient coordinate frame. This pre-processing was performed once and the output was used for all subsequent data processing. The pre-processing of 3DBM is depicted in Figure 4.7 and consisted of converting the UTM (Universal Transverse Mercator) mapping-plane coordinates provided by the model to corresponding Cartesian coordinates in an Earth-Centred, Earth-Fixed (ECEF) frame.

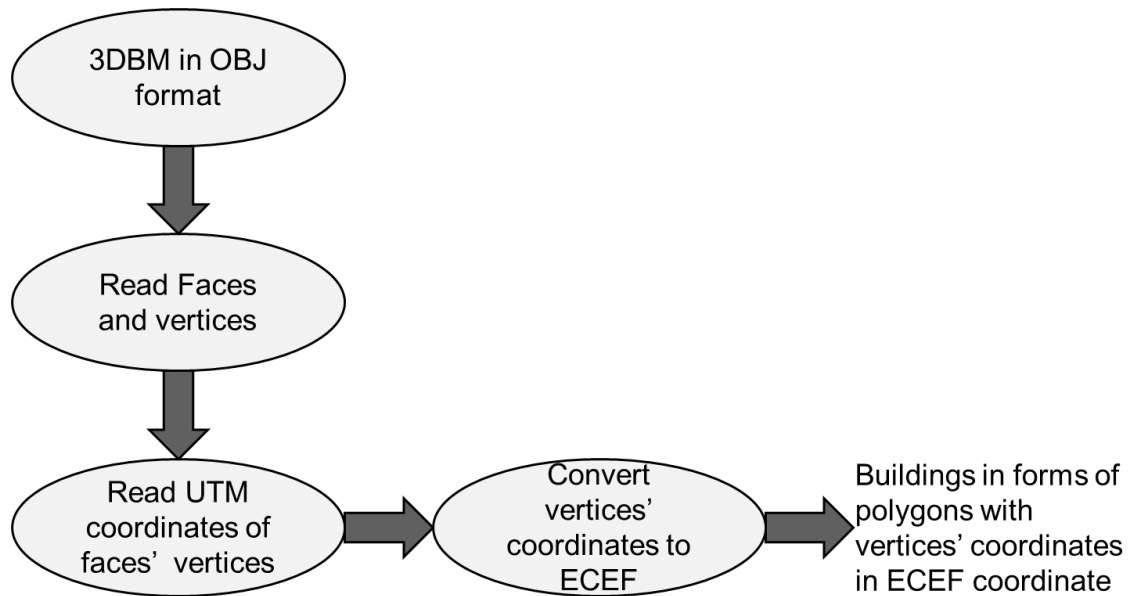


Figure 4.7: Block diagram of 3DBM processing.

A ray-tracer, implemented in MATLAB using the ray-triangle intersection model described in Chapter 2 was used to generate the predicted signal parameters. For this research only single-bounce reflections are considered (i.e., double- or triple-bounce reflections (or more) are not considered) which may limit the number and quality of matches with the observed data.

4.2.3 Positioning Algorithm (SDM Algorithm)

The positioning algorithm was developed in MATLAB, which accepts the correlator outputs from the IF data processing and predicted signal parameters as inputs. As mentioned in chapter 3, the size of the PG depends should be adjusted based on the uncertainty associated with the initial user position, with larger PGs for larger uncertainties. It is evident that a larger grid size would involve more CPs compared to a smaller PG and would thus require more processing.

For results presented in this chapter a position grid of 30 m (± 15 m) was considered to reduce the processing requirements and the approximate/estimated user position was replaced with the “true” position from the reference trajectory. The inherent assumption with this approach is that if the receiver’s estimated position were used with a larger PG (to accommodate the corresponding uncertainty in the estimate), the selected position would be the same as with a smaller PG. This assumption has been confirmed as discussed in Chapter 5 and hence the results presented below are also indicative of what is possible without a reference solution.

Finally, to be truly indicative of snapshot-based positioning algorithms, the results presented below do not include any filtering in the position-domain (e.g., Kalman filtering). By extension, filtering of the results should improve the overall performance, although this was not evaluated as part of this work.

4.2.4 Performance of the Algorithm in Terms of Processing Time

After presenting the data processing procedure for generating observed signal parameter (using IF data processing), predicted signal parameters and SDM data processing, this section presents the processing requirements in terms of processing time. Before presenting the detailed timing requirement it is emphasized here that the software written for this thesis is merely to prove the concept and to show its performance in terms of positioning accuracy. An efficient version of this software for real time application is left as a future work.

The processing time for the positioning algorithm was computed for different sections of algorithm and is summarized in Table 4.2. These times correspond to the ray-tracer and the positioning algorithm written in MATLAB, none of which was optimized for speed.

Table 4.2: Time required for overall processing for position estimate at one epoch using a laptop with i7 2.4 GHz processor and 6 GB memory

Amount of Processing	IF Data Processing	Predicting Signal Parameters (Ray-tracer)	SDM Processing	Total Time
Per CP for all PRNs	<< 1 s	1.2 s	< 0.5 s	≈ 28 minutes
For PG of 30 m; CP spacing 1 m 961 CPs (=31x31 CPs)		1.2 s x 961 CPs ≈ 20 minutes	0.5 x 961 s ≈ 500 s	

It is evident from Table 4.2 that the entire software takes more than 20 minutes to compute the position; mostly limited by the ray-tracing component of the algorithm. However, as shown in Ahmad et al (2004) and Oktal (2015), an optimized ray-tracer can take less than a second to provide all necessary information. By extension, the proposed algorithm may be able to be used in real-time application if an efficient ray-tracing algorithm and SDM algorithm was developed. The improvement of the proposed algorithm in terms of processing time is left as future work and some possible ways to improve the processing speed is discussed in Chapter 6.

4.3 Experimental Results and Analysis

This section presents and analyzes the results in several stages. First, an in-depth analysis from two separate data points is presented in order to emphasize key findings. Next, results from each of the data sets are presented and analyzed separately in order to highlight the effect of front-end bandwidth on the performance and to check the consistency of the performance. Finally, cumulative results from both data sets are presented.

However, before presenting and analyzing the results in detail, a short discussion of the algorithm's expected performance will be helpful. Since the predicted delays vary most quickly in the direction perpendicular to a reflector (equation 2.31), it follows that the (dis)agreement between the predicted and observed signals (as reflected in the LSQ residuals) will vary most quickly in this direction as well. In other words, the algorithm is expected to be more sensitive in this direction. Extending this logic to urban canyons, since reflectors (buildings) are typically parallel to the direction of travel and on either side of the user, the algorithm is expected to be most sensitive (i.e., give the best results) in the across-track direction.

4.3.1 In-Depth Analysis of Two Points

The analysis begins with an in-depth analysis for only two points from Data Set 1 ("point 1" and "point 2") in order to highlight key findings. The two selected points have sky visibilities of 20% and 60%. Figure 4.8 shows the surrounding buildings and idealized sky view (including building obstructions) for each point; point 2 has buildings (potential reflectors) only on one side as opposed to point 1, where buildings (potential reflectors) are on both sides of the road. The results from each point are summarized in the following sub-sections.

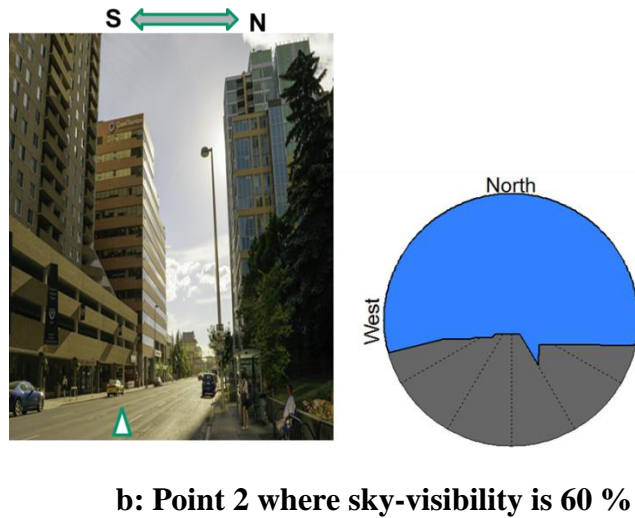
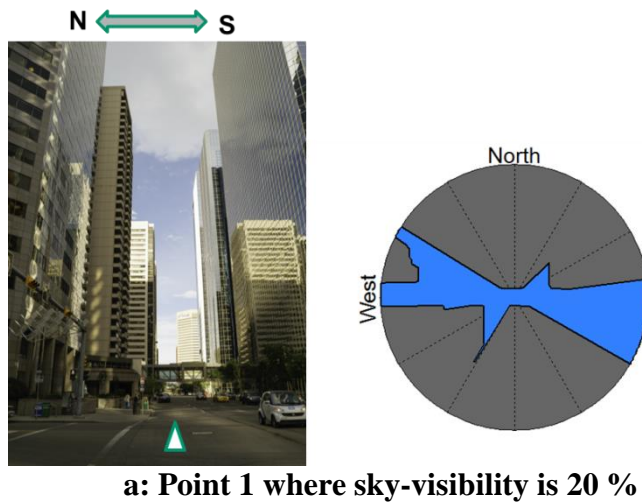


Figure 4.8: Two different points considered for detailed analysis; upper figure (a) shows the surrounding environment with the approximate user location represented as a white triangle for Point 1 and the lower figure is for Point 2. The skyplots shown as sky (blue) and buildings (grey) are computed from the 3DBM

4.3.1.1 Point 1 (20% Sky-Visibility)

Figure 4.9 shows the RSS of residuals at each CP for different PRNs for Point 1. Before discussing the results, the following points are made since they apply to all similar plots in this thesis:

- Since the reference position defines the centre of the grid, the east and north values can also be interpreted as errors
- RSS values are normalized to the range of (0,1] to simplify plotting

The first thing to notice is that the RSS values are nearly binary in nature (PRN 31 is an exception and is discussed below). Higher RSS values (red) correspond to under- and over-parameterized CPs; lower RSS values (blue) correspond to correctly-parametrized CPs. Although not distinguishable at this scale, there are small variations within in the blue regions.

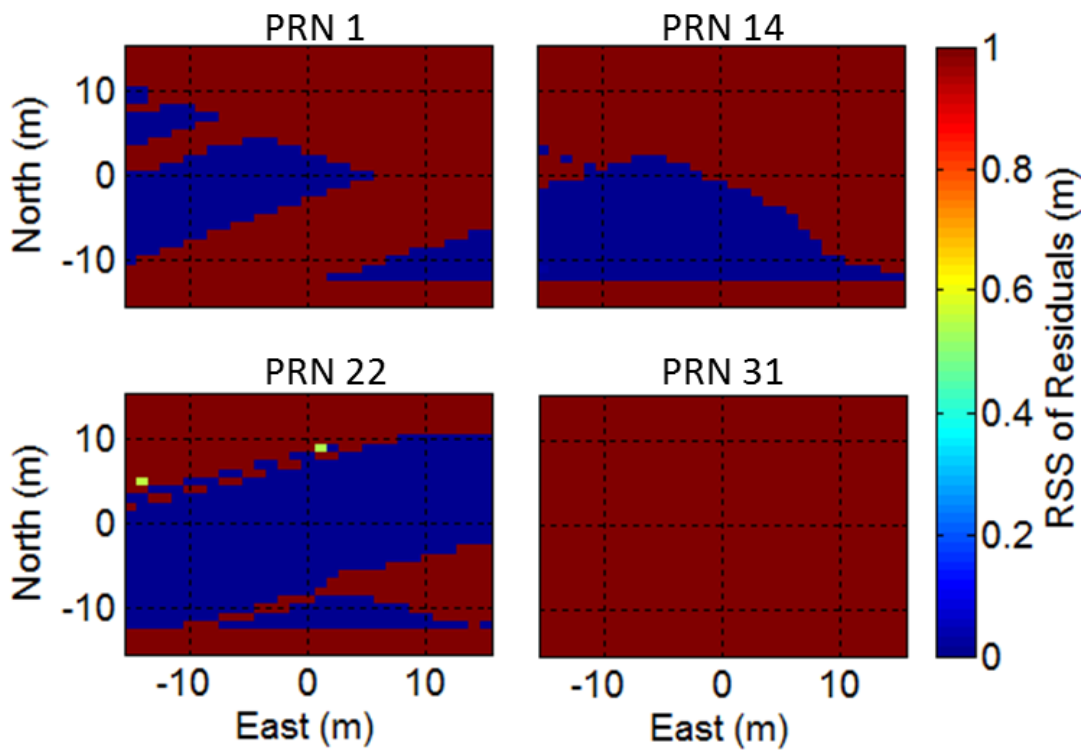


Figure 4.9: RSS of residuals for different PRNs at Point 1

The next thing to notice is that the “shape” of the RSS plots differs between satellites because of the different locations of the satellites relative to the user and surrounding buildings (reflectors). The left half of the plot for PRN 1 is a good example of this: each of the three blue regions corresponds to an area where the predicted signal reflects off of a different building. The other PRNs have different patterns because their predicted signals involve different buildings. The exception to this is PRN 31, which is predicted to have a single-path at all CPs. The single-path model does not receive any *a priori* information (i.e., no predicted relative path delays), so the LSQ estimate is completely unconstrained and converges to the same solution at all CPs; hence there are no variations in the RSS values (and the normalized RSS value will be unity). In other words, the proposed algorithm only makes use of reflected signals and does not use LOS signals at all (including LOS data, which is left as future work). With this in mind, PRN 11 was also a single-path satellite and is thus not shown. It is also noted that a position estimate can be obtained using only a single satellite with multiple paths; for the results shown, using either PRN 1, PRN 14 or PRN 22 only yields position errors of 4.5 m, 9.8 m and 5.4 m respectively.

Figure 4.10 shows the overall RSS across all satellites at each CP and the final position estimate is indicated with a white star. The PG is centered on true location, that is, the estimated position location will be the corresponding error. In this case, despite only using information from three satellites, the position estimate has an error of 3.6 m; about 1 m across-track and 3 m along-track (the vehicle was moving east/west). This contrasts with traditional GNSS methods where the across-track error in urban canyons is typically larger than the along-track error due to poor across-track satellite geometry/visibility (Groves 2011, Ward et al. 2006) but is consistent with the expected performance. The final point is that the blue area containing the smallest RSS

values spans a relatively small region, about 2-3 m in each horizontal direction. This suggests that the solution is fairly strong in both the along- and across-track directions. Quantifying the solution uncertainty is discussed later in this chapter in section 4.4.

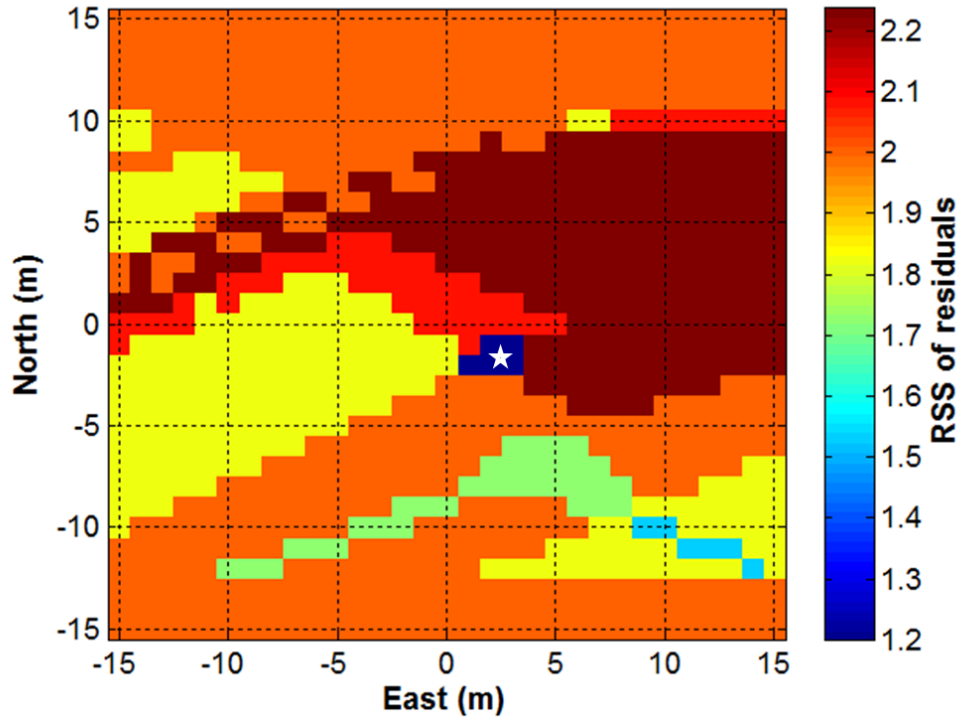


Figure 4.10: Overall RSS of residuals from all PRNs and final estimated position (white star) at the Point 1

4.3.1.2 Point 2 (60% Sky-Visibility)

The RSS of residuals for three different PRNs and the overall RSS at Point 2 is shown in Figure 4.11 and Figure 4.12 respectively. In addition to the satellites shown in Figure 4.11, PRNs 11 and PRN 22 were single-path satellites and thus not shown. Comparing these results with those of Point 1, it is obvious that RSS patterns are quite different and that they are more widely spread in the east/west direction (direction of travel). The reason for this is that there are fewer buildings

(reflectors) that come into play at this location, and the buildings are located on only one side of the road.

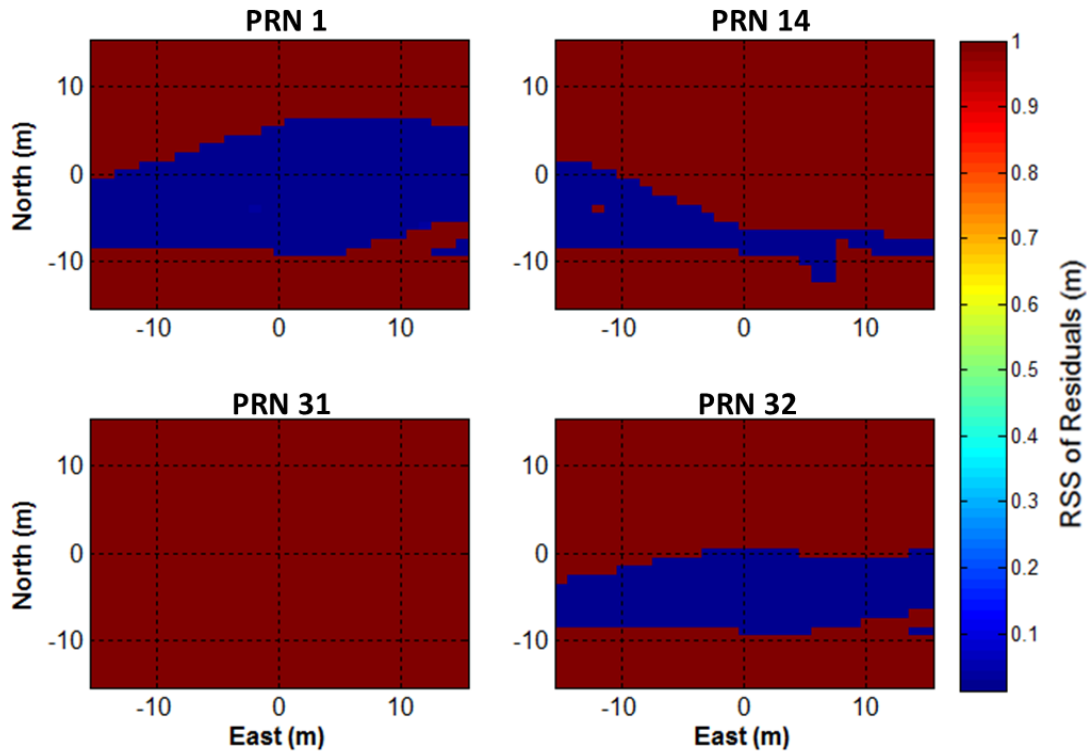


Figure 4.11: RSS of residuals from PRN 1, 14 and 32 at Point 2

This means that CPs in the along-track direction predict similar path delays and hence the variability of the residuals is much smaller. It is therefore not surprising that the position error (8.4 m) is larger than at Point 1 (3.6 m). This increased uncertainty is indirectly shown in Figure 4.12 where the area with the smallest RSS value is much more spread in the along-track direction.

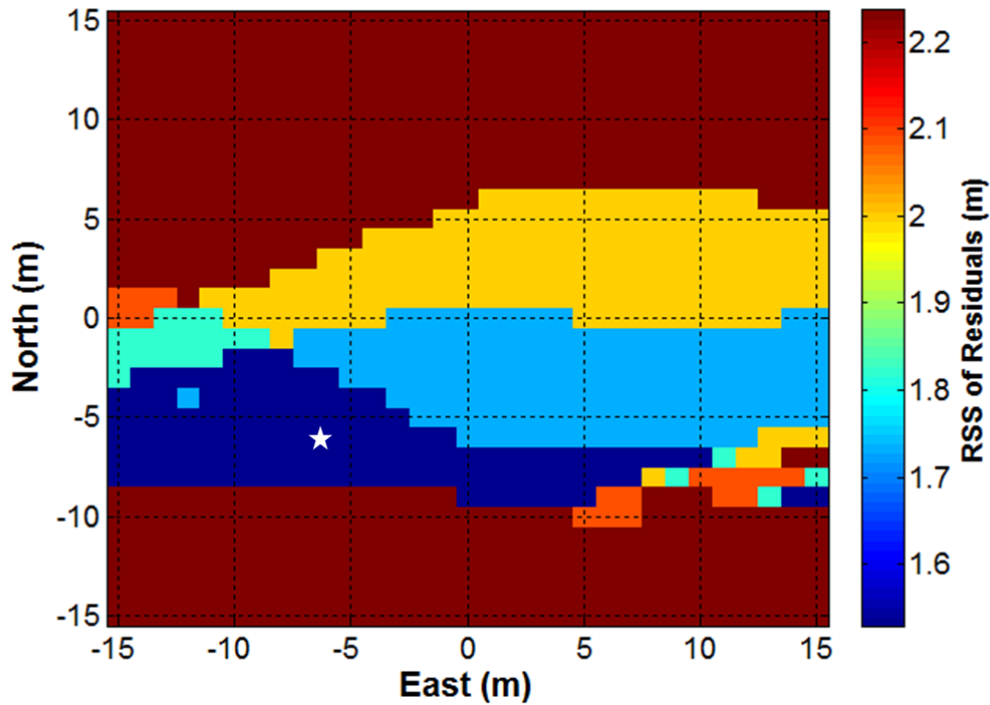


Figure 4.12: Overall RSS of residuals from all PRNs and final estimated position (white star) at the Point 2

4.3.2 Analysis of Data Set 1

This section expands the analysis to include the entire trajectory of Data Set 1. In particular, since the analysis of Point 1 and Point 2 in Section 4.3.1, indicates the possibility of relationship of the position error with sky-visibility. In order to verify this, Figure 4.13 shows the horizontal position error with respect to sky-visibility for all points in the data set. Results from two traditional pseudorange-based receivers also are shown for comparison: one is a high-sensitivity version of the GSNRx™ software receiver and the other is the u-blox 6 receiver mentioned in Section 4.3.3.

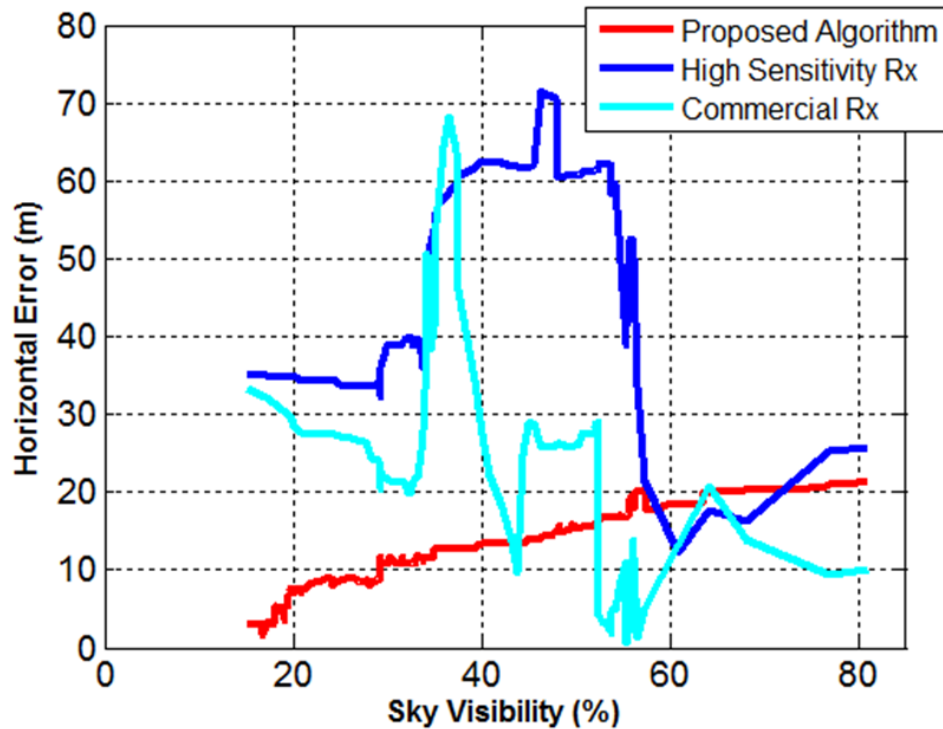


Figure 4.13: Horizontal error with respect to sky-visibility for the proposed algorithm and two pseudorange-based high-sensitivity receivers.

Results in Figure 4.13 indicate the following about the performance of the proposed algorithm:

- The proposed algorithm has a clear relationship of error with respect to sky-visibility , with the lowest sky visibilities providing the best performance
- As the sky-visibility increases the performance of the proposed algorithm degrades, which is primarily due to lesser number of PRNs contributing to the position estimate (i.e., the number of satellites with at least two signal paths)
- The proposed method provides better results compared to other traditional methods, in most cases despite using a snapshot-based approach (thus offering power savings)

and no filtering. By extension, filtering the results from the proposed solution would likely yield even better performance.

In contrast to above results, the two pseudorange-based receivers contain large biases for sky visibilities ranging from about 30-50% and their performance improves as the sky-visibility improves. This is an expected performance of a pseudorange-based positioning algorithm in urban environment (Xie and Petovello 2015; Groves 2011; Bradbury et al 2007).

Since the proposed algorithm is based on using delta path delay, it is unaffected by traditional pseudorange-based error sources such as clock bias, atmospheric errors etc. Since these errors affect all signal paths equally, the delta path delay is unaffected. This further supports the better results of the proposed algorithm compared to the two pseudorange-based approaches.

Also shown in Figure 4.13 is that there is a cross-over point with sky-visibility of approximately 50%, where the pseudorange-based positioning algorithm starts performing better (in terms of error) compared to the proposed algorithm. This deterioration in the positioning performance of the proposed algorithm is due to not including LOS signals in the SDM algorithm. This further suggests that there is a room for improvement in the performance of the proposed algorithm. This is discussed in detail in chapter 6, as future work.

After obtaining an interesting relationship of error versus sky-visibility for the proposed algorithm, the error statistics for all the three solutions is summarized in Table 4.3 and the corresponding improvement of the proposed method's RMS errors is shown in Table 4.4. In addition to the overall horizontal error, the errors in the along and across-track directions are shown; these were obtained by rotating the north and east errors along the direction of travel

using the reference solution’s azimuth. Overall, error statistics of the proposed algorithm are best amongst all solutions. Results in Table 4.3 suggest that the RMS error of the proposed algorithm in along and across track is just less than 10 m and the horizontal positioning RMS error is approximately 15 m.

Table 4.3: Summary of error statistics for Data Set 1 using different receivers

Receiver Type	Along Error (m)		Across Error (m)		Horizontal Error (m)	
	Mean	RMS	Mean	RMS	Mean	RMS
HS receiver	24.3	25.1	37.7	42.8	47.9	49.9
Commercial Receiver	11.8	13.6	20.7	23.7	24.2	27.4
Proposed Algorithm	9.4	10.2	9.4	9.7	13.4	14.2

Table 4.4: RMS positioning improvement using the proposed algorithm for Data Set 1

Compared With	Along Error	Across Error	Horizontal Error
HS receiver	59 %	77 %	72 %
Commercial Receiver	25 %	59 %	48 %

Furthermore, from Table 4.4, it is observed that an improvement of at least 25% and 59% is observed in along-track and across-track respectively. Moreover, the improvement in the across-track accuracy of the proposed algorithm is profound (77% or 59%) due to the fact that the proposed algorithm is more sensitive in across track to changes in delta path delay and due to inherent weakness of the pseudorange-based methods. The horizontal error of the proposed algorithm is 48% to 72% better than what is possible with traditional methods. Collectively,

these results demonstrate that the proposed algorithm is a viable alternative and/or complement to pseudorange-based algorithms in urban canyon environments.

Error statistics presented in Table 4.3 indicate that the overall RMS of horizontal error is 14.2 m using the proposed algorithm, as indicated earlier in this section the positioning error depends on sky-visibility . More precisely, the horizontal error using the proposed algorithm is below 5 m for some locations but exceeds 20 m in others. Hence, a single RMS metric does not relay the full potential of the algorithm. With this in mind, Figure 4.14 shows a box and whisker plot of the horizontal errors as a function of sky-visibility. The box/whisker plot provides a visualization of summary statistics for sample data and contains the following features:

- The tops and bottoms of each "box" are the 75th and 25th percentiles of the samples, respectively. The distances between the tops and bottoms are the interquartile ranges.
- The line in the middle of each box is the sample median. If the median is not centered in the box, it shows sample skewness.
- The whiskers are lines extending above and below each box. Whiskers are drawn from the ends of the interquartile ranges to the furthest observations within the whisker length (1.5 times the interquartile range).
- Observations beyond the whisker length are marked as outliers and are displayed with a red plus sign (first seen in Figure 4.20).

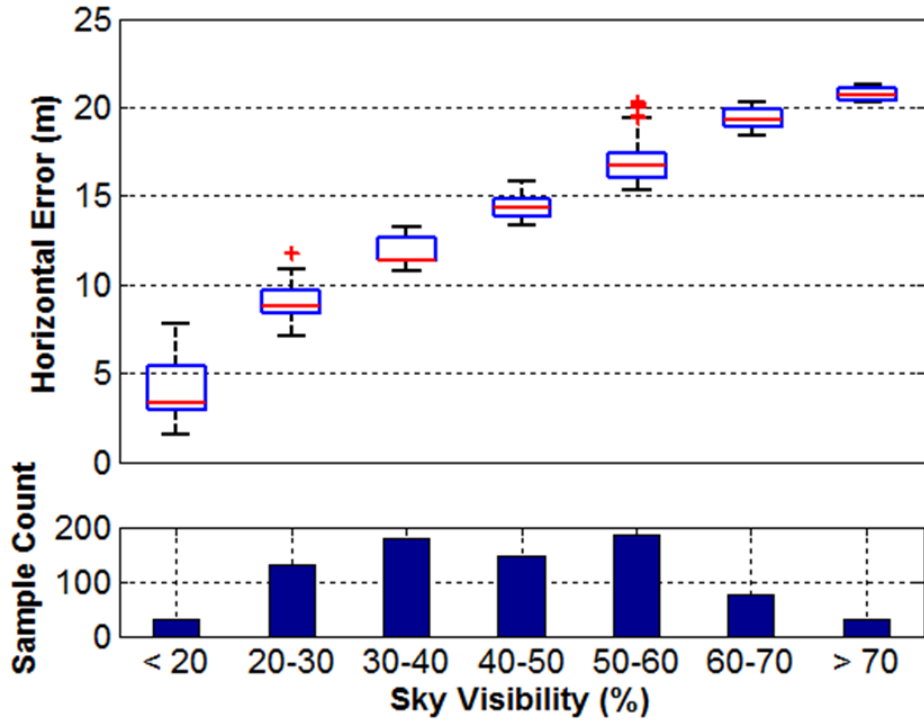


Figure 4.14: Box plot of horizontal positioning error as a function of sky-visibility for Data Set 1 along with the number of samples in each bin.

From Figure 4.14, for sky visibilities of 10-20%, the horizontal error has a minimum value of less than 2 m with median value of less than 5 m. It is evident from Figure 4.13 and Figure 4.14 that the proposed algorithm has better performance in poor sky-visibility. This fact shows and highlights benefits of the algorithm in deep urban areas where traditional positioning methods either fail or have degraded performance.

Results presented so far correspond to the entire trajectory for Data Set 1, which includes several epochs with static data. For a given static point, the measurement/reflection geometry is not changing (over the few seconds or minutes the vehicle is stopped) and thus the positioning accuracy is expected to remain approximately constant during this time. By extension, depending

on whether static points have high or low sky-visibility —and thus high or low position errors— this may result in overly optimistic or overly pessimistic statistics across the data set. To test this, the error statistics were recomputed using only epochs where the vehicle has a speed of at least 10 m/s, thus insuring that subsequent epochs have different measurement geometries. These statistics are shown in Table 4.5 along with the statistics across all epochs taken from Table 4.3.

Table 4.5: Summary of error statistics for Data Set 1 for epochs where vehicle speed was at least 10 m/s and for all epochs

Data	Along Error (m)		Across Error (m)		Horizontal Error (m)	
	Mean	RMS	Mean	RMS	Mean	RMS
Only epochs with speed greater than 10 m/s	9.4	10.2	9.5	9.7	13.7	14.5
All epochs	9.4	10.2	9.4	9.7	13.4	14.2

It is evident that the statistics for the entire trajectory are nearly same as those for all when the vehicle was moving. This implies that the positioning accuracy is independent of whether the receiver is moving. With this in mind, all of the following results are presented for all epochs.

4.3.3 Analysis of Data Set 2 and Performance Comparison with Data Set 1

Error statistics for Data Set 2 are presented in Table 4.6 and improvement in RMS position error is shown in Table 4.7. As with Data Set 1, the proposed algorithm performs better than the high-sensitivity and the commercial receiver. Furthermore an improvement of at least 11%, 26% and 22% was observed in along, across directions and horizontal positioning respectively.

Table 4.6: Summary of error statistics for Data Set 2 using different methods

Receiver Type	Along Error (m)		Across Error (m)		Horizontal Error (m)	
	Mean	RMS	Mean	RMS	Mean	RMS
HS receiver	8.9	10.3	10.7	11.6	14.9	16.2
Commercial Receiver	8.3	9.1	9.1	10.2	14.0	14.6
Proposed Algorithm	7.5	8.1	6.8	7.8	10.2	11.4

Table 4.7: RMS positioning improvement using the proposed algorithm for Data Set 2

Compared With	Along Error	Across Error	Horizontal Error
HS receiver	21 %	33 %	30 %
Commercial Receiver	11 %	26 %	22 %

Since the two data sets were collected with different front-end bandwidths, the relative performance of the SDM algorithm between the two data sets was desired to understand if front-end bandwidth was a critical parameter. Figure 4.15 depicts a performance comparison of the two data sets.

Based on this comparison alone, it seems that the performance of the lower front-end bandwidth (Data Set 2) is better than the larger front-end bandwidth (Data Set 1). However, these two data sets were collected separately on two different days and so to extend the performance comparison, the number of PRNs used for position estimation in each data set was analyzed.

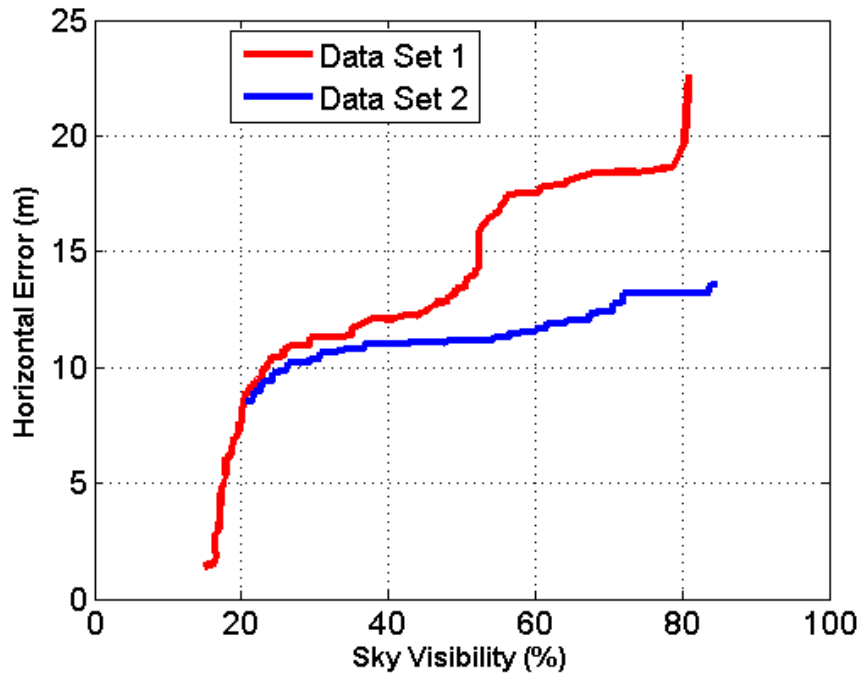


Figure 4.15: Comparison of RMS of horizontal error for the two data sets. Data Set 1 was collected with 20 MHz front-end bandwidth; Data Set 2 was collected with 4 MHz front-end bandwidth

As discussed in Section 3.2.4.1, satellites that have a single path at *all* CPs in the PG do not contribute to the solution. Correspondingly, the number of PRNs that contribute to a position estimate was computed as the number of satellites that had two or more predicted paths at *any* CP in the PG. Figure 4.16, shows number of PRNs used for position computation, as a function of sky-visibility.

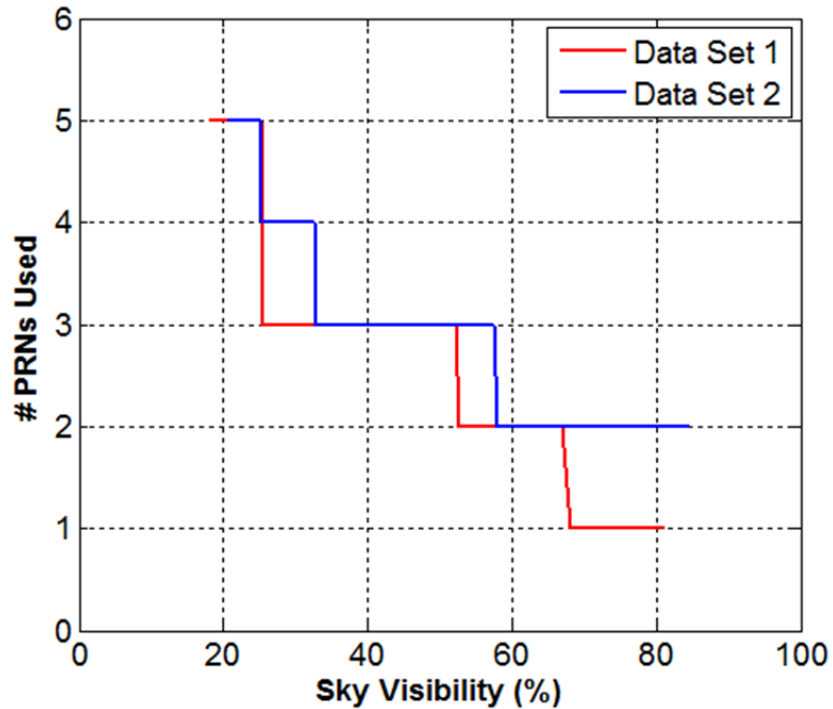


Figure 4.16: Number of PRNs used for position computation for the two data sets

From Figure 4.16, it is evident that Data Set 2 has more PRNs (satellites), used for position estimate, which partly explains results in Figure 4.15. However, there is considerable overlap of number of PRNs used, between the two Data Sets. This suggests that another factor may be playing a role. In particular, since a given PRN may have a different number of paths at different CPs based on the satellite and reflection geometry, the total number of paths could be different for similar sky-visibility.

With this in mind, the total number of paths (across all satellite) predicted at the final estimated position, plotted as a function of sky-visibility, is depicted in Figure 4.17.

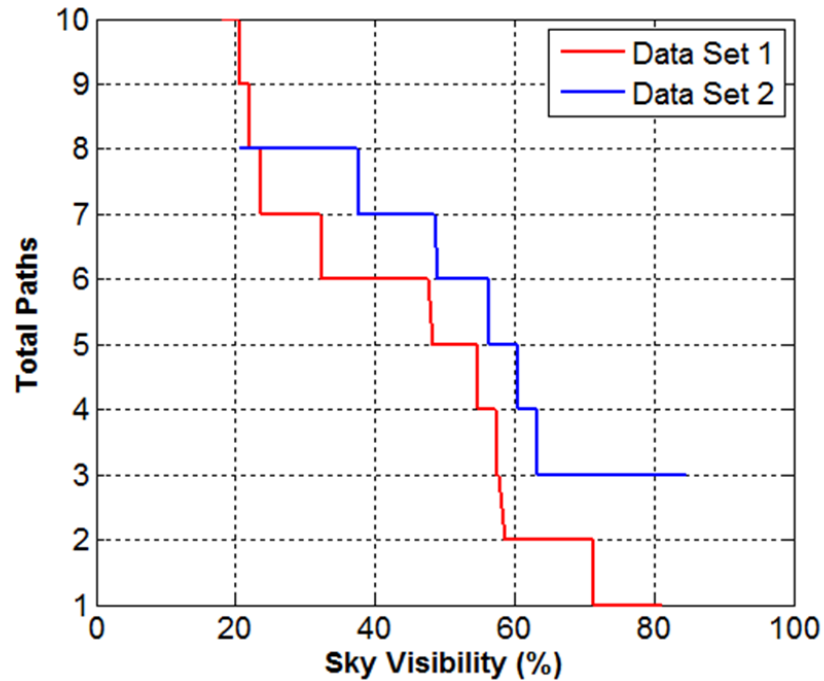


Figure 4.17: Total number of paths observed at estimated position, for the two data sets

It is evident that although the number of PRNs used for computing the position estimate was sometimes the same in both data sets, the total number of paths is clearly different.

To further investigate, Figure 4.18 and Figure 4.19 respectively show the horizontal error with respect to number of PRNs used to compute position and the total number of paths observed at the estimated position. It can be observed that the horizontal position error decreases with the addition of more satellites used in the position computation and with the total number of paths used.

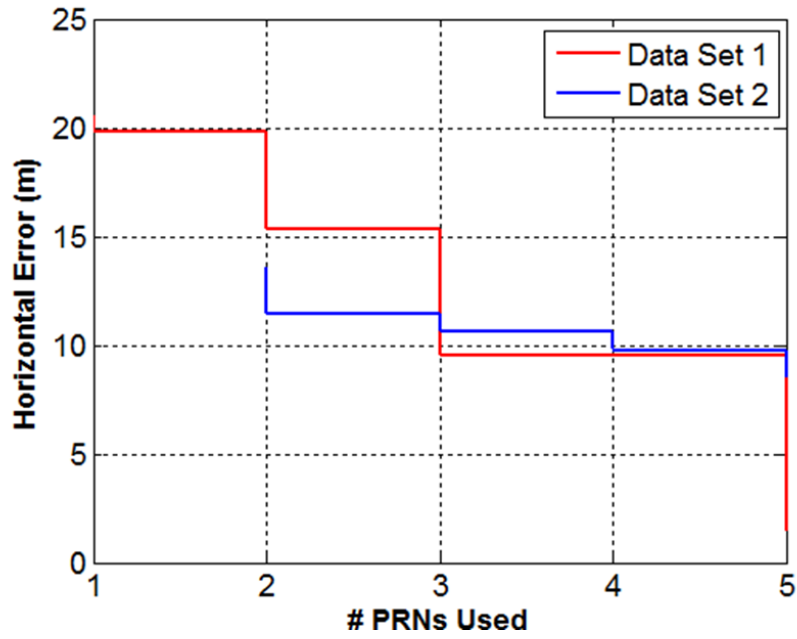


Figure 4.18: Effect of number of PRNs used on horizontal positioning accuracy

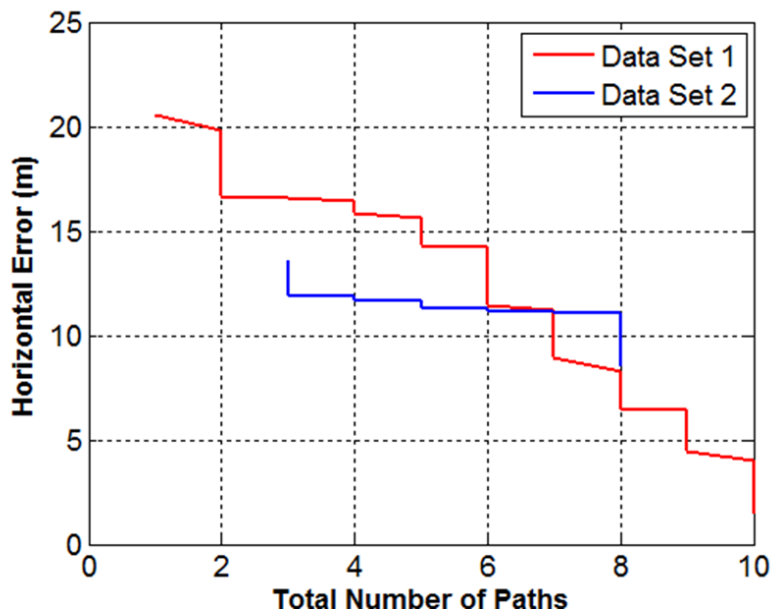


Figure 4.19: Effect of number of paths on horizontal positioning accuracy

Furthermore, Figure 4.18 indicates that the minimum error is approximately 2 m for Data Set 1 only about 11 m for Data Set 2, even though both solutions used the same number of satellites. This can be explained with the help of Figure 4.19 , which indicates that although the number of PRNs used was same for both the data sets, the number of paths observed were different for the two data sets.

These results indicate that sky-visibility, number of PRNs used and number of paths all contribute to the final position estimate, although there does not appear to be a single factor that completely explains the final positioning accuracy.

4.3.4 Statistics for Both Data Sets Combined

After analyzing the performance of the algorithm for the two data sets independently, this section analyzes performance across both data sets. The statistics of the horizontal error is depicted in Figure 4.20. These statistics are based on approximately 30 minutes and 7 km of trajectory in downtown Calgary.

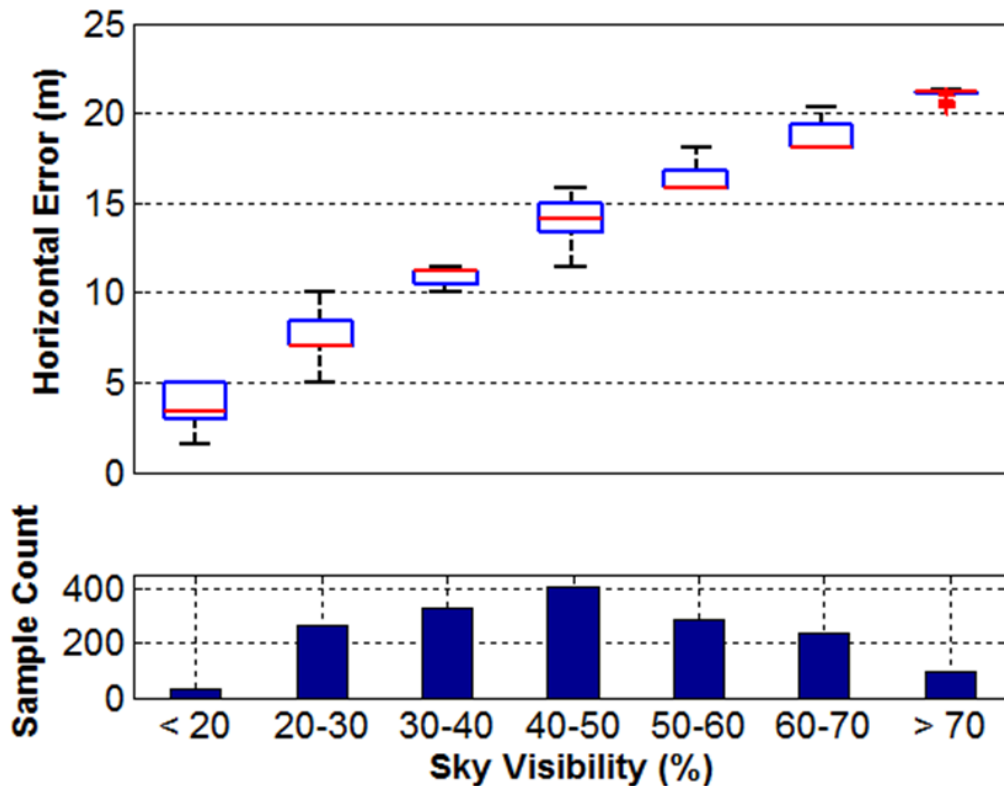


Figure 4.20: Box plot of horizontal positioning error as a function of sky-visibility for combined data sets (Data Set 1 and Data Set 2) along with the total number of combined samples in each bin.

The horizontal error has a minimum value of 2 m and the median horizontal error is approximately 3 m for sky visibilities less than 20 %. Furthermore, the error is less than 10 m for sky-visibility of less than 30 %. These results are very interesting as a traditional receiver's performance is degraded in these scenarios (i.e. in poor sky-visibility). However, the performance of the proposed positioning algorithm worsens as the sky-visibility increases and, as an extension, the proposed algorithm does not provide any solution in open sky; this is expected because in open sky there will not be any NLOS signals to provide input to the SDM algorithm.

After analyzing the performance of the algorithm for two different data sets, the following section provides the uncertainty bound of the positioning errors by proposed positioning algorithm.

4.4 Uncertainty of Estimated Position

The performance of any positioning algorithm is incomplete without quantifying the uncertainty associated with a given position estimate and, more importantly, ensuring the uncertainty is a reflection of the true estimation error. Hence, this section provides a method for quantifying the uncertainty associated with the proposed positioning algorithm and compares this with the actual position error. With this in mind, deriving an analytically/statistically rigorous uncertainty is beyond the scope of this thesis due to the highly non-linear characteristics of the algorithm. Instead, an empirical method of approximating the uncertainty using only data available to the algorithm is presented.

The motivation for selecting an empirical method for uncertainty can be linked to results from the in-depth analysis in Section 4.3.1 (see Figure 4.10 and Figure 4.12), where the two have different spreads of regions with the lowest RSS values (i.e., dark blue regions). More precisely, one epoch has a much wider blue region than the other epoch. These blue regions are of particular interest as it indirectly provides information about the uncertainty associated with the position estimate, with smaller regions suggesting more confidence in the solution. By extension, an empirical method can be used to analyze the uncertainty utilizing the spread of the blue region.

In order to quantify the uncertainty, the following steps were followed:

- Define a threshold for the overall RSS of residuals (RSSR) that can be considered to be of similar quality as the lowest RSS value. Essentially, this defines the RSS values that approximately correspond to the blue regions (at least in terms of shape; size will be discussed later) in Figure 4.10 and Figure 4.12.

The threshold (th) was defined using the minimum value of RSSR at a given epoch as defined as

$$th = RSSR_{\min} + (RSSR_{\max} - RSSR_{\min}) \cdot k \quad (4.1)$$

where:

$RSSR_{\min}$:	minimum RSSR
$RSSR_{\max}$:	maximum RSSR
k	:	empirically-derived scale factor

In other words, the RSSR threshold is the k -th percentile value within a given PG. The procedure used for selecting the value of k is explained below.

- The uncertainty in north (P_N) and east (P_E) direction was then defined as below

$$\max \left\{ \left| N(RSSR_{\min}) - \max \{ N(RSSR < th) \} \right|, \left| N(RSSR_{\min}) - \min \{ N(RSSR < th) \} \right| \right\}$$

$$\max \left\{ \left| E(RSSR_{\min}) - \max \{ E(RSSR < th) \} \right|, \left| E(RSSR_{\min}) - \min \{ E(RSSR < th) \} \right| \right\}$$

where $N(\cdot)$ and $E(\cdot)$ respectively refer to the northing and easting coordinates whose RSSR values are given by the bracketed value.

- The uncertainty in horizontal direction (P_H) was obtained from the north and east

uncertainties as:
$$P_H = \sqrt{P_N^2 + P_E^2}$$

In order to find the optimum value of k , a linear relation between the true estimation error and uncertainty was obtained. Using the steps explained above results for three different values of k (20%, 30% and 50%) Figure 4.21, Figure 4.22 and Figure 4.23 respectively show the east, north and horizontal uncertainty values as a function of the true estimation error.

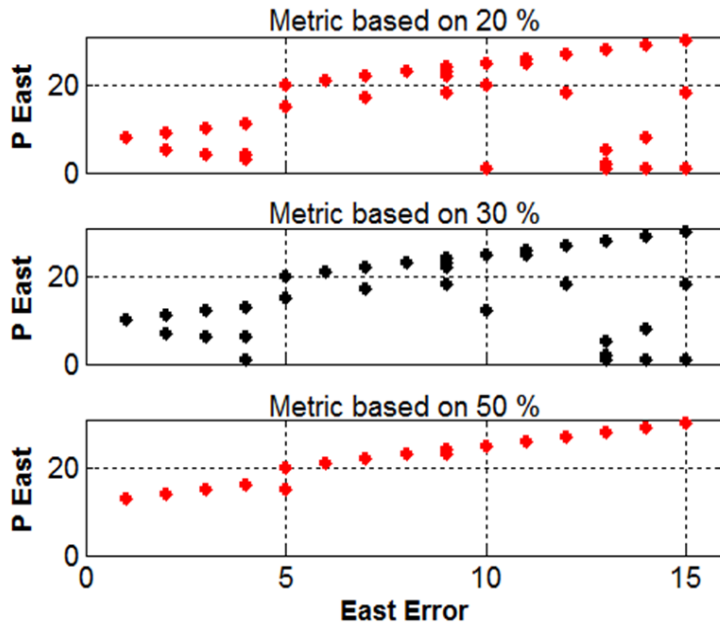


Figure 4.21: Relation between easting error and maximum uncertainty in east direction based on the metric for three different factors, 20 %, 30 % and 50 %

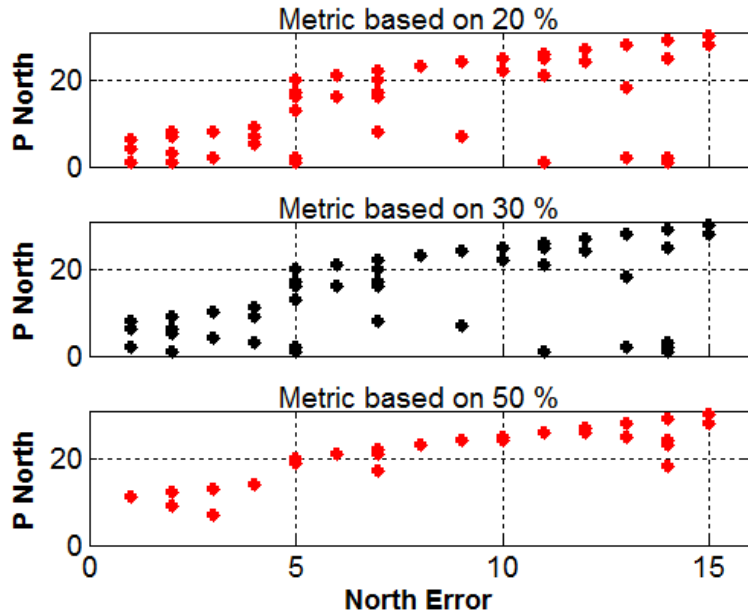


Figure 4.22: Relation between northing error and maximum uncertainty in north direction based on the metric for three different factors, 20 %, 30 % and 50 %

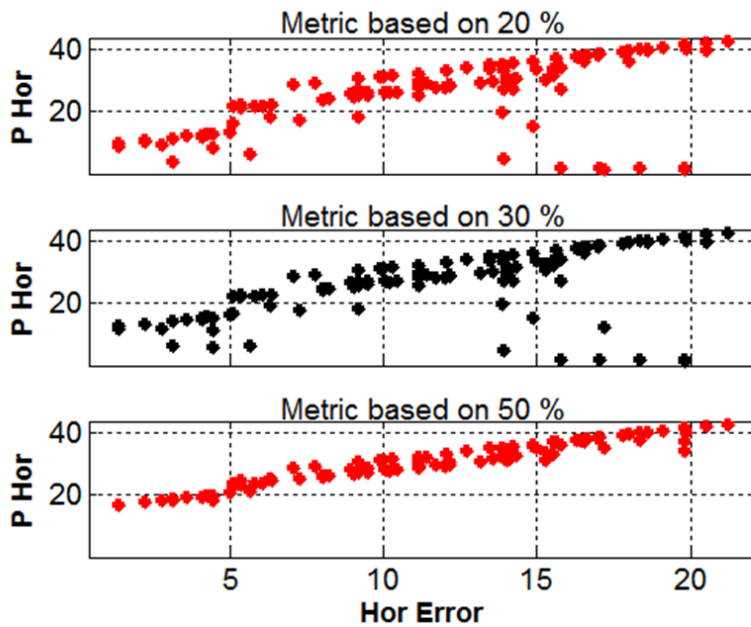


Figure 4.23: Relation between horizontal error and maximum uncertainty in horizontal direction based on the metric for three different factors, 20 %, 30 % and 50 %

These plots were generated using Data Set 1 only. It is observed that the metric corresponding to k as 50 % provides the most linear relationship between the estimation error and the uncertainty value. In addition, this is also the value that produced the fewest “outliers”, that is, solutions with large errors but small uncertainty values. Hence, the optimum value of k based on the results shown was selected as 50%.

A key characteristic of Figure 4.21, Figure 4.22 and Figure 4.23 is that the linear relationship does not pass through the origin. In other words, the uncertainty estimate is overly large (i.e., the uncertainty region has the wrong size). To deal with this, a linear fit was obtained to relate the actual error with the uncertainty estimates. The assumption with this is that the linear fit could be applied across all data sets. In order to test this assumption, the linear coefficients were obtained using Data Set 1 but were applied to data in both data sets and the result is shown in Figure 4.24.

It is evident from Figure 4.24, that there exists a nearly one-to-one relation between the estimation errors and corresponding uncertainty values. This also implies a level of reliability since there are no epochs for which the true error is significantly larger than the estimated uncertainty. As mentioned earlier in this section, this method of obtaining the uncertainty might not be optimal, but Figure 4.24 suggests this is a reasonable first attempt.

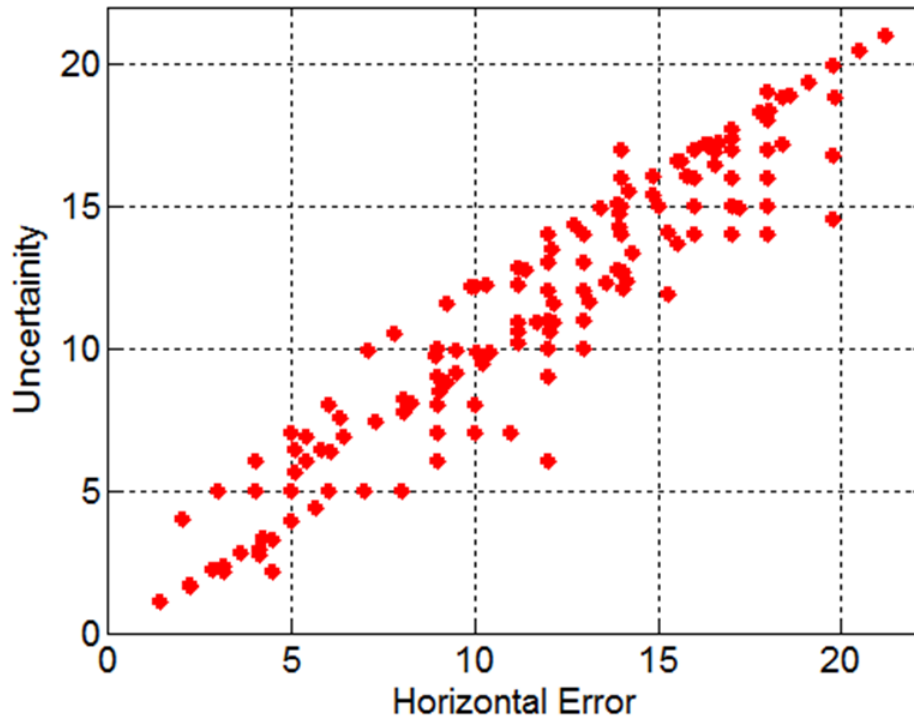


Figure 4.24: Linear fit between horizontal error and estimated horizontal error based on maximum uncertainty obtained from the pre-defined metric

4.5 Summary

This chapter presented the performance of the *3D Building Model-assisted Snapshot GNSS Positioning* method based on results and analysis of two different data sets collected in downtown Calgary. The criterion for performance evaluation was horizontal position accuracy of the proposed algorithm with respect to a reference solution accurate to few centimeters. The performance of the proposed algorithm was also compared with a commercial receiver and a high-sensitivity software receiver. Following is the summary of the results and analysis:

- One of the most important findings was that the proposed algorithm had a relationship between horizontal error and sky-visibility with less sky-visibility yielding smaller position errors. The proposed algorithm's performance was *best* (in terms of horizontal positioning error) for least sky-visibility; where the traditional pseudorange-based receivers either does not work or have worst performance in terms of accuracy
- The performance of the proposed algorithm was found to be dependent on sky-visibility, number of PRNs used for position computation and number of paths
- The proposed algorithm provides better results than traditional methods even with a smaller front-end bandwidth which is an indicative of low cost, mass market application of the proposed algorithm; this combined with above conclusion, indicates that the proposed algorithm has potential for applications in dense urban areas for low cost mass market applications
- Finally, an empirical method was proposed to access the uncertainty of the position estimate; results suggest a linear relationship between error and uncertainty; a detailed mathematical formulation for uncertainty is left as future work (discussed in chapter 6)

The results presented were based on a single set of processing parameters (section 4.2). However, to better understand algorithm behavior, Chapter 5 describes a sensitivity analysis of the proposed algorithm to the various processing parameters.

Chapter Five: **Sensitivity Analysis of 3DBM-assisted Snapshot Positioning Method**

The previous chapter demonstrated that performance of the proposed algorithm was better than a commercial receiver and a high-sensitivity receiver, especially in deep urban canyons with poor sky-visibility. However, that performance was analyzed using only one set of processing parameters (Table 4.1 and 4.4 of Chapter 4). This Chapter provides a detailed analysis of algorithm performance using different processing parameters.

5.1 Key Processing Parameters

With reference to Figure 3.7, the proposed algorithm is a function of following parameters:

- **Quality of initial position:** An initial position and its uncertainty is provided as input to the algorithm, hence if the initial position has larger uncertainty the size of the position grid should be larger in order to include the true position.
- **Number of candidate points inside the position grid:** More candidate points implies a finer resolution when obtaining the final position estimate, provided the position grid is sufficiently large to capture the true location.
- **Effect of timing error:** Since the proposed method deals with snapshots of GNSS data and decoding transmit time is not possible from few milliseconds of IF data, the amount of clock/timing error in the receiver is a critical parameter for operational systems.
- **Coherent integration time:** The correlators are expected to be noisier for lower coherent integration time and since these are used as observations by the signal delay matching algorithm, different coherent integration times are expected to yield different positioning accuracies.

The primary objective of this chapter is to analyze the sensitivity of the proposed positioning algorithm to the above processing parameters. The primary approach used was to reprocess the data from Data Set 1 using different parameters and to then compare results with those obtained originally. The sensitivity analysis is presented in detail for one point on the trajectory (yellow star in figure 4.3); this point is referred as the “epoch under consideration”. After the detailed analysis for a single point, comparison statistics are presented for the entire trajectory. Each of the following sections presents the analysis procedure and corresponding to a specific processing parameter.

5.2 Sensitivity to Size of PG

Since the algorithm requires an initial user position, the uncertainty in this position would affect the size of the PG. For a larger uncertainty; the size of grid should be large enough to capture the true location. Ideally, the final estimated position should not vary with size of the PG, but this needs to be verified. If not satisfied, the resulting solution would be biased and the estimated uncertainty would not match the true error. Whereas the results presented in Chapter 4 were obtained for a PG size of 30x30 m, this section considers a PG size of 200x200 m.

Figure 5.1 shows the RSS of residuals across a 30x30 m position grid with 1 m spacing for PRN 1 at the location under consideration. As before, the true position is located at the centre of the grid and, as expected, the residuals are smallest around this point. The RSS of residuals for the same PRN for a 200x200 m grid is shown in Figure 5.2, where the shaded regions depict the surrounding buildings (all CPs falling “inside” a building are excluded from the algorithm). The grid resolution was selected as 5 m, to reduce the processing load.

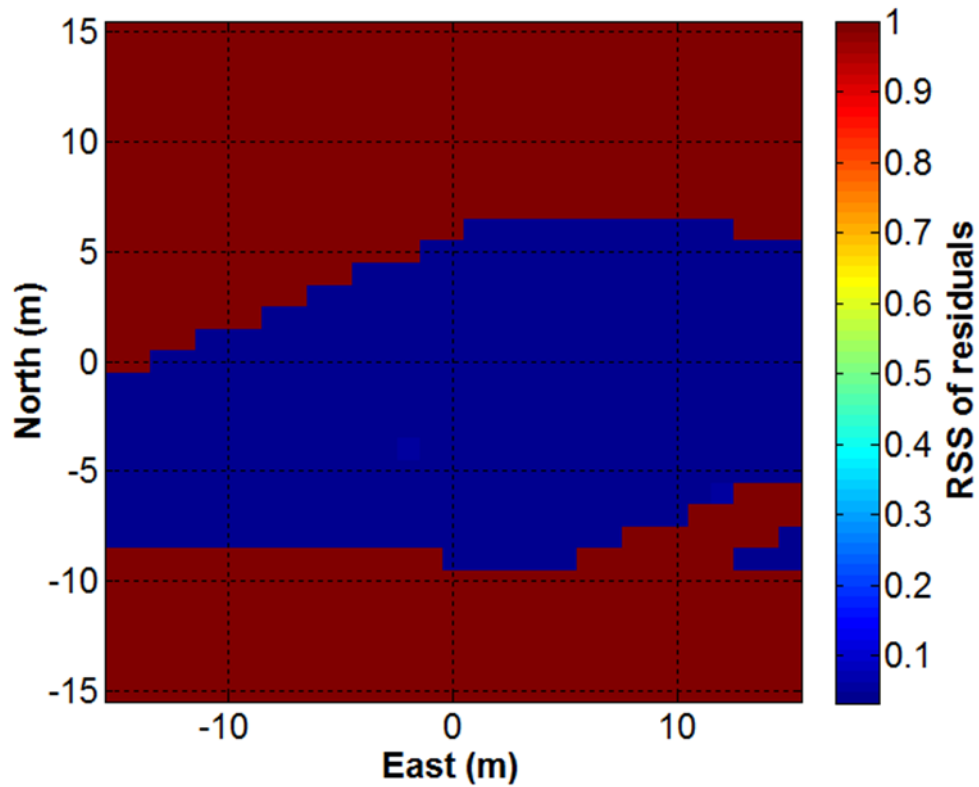


Figure 5.1: RSS of residuals for PRN 1 (Az: 297°, Elve: 42°); size of position grid is 30x30 metres

Ideally, it is expected that the RSS of residuals should increase for CPs farther from the true location. In general, this is the case in Figure 5.1 and Figure 5.2, especially in the north-south direction (although the values appear to be approximately binary in nature). However, in the east-west direction the 200x200 m grid shows several more CPs with low RSS of residuals east of the true location.

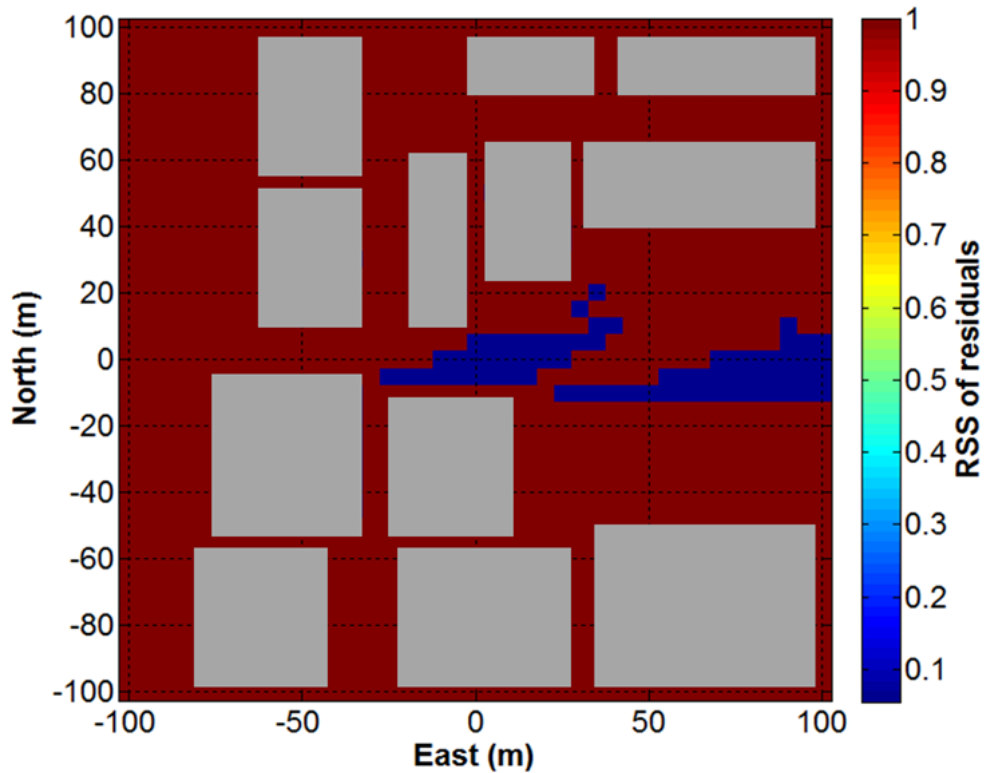


Figure 5.2: RSS of residuals for PRN 1(Az: 297° , Elev: 42°); size of position grid 200x200 metres; shaded regions are buildings and are excluded from position grid for RSS of residuals calculation

Since the position is not typically computed from a single satellite, the increased east-west spread for the 200x200 m case is not a major concern. Nevertheless, if only this particular satellite is used, the computed position for the 200x200 m case has an error of 20 m in the east and 5 m in the north. The error in case of 200x200 m position grid apparently seems large; however, it is worth mentioning that the resolution of the position grid is 5 m in this case as opposed to 1 m in case of 30x30 m grid.

With regards to Figure 5.2, in order to explain the distribution of points in the east-west direction with small RSS values, we consider that PRN 1 has an azimuth of 297° and so its signals will most likely reflect from building south and/or east of the user. In this case, since there are no significant reflectors to the east, the signal is most likely being reflected from a building towards south of the user. However, for a reflector whose normal vector points towards north, a change in the east-west position of the user will not have much effect on the predicted path length and hence the LSQ RSS of residuals should be nearly constant meaning the algorithm is not as sensitive in this direction. This can also be explained further with equation 2.31 which indicates that the path delay is function of normal distance from reflector. By extension, any change in position along a direction perpendicular to the reflector would yield a larger variation in RSS of residual, as compared to a change in other directions.

Figure 5.3 and Figure 5.4 show the RSS values summed across all satellites for the 30x30 m grid and the 200x200 m, respectively. Comparing these figures with the results in Figure 5.1 and Figure 5.2 (PRN 1 only), adding information from more satellites gives fewer regions with “small” RSS residuals, which is expected. In this case, the final position estimate in the 200x200 m case has an error of 5 m easting and 5 m northing. The improvement in east-west error (with respect to using only PRN 1) is obvious due to the inclusion of RSS of residuals from other satellites.

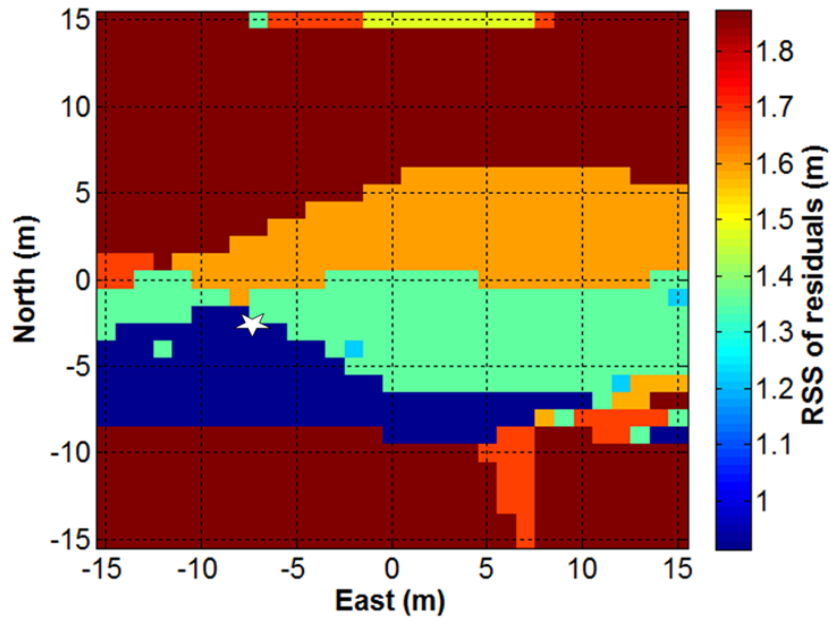


Figure 5.3: RSS of residuals due to all PRNs present at this epoch; size of position grid is 30x30 metres. The white star represents the final estimated position

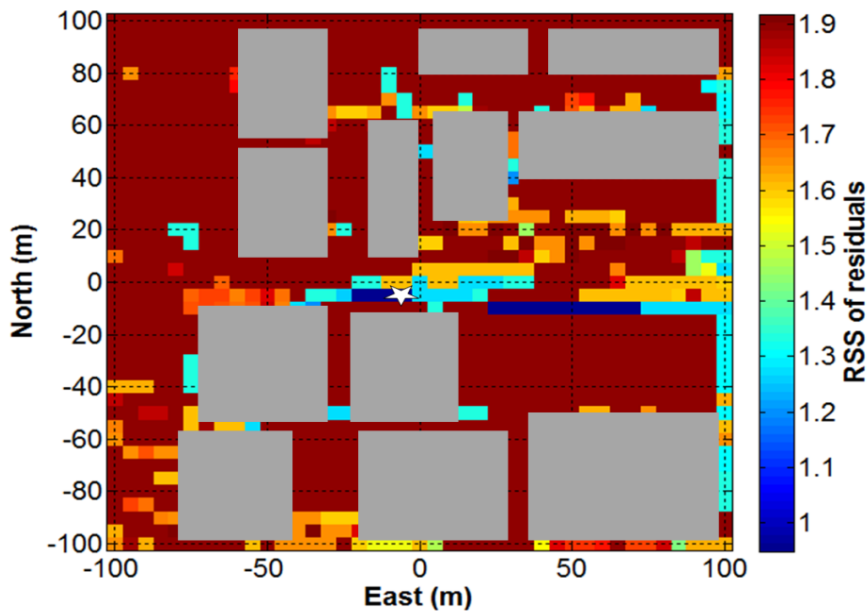


Figure 5.4: RSS of residuals due to all PRNs present at this epoch; size of position grid is 200x200 metres; shaded regions are buildings and are excluded from position grid for RSS of residuals calculation. The white star represents the final estimated position

Results presented here indicate that increasing the size of the position grid does not significantly change the final estimated position. This suggests that the likelihood of obtaining a highly biased solution is quite low.

To confirm these findings, positions were computed across the trajectory (once per ten seconds) for a PG size of 200x200 m with a grid resolution of 5 m. The results were compared with a grid size of 30x30 m, also with a 5 m grid resolution. The error statistics are shown in Table 5.1 and indicate that the algorithm is virtually insensitive to the size of the position grid.

Table 5.1: Comparison of RMS of horizontal error for entire trajectory using different grid sizes

30x30 m grid size	200x200 m grid size
15.4 m	15.8 m

5.3 Sensitivity to Resolution of PG

Since the estimated position is one of the candidate points inside the position grid, the resolution of the grid will affect the quality of the final solution. More precisely, increasing the grid resolution results in increased number of candidate points for a given grid size. This, in turn, should increase the likelihood of obtaining a candidate point closer to the true location but the processing load will have to increase to accommodate the increased number of candidate points under consideration.

In order to analyze the sensitivity of the proposed algorithm with respect to the grid resolution, RMS error of horizontal positions were compared for a grid resolution of 0.5 m, 1 m and 5 m,

keeping other processing parameters same. Performance of these two cases was compared in terms of processing load (due to change in number of CPs) and horizontal position accuracy.

The horizontal error in final estimated position and number of Candidate Points for a grid resolution of 0.5 m, 1 m and 5 m are presented in Table 5.2 for same trajectory points as in section 5.3. As expected, the horizontal error for the finer grid resolution is better than for the larger grid resolution. Also shown in Table 5.2 is that this comes with an increase in processing load, as reflected by the number of candidate points that need to be considered.

Table 5.2: Performance comparison for different grid resolutions for a 30x30 m grid

Grid Resolution (GR)	Number of CPs	change in CPs (with respect to 1 m GR)	RMS Horizontal Error	Relative Error (with respect to 1 m GR)
1 m	961	N/A	12.8 m	N/A
0.5 m	3721	+ 287 %	11.5 m	-10 %
5 m	49	-95 %	14.1 m	+ 11 %

Compared to the case of a 1 m grid spacing:

- The horizontal error for the 0.5 m grid resolution is only slightly better (reduction of 1.3 m compared to the case of 1 m grid spacing) but at the cost of a nearly three-fold increase in the number of CPs, and hence processing load.
- The horizontal error for the 5 m spacing increased by 1.3 m (11% increase) with a 95% reduction in processing load.

These results are as expected, since the increase in grid resolution is expected to give better positioning accuracy at the cost of increased processing load and vice-versa. Based solely on these results, it would seem that a 0.5 m resolution is not worth the computational tradeoff but a 1 m or 5 m resolution would be sufficient, depending on the accuracy requirements.

These results also suggest that the 3DBM-assisted snapshot positioning algorithm can be made more efficient by implementing a multi-stage approach. More precisely, a coarser grid can be used to obtain a refined position estimate (compared to the approximate position used to initialize the algorithm); then a smaller, finer grid could be generated around that point to get the final estimate.

5.4 Sensitivity to Error in Transmit Time

The proposed positioning algorithm uses snapshots of GNSS data where receiver times are not often known precisely, leading to errors in satellite positions due to incorrect transmit time (i.e., the “coarse time” problem) as explained in section 2.4.2.1. The sensitivity of the proposed algorithm to receiver timing errors is therefore critical to understanding its practicality for real-world application. Sensitivity to timing error is first assessed theoretically and then tested by injecting an intentional timing error and comparing results corresponding to the “true” time.

In traditional pseudorange-based positioning, because of satellite motion (~ 4 km/s), an error of 1 s in transmit time (which, in turn, produces a wrong satellite position), corresponds to an error in range of up to about 800 m, which eventually leads to hundreds of metres of position error (Van Diggelen 2009). Since the proposed method is based a snapshot of data, a precise transmit time

cannot be computed as explained in chapter 2, hence the effect of timing error becomes a crucial part of analysis.

In order to analyze the sensitivity of the 3DBM-assisted positioning algorithm with respect to the timing error, Figure 5.5 shows a satellite at location ‘a’ at a particular time, along with the signal path that is incident on a reflector located near the receiver. The reflector is at a perpendicular distance ‘d’ from the receiver and θ is the angle of incidence defined with respect to the normal vector of the reflecting surface. Although Figure 5.5 is shown in 2D, the 3D scenario is effectively the same except θ is a function of both azimuth and elevation.

For this given scenario the path delay ($\delta\tau$) of the reflected signal is given by equation 2.31, repeated here for convenience:

$$\delta\tau = 2 \cdot d \cdot \cos(\theta) \quad (5.1)$$

Any error in satellite transmit time (as derived from the receiver time), would lead to a wrong satellite position. Hence, assuming an error in transmit time, the satellite would be at a different location along the orbit, say at ‘b’ in Figure 5.5. Taking the time derivative of the above equation yields

$$\frac{d(\delta\tau)}{dt} = -2 \cdot d \cdot \sin(\theta) \cdot \frac{d\theta}{dt} \quad (5.2)$$

where, $\frac{d\theta}{dt}$ is the rate of change of the incident angle. An approximate worst-case value for this is the angular rate of satellites as viewed from the centre of the Earth (i.e., the satellite's mean anomaly):

$$\max(d\theta / dt) \approx \frac{V_s}{R} \quad (5.3)$$

where V_s is the satellite orbit speed and R is the distance from the centre of the Earth to the satellite.

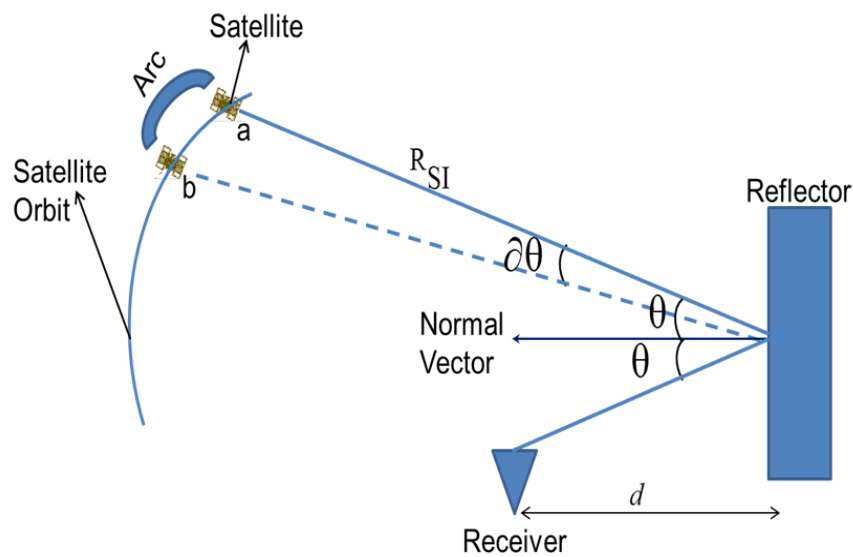


Figure 5.5: Scenario with a reflector near-by receiver and reflections reaching the receiver

Continuing with the pessimistic analysis, $d = 0.5$ code chips and $\theta = 90^\circ$ (such that $\sin(\theta) = 1$); would yield a maximum path delay of 1 chip which is the largest that can impact the correlation

function peak. Then, using GPS specific values for V_s and R , the worst-case error in path delay,

$$\text{that is } \left[\frac{d(\delta\tau)}{dt} \right]_{\max} \cong 0.05 \text{ m/s}.$$

In other words, the delta path delay error is less than 5 cm per second of timing error. Given the level of code phase noise and the magnitude of orbit and atmosphere errors, this level of error is quite small.

It is also worth noting that 5 cm per second of timing error is about four orders of magnitude smaller than the absolute code phase error that is used for traditional coarse-time positioning approaches (Van Diggelen 2009), which are proportional to the geometric range rate between the receiver and satellite (up to about 800 m/s). In this regard, the 3DBM-assisted snapshot positioning approach should be much better suited to coarse-time positioning applications.

To confirm the above, Table 5.3 shows the error in path delay computed for PRN 1 for timing errors up to 10 s. As can be seen, the path delay errors are 2 cm or less. These values are less than the worst case error analysis performed above, which is 50 cm per 10 second timing error (as explained above).

In order to show the effect of transmit time error on the 3DBM-assisted snapshot positioning algorithm, Figure 5.6 shows the *difference* in RSS of residuals for PRN 1 compared to what was shown in Figure 5.1 after introducing an error of 10 s in the transmit time. The difference in RSS of residuals is nearly zero everywhere.

Table 5.3: Error in path delay, azimuth and elevation of point of intersection of incident ray and reflector as a function of transmit time error

Error in Transmit time	Azimuth to point of intersection	Elevation to point of intersection	Delta path delay	Error in delta path delay
0 s (true transmit time)	247.31°	42.01°	5.68 m	N/A
1 s	247.32°	42.02°	5.68 m	0 m
5 s	247.35°	42.04°	5.67 m	0.01 m
10 s	247.39°	42.06°	5.66 m	0.02 m

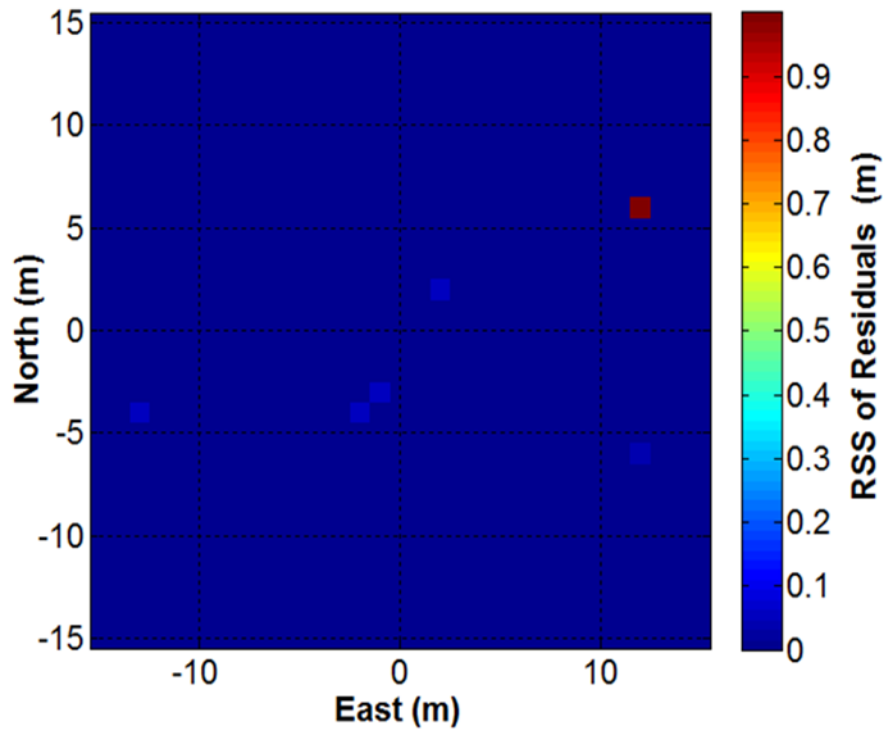


Figure 5.6: Difference in RSS of residuals for PRN 1 (Az: 297°, Ele: 42°), relative to Figure 3, due to a transmit time error of 10 s

The difference is larger at a single CP (difference of more than 0.9) because of a change in the number of predicted paths at that CP due to timing error of 10 s (compared to the “true” time case). Since predicting the wrong number of paths would lead to larger RSS of residuals compared to corresponding to “true” number of paths, these results make sense. More importantly, the final estimated position was exactly the same as for the timing-error-free case.

Finally, the process of timing error injection was repeated for the entire trajectory of 2.5 km for an error injection of 5 s. It was observed that the mean difference in path delay was 0.08 metres and the position estimate was the same as for the case with no timing errors.

Overall, these results show that using delta path delay’ or position computation is nearly insensitive to the transmit time error.

5.5 Sensitivity to Coherent Integration Time

Since correlator outputs are used for matching with predicted parameters, and since the coherent integration time affects the amount of noise in the correlator outputs, it follows that the quality of match will be affected by the coherent integration time used. In turn, this will affect the quality of final estimated position. Hence, the sensitivity analysis of the algorithm with respect to coherent integration becomes important.

Sensitivity to coherent integration time is assessed by comparing the RMS error of horizontal position for 10 ms, 20 ms and 100 ms coherent integration times. The resulting RMS horizontal position errors along with mean and standard deviation for these cases are shown in Table 5.4.

Table 5.4: Effect of coherent integration time on proposed positioning algorithm

Coherent Integration Time	Mean	Std. Deviation	RMS Horizontal Position Error
10 ms	13.7 m	4.8 m	14.5 m
20 ms	13.5 m	4.3 m	14.1 m
100 ms	13.5 m	3.7 m	13.9 m

Compared with the 10 ms case, the RMS of horizontal error for 20 ms CIT differed by only 50 cm (improvement of approximately 3%). There is also marginal improvement of positioning performance when CIT was increased to 100 ms from 10 ms (RMS error decreases by 4 % to 13.9 m). This marginal improvement is expected since CIT primarily affects the level of noise in the correlator, but does not affect the overall shape. This allows for the relative path delays to be estimated with slightly more noise, but without additional systematic errors. To illustrate this, Figure 5.7 shows correlator outputs for 10 ms and 100 ms CIT values (normalized to unit power to facilitate comparison). It is clear that the overall shape of the correlator outputs is the same, implying the same delta path delays should be estimated in both cases, thus leading to similar position estimates.

Based on these results, the 3DBM-assisted snapshot positioning method is considered to be only marginally sensitive to CIT. This is an important finding and suggests that there is no obvious benefit to extending coherent integration time, thus circumventing the challenges with doing so. In particular, it means that data bit aiding is not required and lower-stability clocks can be used. Collectively, this leads to a simpler implementation of the receiver.

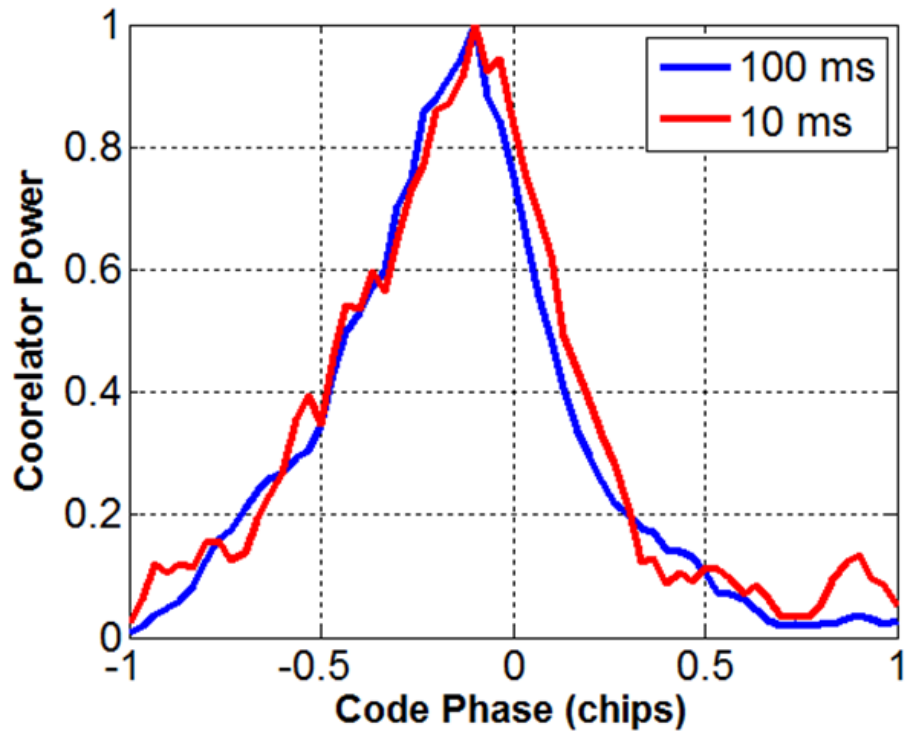


Figure 5.7: Normalized correlator outputs for 10 ms and 100 ms coherent integration times. The correlator output corresponding to 10 ms is noisier compared to that of 100 ms

5.6 Summary

This chapter presented a detailed sensitivity analysis of the 3DBM-assisted snapshot positioning algorithm with respect to various processing parameters such as: grid size, grid resolution, error in transmit time, and coherent integration time. Based on results, the proposed algorithm is largely insensitive to all of these parameters (size and resolution of PG, transmit time error and effect of coherent integration time), which has the following practical benefits:

- Increasing the initial position uncertainty is unlikely to result in a biased solution
- Varying the grid resolution from coarse-to-fine could yield a more efficient implementation

- The receiver can have much less stringent requirements for maintaining time between snapshots compared to traditional coarse time receivers (because of the insensitivity to coarse time error)
- The receiver architecture can be simpler because extended coherent integration time does not provide appreciable position accuracy improvements

These findings strongly suggest the potential benefits of the proposed algorithm in urban canyon environments, over traditional positioning methods.

Chapter Six: **Conclusion and Future Work**

This thesis presented a novel positioning algorithm, refereed as “3DBM-assisted Snapshot GNSS Positioning” method that uses a unique SDM-based position technique. Based on the results and analyses described in previous chapters, this chapter provides the conclusion regarding the different aspects of the algorithm. Later, a list of recommendations for future work is presented.

6.1 Summary and Novelty of Research

The novelties of the proposed positioning algorithm can be listed as below:

- The proposed algorithm is based a unique SDM technique that provides position estimates based on the delta path delay of NLOS signal with respect to the shortest received path signal. Thus the proposed algorithm is unaffected by traditional GNSS error sources such as receiver clock error, atmospheric errors, orbital error etc.
- Since the proposed algorithm is based on snapshots of GNSS data, use of continuous tracking and hence tracking loops are unnecessary, providing all benefits of tracking-free GNSS receiver; moreover the proposed algorithm is nearly insensitive to timing errors which suggests coarse time estimation is unnecessary even while using snapshot of GNSS data
- The proposed algorithm is different than previously proposed methods using NLOS signals constructively, since the proposed method utilizes all NLOS signals and is not based on pseudorange. More precisely, constructive use of NLOS signals for pseudorange-based method, are still affected by traditional pseudorange-based errors as explained above. Furthermore, techniques such as shadow matching do not utilize all NLOS signals

- In addition to the novelties presented above, the research resulted in a novel technique for multipath parameter estimation resulting in better performance of multipath parameter estimation

In order to assess the performance of the proposed positioning technique, two different data sets were collected in downtown Calgary and the performance in terms of RMS of horizontal position error was compared against two pseudorange-based approaches. The combined data set was 7.5 km long travelled using a vehicle with a maximum speed of 15 m/s. The following section contains the conclusions based on the results presented.

6.2 Conclusions Based on Results Analysis

Based on the results obtained in this work, the following conclusions can be drawn:

- The proposed algorithm exhibits a relationship between horizontal error and sky-visibility with performance occurring with lower sky visibilities. This contrasts with traditional pseudorange-based receivers which either do not work or have degraded accuracy with lower sky-visibility. The performance degradation with increasing sky-visibility is because the current algorithm only uses NLOS signal (i.e., no LOS signals), for which there are fewer in more open areas.
- Based on the data analyzed, the proposed method did not produce degraded results when changing from a 20 Hz to a 4 MHz front-end bandwidth suggesting it is well suited to low cost, mass market applications.
- The proposed algorithm's RMS horizontal positioning error ranged from 2 m when sky-visibility was less than 20% to 20 m as sky-visibility increased to 60%. Furthermore, an

improvement of at least 27% (up to 46%) in terms of RMS error was observed for horizontal positioning, compared to two traditional pseudorange-based methods.

- The proposed algorithm was shown to have better accuracy in the across track direction than in the along-track direction. Compared to traditional receivers improvements in the across- and along-track directions were at least 32% (up to 57%) and at least 12% (up to 21%), respectively.
- An empirical method was proposed to assess the uncertainty of the position estimate and results show a near-linear relationship between error and uncertainty.
- Although time aiding information can be obtained from cell phone towers, in the absence of such aiding, timing becomes a major source of error in traditional positioning methods. In contrast, the proposed positioning algorithm was found to be nearly insensitive to the timing errors with errors in the delta path delay having a maximum value of less than 5 cm per second of timing error. This was confirmed by introducing timing errors of 10 s and observing that the algorithm produced identical position errors as compared to the case with no timing errors. This contrasts with the traditional pseudorange-based positioning methods, where the every second of timing error results in 100s of metres of ranging errors, thus forcing the inclusion of a coarse time state that reduces system observability and generally degrades positioning accuracy.
- The proposed algorithm was shown to be nearly insensitive to coherent integration time. The RMS horizontal error improved by only 4% only when coherent integration time was increased from 10 ms to 100 ms due to an decrease in correlator noise. The ability to use as little as 10 ms of data suggests that proposed algorithm does not require external data

bit aiding or a stable clock. Furthermore the proposed receiver architecture would be much simpler to implement since data bit aiding is unnecessary.

- The positioning algorithm was found nearly insensitive to the size of the position grid and marginally sensitive to the grid resolution. Compared to a 1 m grid resolution, RMS horizontal position error was only 10% better when using a 0.5 m grid resolution, but this comes at the cost of a three-fold increase in processing load. On the other hand, decreasing the grid resolution to 5 m produce a degradation of only 11% with processing load reductions of 95%. This suggests that the positioning algorithm can be implemented with a coarse (larger) grid resolution to estimate a coarse position and then refined with a finer grid resolution

The above conclusions suggest that the proposed positioning algorithm could be a low cost and efficient solution for positioning in urban environments. However, the performance of the proposed algorithm can be improved further as discussed in the following section.

6.3 Recommendations for Future Work

Following are the recommendations for future work to extend and/or improve the proposed 3DBM-assisted Snapshot GNSS Positioning algorithm:

Integration of LOS-based Signal Information

Based on results presented in Chapter 4, it is observed that the proposed algorithm performs better when NLOS signal information is available to the algorithm and the performance of algorithm deteriorates in areas where sky-visibility was more than 60%. By extension, the algorithm breaks in open sky scenarios where there is no NLOS signal present. One possible

solution to this problem is to integrate LOS-based signal to the proposed algorithm to use the LOS-based signal information in absence of NLOS signals.

Improving Efficiency of the Proposed Algorithm

The huge processing requirement by the ray-tracer for several CPs inside the PG is time consuming specially for a larger grid size. This can be a bottleneck for real-time application of the proposed algorithm. However, there are several ways to handle this problem:

- All the ray-tracing processing can be done offline and can be stored for real-time applications. However, this does not solve the problem if the positioning has to be done for new buildings which were not present in stored information.
- A more practical approach (compared to above point) is to define a variable grid resolution and grid size, based on uncertainty of the initial position provided. More precisely, define a larger grid with coarse grid resolution to first obtain a coarse position estimate and later improve the position estimate by defining finer grid resolution around the estimated coarse position estimate.
- Finally, the efficiency of the ray-tracer can be improved by porting the code from MATLAB to C or C++ (for example) and using existing software libraries for accelerated computing like OpenCL, NVIDIA's CUDA and embedded GPU computing in order to improve the processing efficiency.

Better Metric for Uncertainty

As explained in Chapter 4, the proposed method for uncertainty was based on an empirical method of approximating the uncertainty using only data available to the algorithm. This might not be the optimal way of defining the uncertainty associated with position estimate from the proposed algorithm. Hence, a better metric based on analytical and mathematical method need to be defined, although this requires a rigorous mathematical model to deal with non-linearity associated with the algorithm.

Extension of Proposed Algorithm for Velocity Estimate and Filtering

The proposed research estimates position using code phase-based correlators. Using correlator information in Doppler domain, velocity can also be estimated along with the estimated position. Furthermore, the estimated position can be smoothed by applying a filter.

All these modifications are assumed to improve the accuracies of the estimated position as well as better uncertainty and reliability of the estimate. However, at system design stage, cost, processing power, and required accuracies and reliability need to be taken into account.

Integrating the Proposed Methodology with Other Sensors

As an extension the proposed methodology can be used to aid the system with external sensors and/or systems such as vehicle sensors, inertial sensors, pedestrian dead-reckoning system, etc. in order to improve accuracy. Such an approach may also allow for smaller search spaces, thus improving algorithm efficiency.

6.4 Final Panoramic View and Impact of the Proposed Research

With the fast urbanization and increasing urban populations (United Nations 2014) improving low cost navigation and positioning solution in urban areas is becoming more important. With the low cost associated with 3DBMs and real-time ray-tracing capabilities (Oktal 2015), the integration of 3DBM with GNSS is a viable solution. By extension, the research presented herein can be part of a low cost, reliable solution for fulfilling the increasing demand of urban navigation. The proposed method can be integrated with other sensors to improve pedestrian navigation on sidewalk in deep urban canyons. Furthermore, since the proposed method is more accurate in across- street compared to along-street, some of its potential applications could be in lane-level autonomous driving and guiding visually impaired person. Hence, 3DBM-integrated GNSS has lots of potential in low cost reliable positioning and navigation in urban canyons, for various current and future applications.

References

- Abd Rabbou M., & El-Rabbany, A. (2015), "Integration of GPS Precise Point Positioning and MEMS-Based INS Using Unscented Particle Filter", *Sensors*, 15(4), 7228-7245. <http://dx.doi.org/10.3390/s150407228>
- Adjrd M., and Paul D Groves (2015), "Enhancing Conventional GNSS Positioning with 3D Mapping without Accurate Prior Knowledge", *Proceeding of ION GNSS 2015*, September 14-18, Tampa, FL, USA
- Aftatah M., Abdelkabir Lahrech, Abdelouahed Abounada & Aziz Soulhi (2016), "GPS/INS/Odometer Data Fusion for Land Vehicle Localization in GPS Denied Environment", *Modern Applied Science*; Vol. 11, No. 1; 2017
- Ahmad K.A.B., Sahnoudi M, Macabiau C, Bourdeau A, Moura G (2013) Reliable GNSS Positioning in Mixed LOS/NLOS Environments Using a 3D model. *Proceedings of the European Navigation Conference*, Vienne, Austria 2013
- Angrisano, A., M. Petovello and G. Pugliano (2012) "Benefits of Combined GPS/GLONASS with Low-Cost MEMS IMUs for Vehicular Urban Navigation," in *Journal of Sensors*, Vol. 12, pp. 5134–5158
- Badia-Sole´ O, Iacobescu-Ioan T (2010) GPS snapshot techniques. Aalborg University, Danish GPS Center
- Bartone, C. and F. Van Graas (1998) "Ranging Airport Pseudolite for Local Area Augmentation", in the *Proceeding of IEEE PLANS*, Palm Springs, CA, April 1998
- Bauer, S., Obst, M., Wanielik, G. (2013), "Probabilistic Integrating of 3D Building Models and GNSS for Reliable Vehicle Localization in Urban Areas—the GAIN Approach," *Proceedings of the Institute of Navigation (ION GNSS+ 2013)*, Nashville, TN, September 2013, pp. 1267-1276.
- Ben-Moshe, B., E. Elkin, H. Levi, and A. Weissman (2011), "Improving Accuracy of GNSS Devices in Urban Canyons", in the *Proceeding of Canadian Conference on Computational Geometry 2011*, August 10-12, Toronto, ON
- Borio, D. (2012) *GNSS Receiver Design*, ENGO 638 Course Notes, Department of Geomatics Engineering, University of Calgary, Canada, Summer 2012
- Borre, K., D. M. Akos, N. Bertelsen, and P. Rinder (2006) *A Software-Defined GPS and Galileo Receiver*, Birkhauser, Boston
- Bourdeau, A. (2012) "Constructive Use of GNSS NLOS-Multipath: Augmenting the Navigation Kalman Filter with a 3D Model of the Environment," in *Proceedings of the 15th International Conference on Information Fusion*, Singapore, IEEE, pp. 2271 – 2276
- Bourdeau, A. (2012a) "Tight Integration of GNSS and 3D City Model for Robust Positioning in Urban Canyons," in *Proceeding of ION GNSS 2012*, September 17-21, Nashville, TN
- Braasch, M. (2001) "Performance comparison of multipath mitigating receiver architectures," in *Proceedings of the IEEE Aerospace Conference*, IEEE, pp. 1309-1315

- Braasch, M., and A.J. Van Dierendonck (1999) "GPS Receiver Architecture and Measurements," *Proceedings of IEEE*, Vol.87, No.1, 1999, 48-64
- Bradbury, J., M. Ziebart, and P.A. Cross (2007), "Code Multipath Modelling in the Urban Environment Using Large Virtual Reality City Models: Determining the Local Environment", *The Journal of Navigation* (2007), Vol. 60, 95–105
- Brenner, C. (2005), "Building reconstruction from images and laser scanning." *International Journal of Applied Earth Observation and Geoinformation*, 6(3–4), 187–198.
- Carrasco-Martos, S., Lopez-Risueno, G., Jiménez-Baños, D., Gill, E.K.A. (2010), "Snapshot Software Receiver for GNSS in Weak Signal Environments: An Innovative Approach for Galileo E5", *ION GNSS 2010*, Sep. 21-24, Portland, OR, USA
- Chan, B., and M.G. Petovello (2011), "Collaborative Vector Tracking of GNSS Signals with Ultra-Wideband Augmentation in Degraded Signal Environment", *ION ITM 2011*, Jan 24-26, San Diego, CA
- Cossaboom, M., J. Georgy, T.B. Karamat, and A. Noureldin (2012), "Augmented Kalman Filter and Map Matching for 3D RISS/GPS Integration for Land Vehicles," in *International Journal of Navigation and Observation*, Vol. 2012, pp. 1–16
- Dierendonck, A. V. , Pat Fenton and Tom Ford (1992) "Theory and performance of narrow correlator spacing in a GPS receiver," in *Navigation, Journal of the Institute of Navigation*, Vol. 39, Issue 3, pp. 265–283
- Dragunas, K. and K. Borre (2011) "Multipath Mitigation Based on Deconvolution," *Journal of Global Positioning Systems*, vol 10, no 1, October, pp. 79-88
- Ebner, A. (2008), "On the attainable accuracy of multisystem GNSS positioning in high-multipath urban", Master thesis, TU Graz University, Austria, 2008
- Fenton, P. C. and J. Jones (2005) "The Theory and Performance of NovAtel Inc.'s Vision Correlator", *ION/GNSS 2005*, Long Beach, CA
- Fenton, P., B. Falkenberg, T. Ford, K. Ng, and A. J. Van Dierendonck (1991) "NovAtel's GPS Receiver – the High Performance OEM Sensor of the Future," in *Proceedings of ION GPS-91*, Albuquerque, NM, September 1991, pp.49–58
- Fernandez-Hernandez I and Borre K (2016) Snapshot Positioning without Initial Information. *GPS Solutions*, March 2016, DOI 10.1007/s10291-016-0530-4, pp 1-12
- Filippov, V., D. Tatarnicov, J. Ashjaee, A. Astakhov, I. Sutiagin (1998) "The First Dual-Depth Dual-Frequency Choke Ring", in the *Proceeding of ION/GPS 1998*
- Frere D, Vandekerckhove J, Moon T, Van Gool L (1998) Automatic Modelling and 3D Reconstruction of Urban 376 Buildings from Aerial Imagery. *IEEE International Geoscience and Remote Sensing Symposium 377 Proceedings*, pp 2593-2596
- Garin, L. and J. M. Rousseau (1997) "Enhanced strobe correlator multipath rejection for code & carrier," in *Proceedings of the Institute of Navigation (ION GPS '97)*, 16-19 September, Kansas City MO, USA, pp. 559–568.

- Gao, J., M. Petovello, and M. Elizabeth Cannon (2008) "Integration of Steering Angle Sensor with GPS and MEMS IMU for Vehicular Positioning," in *Journal of Intelligent Transportation Systems*, Vol. 12, Issue 4, pp. 159–167
- Godha, S., M. Petovello, and G. Lachapelle (2005), "Performance Analysis of MEMS IMU/HSGPS/Magnetic Sensor Integrated System in Urban Canyons", *Proceeding of ION ITM 2005*, September 13-16, Long Beach, CA
- Groves, P D, Z Jiang, M Rudi, and P Strode (2013), "A Portfolio Approach to NLOS and Multipath Mitigation in Dense Urban Areas", *Proceeding of ION GNSS 2013*, September 16-20, Nashville, TN
- Groves, P.D., Z. Jiang, L. Wang, and M K Ziebart (2012), "Intelligent Urban Positioning Using Multi-Constellation GNSS with 3D Mapping and NLOS Signal Detection", in the *Proceeding of ION ITM 2012*, September 17-21, Nashville, TN
- Groves, P.D. (2011), "Shadow Matching: A New GNSS Positioning Technique for Urban Canyons", *Journal of Navigation*, Vol. 64, Issue 03
- Groves, P.D., Z. Jiang, B. Skelton, Paul Cross, L. Lau, Y. Adane, and I. Kale (2010), "Novel multipath Mitigation Methods using a Dual-polarization Antenna", *Proceeding of ION ITM 2010*, September 21-24, Portland, OR
- Groves, P.D., Christopher J Mather, Alex A Macaulay (2007), "Demonstration of Non-coherent Deep INS/GPS Integration for Optimised Signal-to-noise Performance", *Proceeding of ION ITM 2007*, September 25-28, Fort Worth, TX
- Gu, Yanlei, Hsu, Li-Ta, Wada, Yutaro, Kamijo, Shunsuke (2015), "Integration of 3D Map based GPS Positioning and On-Board Sensors for Vehicle Self-Localization in Urban Canyon," *Proceedings of the ION 2015 Pacific PNT Meeting*, Honolulu, Hawaii, April 2015, pp. 565-572
- Habib, A., E. Kim, and C. Kim (2007). New methodologies for true ortho-photo generation, *Photogrammetric Engineering and Remote Sensing*, 73(1): pp.25-36, 2007
- He Z and Petovello M G (2014) Joint Detection and Estimation of Weak GNSS Signals with Application to Coarse Time Navigation. *Proceeding of ION GNSS 2014*, September 8-12, Tampa, FL, USA
- He Z, and Petovello M G (2013) Multipath Mitigation by Voting Channel Impulse Response in Navigation Domain with High-Sensitivity GNSS. *Proceeding of ION GNSS 2013*, September 16-20, Nashville, TN, pp 2749-2758
- Hsu Li-Ta, Gu Y., Kamijo S., (2016), " 3D building model-based pedestrian positioning method using GPS/GLONASS/QZSS and its reliability calculation," *GPS Solution*, Vol. 20, Issue-3, July 2016, pp 413-428
- Hsu, LT., Y. Gu and S. Kamijo (2016 a), "Autonomous driving positioning using building model and DGNSS" *ENC 2016*, Helsinki, Finland, 30 May-2 June 2016, IEEE.

- Iqbal, U., T.B. Karamat, A.F. Okou and A. Noureldin (2009), "Experimental Results on an Integrated GPS and Multisensor System for Land Vehicle Positioning," in *International Journal of Navigation and Observation*, Vol. 2009, pp. 1–18
- Irsigler, M., and B. Eissfeller (2003), "Comparison of multipath mitigation techniques with consideration of future signal structures," in *Proceedings of the ION/GNSS*, September 2003, Portland, OR
- Jekeli, C. (2001). Inertial navigation systems with geodetic applications. Walter de Gruyter: Berlin, Germany.
- Jensen, J. R., D. Cowen, T. Kammerer, and X. Huang (1994), GPS and softcopy photogrammetry for large-scale digital elevation model creation and orthophoto mapping for urban applications, proceedings ASPRS, Washington, Aug. 26-29, pp. 169-178, 1994.
- Kaplan, E. (2006), "Introduction", Kaplan E. and Hegarty C., eds., *Understanding GPS: Principles and Applications*, 2nd edition, Chapter 1, Artech House Inc., MA, USA
- Knight J., Greg Turetzky, Charles Norman and Dennis Hilgenberg (1998), "SiRF's Low Power Receiver Advances", in Proceedings of ION GPS 1998.
- Kumar, R., and M Ahmad (2004), "Comparison of Multipath Error Elimination Techniques under Relatively Severe Multipath Environments", in *Proceeding of ION ITM*, San Diego, CA, 26-28 January 2004
- Kwak E., (2013), "Automatic 3D Building Model Generation by Integrating LiDAR and Aerial Images Using a Hybrid Approach", PhD thesis, Department of Geomatics Engineering, January 2013
- Lannelongue, S. and P. Pablos (1998), "Fast acquisition techniques for GPS receivers", in Proceedings of the 54th Annual Meeting of The Institute of Navigation, pp.261–269
- Lau, L., and P. Cross (2007), "Development and testing of a new ray-tracing approach to GNSS carrier-phase multipath modelling", *Journal of Geodesy*, Nov. 2007, Vol. 81, No. 11, PP-713-732
- Lee Y-W, Suh Y-C, Shibasaki R (2008), "A simulation system for GNSS multipath mitigation using spatial statistical methods", *Computers and Geosciences*, vol. 34, issue 11, pages: 1597–1609. doi:10.1016/j.cageo.2008.01.004
- Lehner, A., and Steingass (2008), "Differences in Multipath Propagation between Urban and Suburban Environments", *Proceedings of the 21st International Technical Meeting of the Satellite Division of The Institute of Navigation*, September 16 - 19, 2008, Savannah, GA
- Lentmaier, M., B. Krach, and P. Robertson (2008) "Bayesian Time Delay Estimation of GNSS Signals in Dynamic Multipath Environments", *International Journal of Navigation and Observation*, Vol. 2008, Article ID 372651
- Li, T., M.G. Petovello, G. Lachapelle and C. Basnayake (2011) "Real-time ultra-tight integration of GPS L1/L2C and Vehicle Sensors," in Proceedings of ION ITM 2011, 24-26 January, San Diego CA 2011

- Lin, Z., J. Wang and J. Gao (2016) "An Enhanced GPS/INS Integrated Navigation System With GPS Observation Expansion," *The Journal of Navigation*, 2016, No-69, The Royal Institute of Navigation, pp.1041-1060, doi:10.1017/S0373463315001083
- Lin, T., Cillian O'Driscoll and Gérard Lachapelle (2011) "Development of a Context-Aware Vector-Based High-Sensitivity GNSS Software Receiver," in *Proceedings of IEEE/ION PLANS 2006*, 25-27 April, San Diego CA, pp.291-299
- Manandhar, D. and R. Shibasaki (2004) "Possibility Analysis of Polarization Diversity Scheme for Multipath Mitigation in GPS Receivers," *The 2004 International Symposium on GNSS/GPS Sydney 2004*, 6-8 December, Sydney, Australia
- Mcgraw, G. A., Braasch, M. S. (1999) "GNSS multipath mitigation using gated and high resolution correlator concepts", in *Proceedings of the National Technical Meeting of the Satellite Division of the Institute of Navigation*. San Diego (USA), Jan 1999.
- Mezentsev, O., Y. Lu, G. Lachapelle, and R. Klukas (2002), "Vehicular Navigation in Urban Canyons Using a High Sensitivity GPS Receiver Augmented with a Low Cost Rate Gyro", *ION/GPS 2002*, Sep. 24-27, Portland, OR
- Misra, P., and P. Enge (2011) *Global Positioning System: Signals, Measurements and Performance*, Ganga-Jamuna Press, Licoln, Massachusetts
- Miura S, Hisaka S, Kamijo S (2013) GPS multipath detection and rectification using 3D maps. 16th International IEEE conference on intelligent transportation systems (ITSC), 2013, October 6–9, pp 1528–1534. doi:10.1109/ITSC.2013.6728447
- Moelker, D. J. (1997) "Multiple Antennas for Advanced GNSS Multipath Mitigation and Multipath Direction Finding", in the *Proceeding of ION/GPS 97*, September, Kansas City
- Morrison, A. (2010), *GNSS Signal Tracking Methods Under Ionospheric Scintillation*, PhD Thesis, Dept. Of Geomatics Engineering, University of Calgary, August 2010
- Muthuraman, K., J. Brown and M. Chansarkar (2011) "Coarse time navigation: Equivalence of algorithms and reliability of time estimates." *IET radar, sonar & navigation*, vol. 5, no. 6, pp. 657–665
- Noureldin, A. (2013), *Inertial Navigation and INS/GPS Integration* ENGO 623 Course Notes, Department of Geomatics Engineering, University of Calgary, Canada, Spring 2013
- Noureldin, A., T.B. Karamat, J. Georgy (2013), *Fundamentals of Inertial Navigation, Satellite-based Positioning and their Integration*, Springer, DOI: 10.1007/978-3-642-30466-8
- Noureldin, A., T.B. Karamat, M.D. Eberts and A. El-Shafie (2009), "Performance Enhancement of MEMS-Based INS/GPS Integration for Low-Cost Navigation Applications," in *IEEE Transactions on Vehicular Technology*, Vol. 58, Issue 3, pp. 1077–1096

- Obst, M., S. Bauer, and G. Wanielik (2012) "Urban Multipath Detection and Mitigation with Dynamic 3D Maps for Reliable Land Vehicle Localization," in *Proceedings of the Position Location and Navigation Symposium (PLANS)*, IEEE/ION, Myrtle Beach, SC, IEEE/ION, pp. 685-691
- O'Driscoll, C., G. Lachapelle, and M.E. Tamazin (2010), "Investigation of the Benefits of Combined GPS/GLONASS Receivers in Urban Environments", *Royal Inst. Of Nav. NAVIO Conference*, London Nov 30- Dec 2, 2010
- Oktal (2015), Oktal-Synthetic Environment (SE-NAV), "Simulating, Assessing and Improving GNSS Reception in Constrained Environments", <http://www.oktal-se.fr/website/wp-content/uploads/2015/09/SE-NAV.pdf>
- Pany, T., (2010) *Navigation Signal Processing for GNSS Software Receivers*, Artech House, Boston|London, 685 Canton Street, Norwood, MA 02062
- Parkinson, B., and J. Spilker (1996) *Fundamentals of Signal Tracking Theory in Global Positioning System: Theory and Applications*, AIAA
- Petovello, M., and Z. He (2016) "Skyline Positioning in Urban Areas Using a Low-Cost Infrared Camera," ENC 2016, Helsinki, Finland, 30 May-2 June 2016, IEEE
- Petovello, M., and J.T. Curran (2013) "Investigation of Doppler Measurements for Static Indoor Positioning", Proceedings of ION Pacific PNT 2013 Conference, April 22-25, Honolulu, HI, 12 pages
- Petovello, M.G., C. O'Driscoll, G. Lachapelle, D. Borio and H. Murtaza (2009) "Architecture and Benefits of an Advanced GNSS Software Receiver". *Journal of Global Positioning Systems*, 7, 2, pp. 156-168.
- Petovello, M., C. O'Driscoll and G. Lachapelle (2008) "Carrier Phase Tracking of Weak Signals Using Different Receiver Architectures," Proceedings of ION NTM08 (San Diego, 28-30 Jan, Session A4). The Institute of Navigation, 11 pages
- Petovello, M., and G. Lachapelle (2006) "Comparison of Vector-Based Software Receiver Implementations with Application to Ultra-Tight GPS/INS Integration," in Proceedings of ION GNSS 2006, 26-29 Sept., Fort Worth TX, pp.2977-2989, U.S. Institute of Navigation, Fairfax VA.
- Petovello, M. G. (2003) *Real-Time Integration of a Tactical-Grade IMU and GPS for High-Accuracy Positioning and Navigation*, PhD thesis, Department of Geomatics Engineering, the University of Calgary, Canada
- Peyraud, S., David B'étaille, Stéphane Renault, Miguel Ortiz, Florian Mougel, Dominique Meizel and Francois Peyret (2013), "About Non-Line-Of-Sight Satellite Detection and Exclusion in a 3D Map-Aided Localization Algorithm", *Sensors* 2013, 13, 829-847, doi:10.3390/s130100829
- Pinana-Diaz C, Toledo-Moreo R, Betaille D, Gomez-Skarmeta AF (2011), "GPS multipath detection and exclusion with elevation-enhanced maps", 14th International IEEE conference intelligent transportation systems (ITSC), October 5-7, pp 19-24. doi:10.1109/ITSC.2011.6083042

- Pratt, A. R. (2004), "Performance of Multi-Path Mitigation Techniques at Low Signal to Noise Ratios," *Proc. ION GNSS 2004*, Long Beach, CA, September 2004, pp. 43–53.
- Qian Y, Cui X, Lu M, Feng Z (2008) Snapshot Positioning for Unaided GPS Software Receivers. *Proceeding of ION GNSS 2008*, September 16-19, Savannah, GA, pp. 2343-2350
- Ramalingam S, Bouaziz S, Sturm P, Brand M (2010), SKYLINE2GPS: Localization in urban canyons using omniskyines. *Intelligent Robots and Systems (IROS), 2010 IEEE/RSJ International Conference on. IEEE, 2010*, pp. 3816–3823.
- Ramalingam S, Bouaziz S, Sturm P, Brand M (2009) Geolocalization using skylines from omni-images. *Computer Vision Workshops (ICCV Workshops), 2009 IEEE 12th International Conference on IEEE, 2009*, pp. 23–30.
- Ray, J.K. (2000), *Mitigation of GPS Code and Carrier Phase Multipath Effects Using a Multi-Antenna System*, PhD Thesis, Dept. Of Geomatics Engineering, University of Calgary, March 2000
- Ranzinger, M., and G. Gleixner (1997), GIS Datasets For 3D Urban Planning, *Computers, Environment, and Urban Systems*, 21(2): pp. 159-173, 1997.
- Sahmoudi, M. and M.G. Amin (2008) "Fast iterative maximum-likelihood algorithm (FIMLA) for multipath mitigation in next generation of GNSS receivers," in *IEEE Trans. On Wireless Com*, Vol. 7, Issue 11, pp. 4362–4374
- Scherzinger, Bruno (2015), "Quasi-tightly Coupled GNSS-INS Integration", *NAVIGATION, Journal of The Institute of Navigation*, Vol. 62, No. 4, Winter 2015, pp. 253-264.
- Sharp Yu, Guo Y (2009) Peak and leading edge detection for time-of-arrival estimation in band-limited positioning systems. *IET Communications*, vol. 3, no. 10, Oct. 2009, pp 1616–1627
- Sleewaegen, J.M., and F. Boon (2001) "Mitigating short-delay multipath: A promising new technique", pp. 204–213, in *Proc. ION GPS 2001*, Salt Lake City, UT, USA, 2001.
- Sokhandan, N. (2013), *GNSS Multipath Mitigation Using Channel Parameter Estimation Techniques*, PhD Thesis, Dept. Of Geomatics Engineering, University of Calgary, November 2013
- Sokhandan, N. (2013a), "A Novel Multipath Estimation and Tracking Algorithm for Urban GNSS Navigation Applications," in *Proceeding of ION GNSS 2013*, September 16-20, Nashville, TN
- Soloviev, A., C. Toth, D. Grejner-Brzezinska (2011), "Performance of Deeply Integrated GPS/INS in Dense Forestry Areas", in *proceeding of ION/GNSS 2011*, September 20-23, Portland, Oregon
- Soloviev, A., and F. V. Graas (2009) "Use of deeply integrated GPS/INS architecture and laser scanners for the identification of multipath reflections in urban environments," *IEEE Journal of Selected Topics in Signal Processing*, vol. 3, no. 5, pp. 786-797, Oct. 2009.

- Soloviev, A., D. Bruckner, F. van Graas and L. Marti (2007) “Assessment of GPS Signal Quality in Urban Environments Using Deeply Integrated GPS/IMU,” in Proceedings of ION NTM 2007, 22-24 January, San Diego, CA, pp. 815-828, U.S. Institute of Navigation, Fairfax VA
- Stone, J., and M. Chansarkar (2004), “Anti-multipath triangulation (AMT) for positioning in dense urban environments”, in *Proc. ION GNSS*, pp. 1165–1168, Long Beach, CA, Sep. 21-24, 2004
- Suzuki, T., (2016), “Integration of GNSS Positioning and 3D Map using Particle Filter ”, in *Proceedings of the ION GNSS+ Sep 12-16, 2016*, Portland, OR, USA, 2016
- Suzuki, T., and N. Kubo (2013), “Correcting GNSS Multipath Errors Using a 3D Surface Model and Particle Filter”, in *Proceedings of the ION GNSS*, Nashville, Tennessee, 2013
- Suzuki, T., and N. Kubo (2012), “GNSS Positioning with Multipath Simulation using 3D Surface Model in Urban Canyon”, in *Proceedings of the ION GNSS*, Nashville, Tennessee, 2012
- Townsend, B. and Fenton, P. (1994), “A Practical Approach to the Reduction of Pseudorange Multipath Errors in a L1 GPS Receiver,” in Proceedings of the 7th International Technical Meeting of the Satellite Division of The Institute of Navigation (ION GPS-94), Salt Lake City, UT, pp. 143–148.
- Uijt de Haag M (1999) An investigation into the application of block processing techniques for the Global Positioning System. Ph. D. Thesis, Department of Electrical Engineering, The Ohio University
- United Nations (2014), Department of Economic and Social Affairs, Population Division (2014), *World Urbanization Prospects: The 2014 Revision, Highlights (ST/ESA/SER.A/352)*.
- Van Dierendonck, A. J., P. Fenton, and T. Ford (1992) “Theory and Performance of Narrow Correlator Spacing in a GPS Receiver”, *Navigation: Journal of The Institute of Navigation*, Vol.39, No.3, Fall 1992
- Van Diggelen, F., (2009) *A-GPS: Assisted GPS, GNSS and SBAS*, Artech House, Boston|London, 685 Canton Street, Norwood, MA 02062
- Van Graas, F, A. Soloviev, M. Uijt de Haag, and S. Gunawardena (2009), Closed-Loop Sequential Signal Processing and Open-loop Batch Processing Approaches for GNSS Receiver Design, *IEEE Journal of Selected Topics in Signal Processing*, Vol. 3, No. 4, August 2009
- Van Nee, R.D.J. (1995) *Multipath and Multi-Transmitter Interference in Spread-Spectrum Communication and Navigation Systems*, PhD Thesis, Faculty of Electrical Engineering, Mathematics and Computer Science, TU Delft,1995
- Van Nee, R. D. J., J. Sierveld, P. C. Fenton, and B. R. Townsend (1994) “The Multipath Estimating Delay Lock Loop: Approaching Theoretical Accuracy Limits”, *IEEE Position Location and Navigation Symposium*, 1994

- Van Nee, R. D. J. (1992) "The Multipath Estimating Delay Lock Loop", Proceedings of the IEEE 2nd Int. Symp. on Spread Spectrum Techniques & Applications, Yokohama, 1992
- Wang, L., P D Groves, and M.K. Ziebart, (2015), Smartphone Shadow Matching for Better Cross-street GNSS Positioning in Urban Environments. *The Journal of Navigation*, Vol. 68, 411-433
- Wang, L., P D Groves, and M.K. Ziebart, (2012), "Multi-Constellation GNSS Performance Evaluation for Urban Canyons Using Large Virtual Reality City Models", *The Journal of Navigation*, Vol. 65, 459-476
- Ward, P. W. and Christopher J. Hegarty, (2006) "Satellite Signal Acquisition, Tracking, and data demodulation", Chapter 5, *Understanding GPS: Principles and Applications*, Edited by Elliott D. Kaplan and Christopher J. Hegarty, 2nd edition, Artech House, MA, USA
- Ward, P. W., J. W. Betz, and Christopher J. Hegarty, (2006) "Interference, Multipath, and Scintillation", Chapter 6, *Understanding GPS: Principles and Applications*, Edited by Elliott D. Kaplan and Christopher J. Hegarty, second edition, Artech House, MA, USA
- Ward, P. W., J. W. Betz, and Christopher J. Hegarty, (2006 a) "GPS Satellite Signal characteristics", Chapter 4, *Understanding GPS: Principles and Applications*, Edited by Elliott D. Kaplan and Christopher J. Hegarty, second edition, Artech House, MA, USA
- Watson, J. (2005) *High-Sensitivity GPS L1 Signal Analysis for Indoor Channel Modeling*, Master thesis, the University of Calgary, Canada
- Weill, L. R. (1995) "Achieving Theoretical Accuracy Limits for Pseudorangeing in the Presence of Multipath", in the Proceeding of ION/GPS, September, Palm Springs, CA
- Wendel, J., C. Schlaile, and G. F Trommer (2004), "Direct Kalman Filtering of GPS/INS for Aerospace Applications", Univ of Karlsruhe, Germany
- Xie P, Petovello M G (2015), "Measuring GNSS Multipath Distributions in Urban Canyon Environments", *IEEE Transactions on Instrumentation and Measurement*, Vol. 64, No-2, February 2015, pp 366-377
- Xie, P. (2013) *Improving High Sensitivity Receiver Performance in multipath Environment for Vehicular Applications*, PhD Thesis, Department Of Geomatics Engineering, University of Calgary, September 2013
- Yang, Y. (2008) *Tightly Coupled MEMS INS/GPS Integration with INS Aided Receiver Tracking Loops*, PhD Thesis, Department Of Geomatics Engineering, University of Calgary, May 2008
- Yao Z., M. Lu and Z. Feng, (2010), " Spreading code phase measurement technique for snapshot GNSS receiver", *IEEE Transaction on Consumer Electronics*, Vol. 56, No. 3, August 2010, pp. 1275-1282, DOI: 10.1109/TCE.2010.5606259
- Yozevitch, Roi, Moshe, Boaz Ben (2015), "A Robust Shadow Matching Algorithm for GNSS Positioning", *NAVIGATION, Journal of The Institute of Navigation*, Vol. 62, No. 2, Summer 2015, pp. 95-109.

Appendix: A

Computation of Observation Matrix and Measurement Noise Covariance Matrix for the Least-Squares

This Appendix shows the observation matrix and noise covariance matrix for different path models shown in Table 3.1. Using states and observation models from Table 3.1, the observation matrix for different path model can be derived as below.

In following equations of observation matrix (equations (A.4) to (A.18)), we have used the following notations:

$$R'(\tau_k) = \frac{\partial R(\tau_k)}{\partial \tau_k} \quad (\text{A.1})$$

where $R(\tau_k)$ is the autocorrelation function defined as (Sharp 2009):

$$R(\tau_k) = A_c \times \left(1 - \sqrt{(\tau_{nco} - \tau_k)^2 + \sigma^2} \right) \quad (\text{A.2})$$

where

A_c : is a constant obtained from simulations; and

σ : corresponds to bandwidth loss;

A_c and σ values were obtained after a LSQ fit of the simulated correlator (using Spirent simulator) with a mathematical correlator model (equation A.2).

where

$$R(\tau_k) = R(\tau_1 + \Delta\tau_k); k > 1 \quad (\text{A.3})$$

One-path signal model

For one-path signal model, since there are only two states to be determined (Table 3.1), the corresponding partial derivatives (for linearization) for the observation matrix are shown in equations (A.4) and (A.5).

$$\frac{\partial Z}{\partial A_1} = (2 \times A_1 \times R^2(\tau_1)) \quad (\text{A.4})$$

$$\frac{\partial Z}{\partial \tau_1} = (2 \times A_1^2 \times R(\tau_1) \times R'(\tau_1)) \quad (\text{A.5})$$

Two-path signal model

For two-path signal model, there are five states to be determined (Table 3.1), the corresponding partial derivatives for the observation matrix is shown in to equations (A.6) to (A.10)

$$\frac{\partial Z}{\partial A_1} = (2 \times A_1 \times R^2(\tau_1)) + (2 \times A_2 \times R(\tau_1) \times R(\tau_2) \times \cos(\delta_{12})) \quad (\text{A.6})$$

$$\begin{aligned} \frac{\partial Z}{\partial \tau_1} = & (2 \times A_1^2 \times R(\tau_1) \times R'(\tau_1)) + \\ & \left(2 \times A_1 \times A_2 \times \cos(\delta_{12}) \times \left(\begin{array}{l} R'(\tau_1) \times R(\tau_2) \\ + R'(\tau_2) \times R(\tau_1) \end{array} \right) \right) + \\ & (2 \times A_2^2 \times R(\tau_2) \times R'(\tau_2)) \end{aligned} \quad (\text{A.7})$$

$$\frac{\partial Z}{\partial A_2} = (2 \times A_2 \times R^2(\tau_2)) + (2 \times A_1 \times R(\tau_1) \times R(\tau_2) \times \cos(\delta_{12})) \quad (\text{A.8})$$

$$\begin{aligned} \frac{\partial Z}{\partial \Delta \tau_2} = & (2 \times A_2^2 \times R(\tau_2) \times R'(\tau_2)) + \\ & (2 \times A_1 \times A_2 \times R(\tau_1) \times R'(\tau_2) \times \cos(\delta_{12})) \end{aligned} \quad (\text{A.9})$$

$$\frac{\partial Z}{\partial \delta_{12}} = -(2 \times A_1 \times A_2 \times R(\tau_1) \times R(\tau_2) \times \sin(\delta_{12})) \quad (\text{A.10})$$

Three-path signal model

For three-path signal model, there are eight states to be determined (Table 3.1), the corresponding partial derivatives for the observation matrix is shown in equations (A.11) to (A.19).

$$\begin{aligned} \frac{\partial Z}{\partial A_1} = & (2 \times A_1 \times R^2(\tau_1)) + (2 \times A_2 \times R(\tau_1) \times R(\tau_2) \times \cos(\delta_{12})) + \\ & (2 \times A_3 \times R(\tau_1) \times R(\tau_3) \times \cos(\delta_{13})) \end{aligned} \quad (\text{A.11})$$

$$\begin{aligned} \frac{\partial Z}{\partial \tau_1} = & (2 \times A_1^2 \times R(\tau_1) \times R'(\tau_1)) + (2 \times A_2^2 \times R(\tau_2) \times R'(\tau_2)) \\ & + (2 \times A_3^2 \times R(\tau_3) \times R'(\tau_3)) \\ & + (2 \times A_1 \times A_2 \times \cos(\delta_{12}) \times (R'(\tau_1) \times R(\tau_2) + R'(\tau_2) \times R(\tau_1))) \\ & + (2 \times A_2 \times A_3 \times \cos(\delta_{23}) \times (R'(\tau_2) \times R(\tau_3) + R'(\tau_3) \times R(\tau_2))) \\ & + (2 \times A_1 \times A_3 \times \cos(\delta_{13}) \times (R'(\tau_1) \times R(\tau_3) + R'(\tau_3) \times R(\tau_1))) \end{aligned} \quad (\text{A.12})$$

$$\frac{\partial Z}{\partial \delta_{12}} = -(2 \times A_1 \times A_2 \times R(\tau_1) \times R(\tau_2) \times \sin(\delta_{12})) \quad (\text{A.13})$$

$$\begin{aligned} \frac{\partial Z}{\partial A_2} = & (2 \times A_2 \times R^2(\tau_2)) + (2 \times A_1 \times R(\tau_1) \times R(\tau_2) \times \cos(\delta_{12})) + \\ & (2 \times A_3 \times R(\tau_2) \times R(\tau_3) \times \cos(\delta_{23})) \end{aligned} \quad (\text{A.14})$$

$$\begin{aligned} \frac{\partial Z}{\partial \Delta \tau_2} = & (2 \times A_2^2 \times R(\tau_2) \times R'(\tau_2)) + \\ & (2 \times A_1 \times A_2 \times R(\tau_1) \times R'(\tau_2) \times \cos(\delta_{12})) + \\ & (2 \times A_2 \times A_3 \times R'(\tau_2) \times R(\tau_3) \times \cos(\delta_{12})) \end{aligned} \quad (\text{A.15})$$

$$\frac{\partial Z}{\partial \delta_{23}} = -(2 \times A_2 \times A_3 \times R(\tau_2) \times R(\tau_3) \times \sin(\delta_{23})) \quad (\text{A.16})$$

$$\begin{aligned} \frac{\partial Z}{\partial A_3} = & (2 \times A_3 \times R^2(\tau_3)) + (2 \times A_2 \times R(\tau_2) \times R(\tau_3) \times \cos(\delta_{23})) + \\ & (2 \times A_1 \times R(\tau_1) \times R(\tau_3) \times \cos(\delta_{13})) \end{aligned} \quad (\text{A.17})$$

$$\begin{aligned} \frac{\partial Z}{\partial \Delta \tau_3} = & (2 \times A_3^2 \times R(\tau_3) \times R'(\tau_3)) + \\ & (2 \times A_2 \times A_3 \times R(\tau_2) \times R'(\tau_3) \times \cos(\delta_{23})) + \\ & (2 \times A_1 \times A_3 \times R(\tau_1) \times R'(\tau_3) \times \cos(\delta_{13})) \end{aligned} \quad (\text{A.18})$$

and

$$\delta_{13} = \delta_{12} + \delta_{23} \quad (\text{A.19})$$

Measurement Noise Covariance Matrix (W)

The measurement noise covariance matrix (W) matrix is a fully populated matrix, where off-diagonal elements have values according to the ranging code's auto-correlation function.

Assuming n observations (correlator outputs) for a given satellite, the covariance matrix can be written as shown in equation (A.20).

$$W = \sigma^2 \begin{bmatrix} 1 & R(\tau_2) & \dots & R(\tau_{n-1}) & R(\tau_n) \\ R(\tau_1) & 1 & \dots & R(\tau_{n-1}) & R(\tau_n) \\ \dots & \dots & \dots & \dots & \dots \\ R(\tau_1) & R(\tau_2) & \dots & 1 & R(\tau_n) \\ R(\tau_1) & R(\tau_2) & \dots & R(\tau_{n-1}) & 1 \end{bmatrix} \quad (\text{A.20})$$

where

$R(\tau_i)$: is the value of the auto-correlation function of the difference in code phase between two correlators corresponding to the i^{th} correlator; and

σ : is standard deviation of the measurement post correlation, as defined in Chapter 6 of Van Diggelen (2009).

Appendix: B

Analysis of accuracy of 3D building model from 3D CAD browser

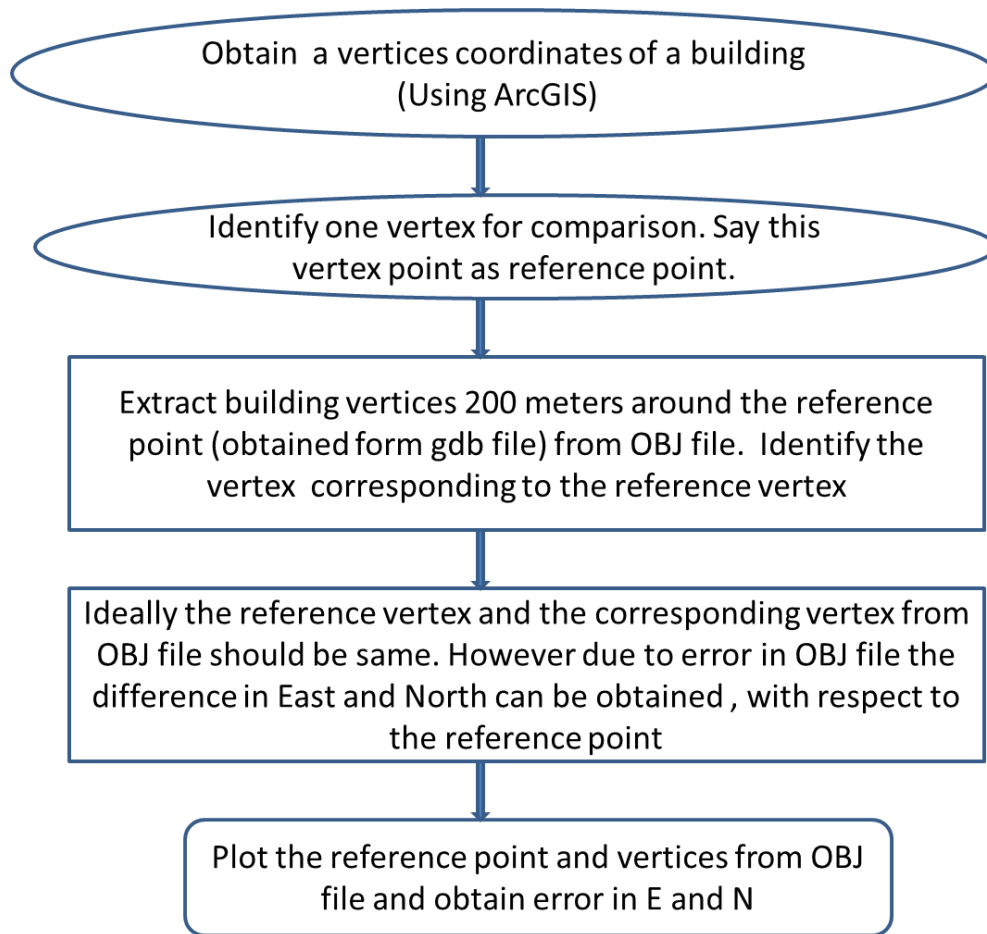
This appendix provides a brief analysis of accuracy of the 3D Building Model (3DBM) obtained from 3D CAD Browser, Hampshire, UK (<http://www.3dcadbrowser.com>). The quoted accuracy of the model by the manufacture was 1 to 3 metres. In order to validate this 3DBM's accuracy, another 3DBM was obtained from the City of Calgary, with quoted accuracy of 15 cm.

The file format of the 3DBM from 3D CAD Browser was in Object (.obj) file format, which is a native format of any 3DBM. The vertices coordinate were obtained in Geodetic coordinate system (Latitude, Longitude and height). The file format of the 3DBM from City of Calgary was provided in geodatabase format (.gdb). Geodatabase is format defined by ESRI Company. The vertices coordinates in gdb file is in 3TM coordinate system. In order to obtain the vertices coordinates in geodetic coordinate system, ArcGIS was used.

It was also observed that there were some features/vertices missing in the OBJ file. For missing vertices (in OBJ file) the analysis is done separately by calculating the error occurred in model due to missing feature/vertices. This error should not be confused with accuracy analysis, since the accuracy analysis is done only for those vertices which are common in OBJ and GDB files.

Algorithm for 3D model's accuracy analysis

The 3D model obtained from 'The City of Calgary' in .gdb format was assumed as the reference to obtain the accuracy of 3D model obtained from 'The 3D CAD Browser' company (<http://www.3dcadbrowser.com>) in .obj file format. The process is termed here as validation process. Below is a flow chart to depict the validation process.



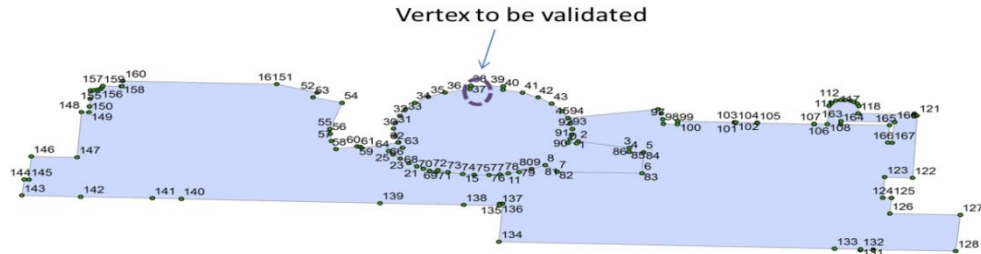
Flow chart for validation

For validation 3 different buildings were selected in E-W along 9th Avenue and in N-S along 6th street. Below is analysis for each building, separately.

Calgary Tower

Below is a jpg image of Calgary tower obtained from gdb file using ArcGIS. The numbers indicate the vertices ID. Each ID is associated with Latitude, Longitude in a file exported using ArcGIS.

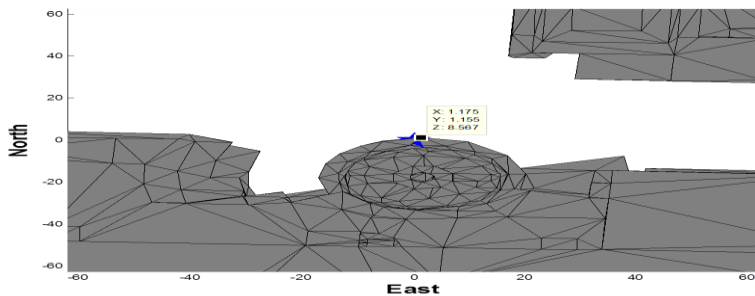
Validation of vertex in N direction



Calgary Tower’s vertices from gdb file. Vertex ID 37 in N direction is used as reference in this case for validation of corresponding vertex from OBJ file

Lat Long for vertex ID 37

Lat	Long	Vertex ID
51.04447	-114.063151	37

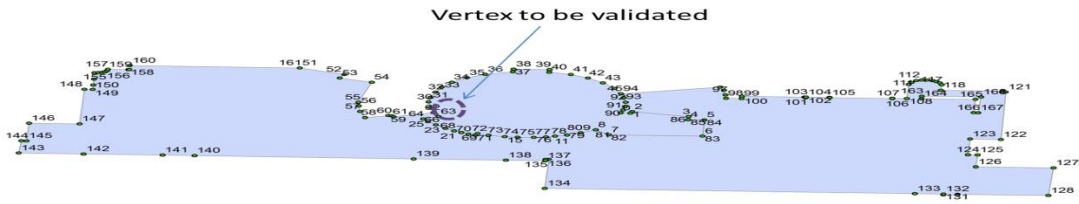


Calgary Tower’s vertices obtained from OBJ file. The blue star indicates the reference point (vertex ID 37 from gdb file). The marker indicates the corresponding point in OBJ file for vertex ID 37 (of gdb file).

Error for a vertex in N direction

Error in E (m)	Error in N (m)
1.2	1.2

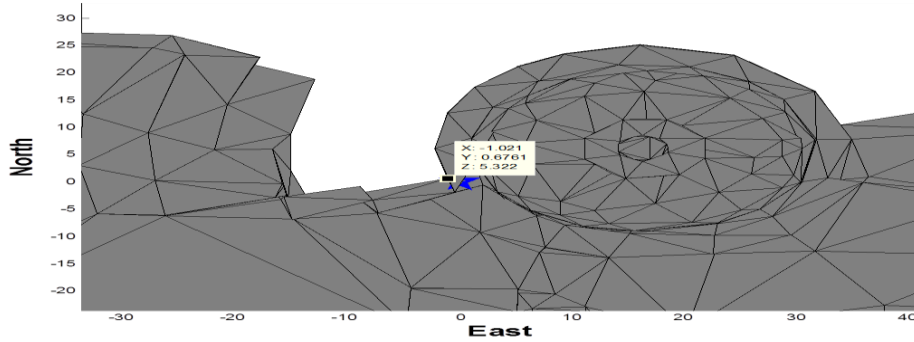
Validation of vertex in SW direction



Calgary Tower’s vertices from gdb file. Vertex ID 63 in SW direction is used as reference in this case for validation of corresponding vertex from OBJ file

Lat Long for vertex ID 63

Lat	Long	Vertex ID
51.044234	-114.06335	63

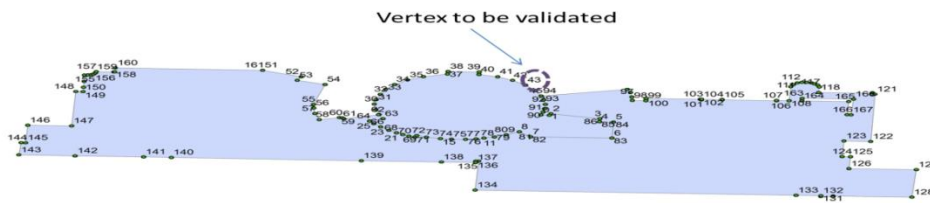


Calgary Tower's vertices obtained from OBJ file. The blue star indicates the reference point (vertex ID 63 from gdb file). The marker indicates the corresponding point in OBJ file for vertex ID 63 (of gdb file).

Error for a vertex in SW direction

Error in E (m)	Error in N (m)
1.0	0.7

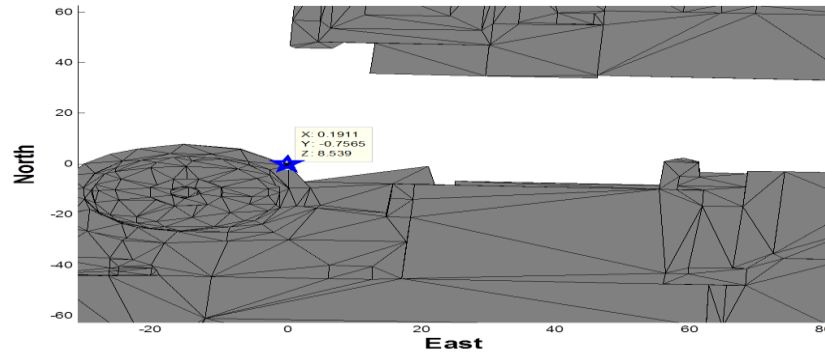
Validation of vertex in NE direction



Calgary Tower's vertices from gdb file. Vertex ID 43 in NE direction is used as reference in this case for validation of corresponding vertex from OBJ file

Lat Long for vertex ID 43

Lat	Long	Vertex ID
51.044411	-114.062913	43



Calgary Tower's vertices obtained from OBJ file. The blue star indicates the reference point (vertex ID 43 from gdb file). The marker indicates the corresponding point in OBJ file for vertex ID 43 (of gdb file).

Error for a vertex in NE direction

Error in E (m)	Error in N (m)
0.2	0.7

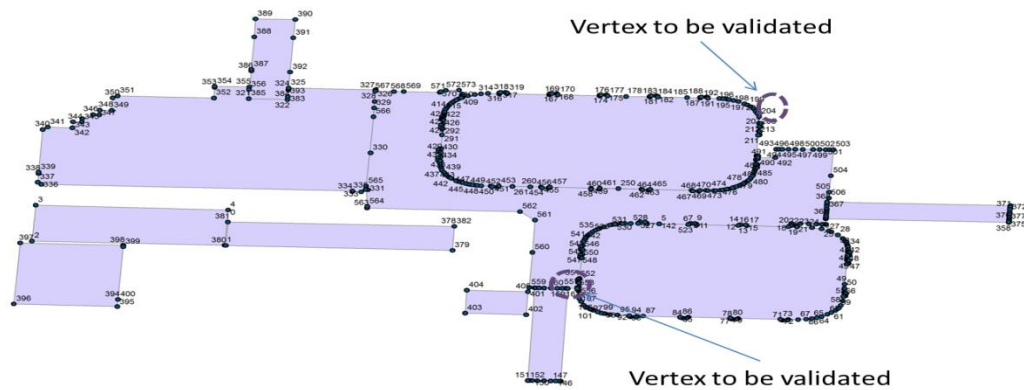
After analyzing three different vertices of Calgary Tower with same vertices from GDB file it was observed that the OBJ file is accurate within metres. Maximum error of 1.2 metres in E and N direction was observed.

Husky Oil Corporation building

Below is a jpg image of Husky Oil Corporation building obtained from gdb file using ArcGIS.

The numbers indicate the vertices ID. Each ID is associated with Lat Long in a file exported using ArcGIS.

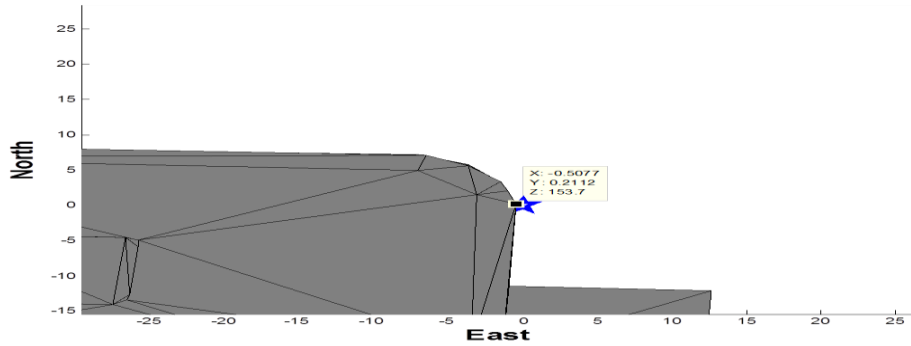
Validation of vertex in E direction



Husky building's vertices from gdb file. Vertex ID 204 in E direction is used as reference in this case for validation of corresponding vertex from OBJ file

Lat Long for vertex ID 204

Lat	Long	Vertex ID
51.045764	-114.076797	204

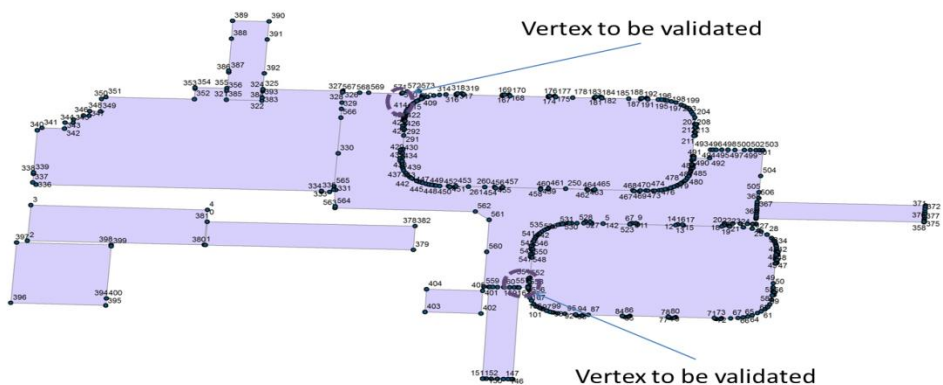


Husky building's vertices obtained from OBJ file. The blue star indicates the reference point (vertex ID 204 from gdb file). The marker indicates the corresponding point in OBJ file for vertex ID 204 (of gdb file).

Error for a vertex in E direction

Error in E (m)	Error in N (m)
0.6	0.2

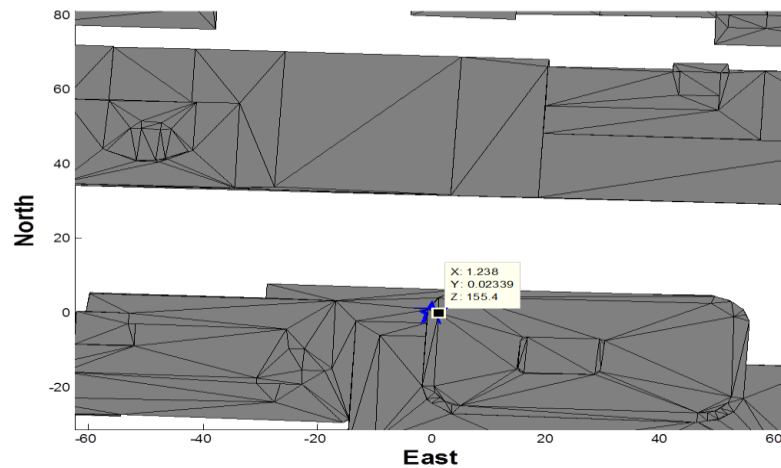
Validation of vertex in W direction



Husky building's vertices from gdb file. Vertex ID 414 in W direction is used as reference in this case for validation of corresponding vertex from OBJ file

Lat Long for vertex ID 414

Lat	Long	Vertex ID
51.045786	-114.077597	414



Husky building's vertices obtained from OBJ file. The blue star indicates the reference point (vertex ID 414 from gdb file). The marker indicates the corresponding point in OBJ file for vertex ID 414 (of gdb file).

Error for a vertex in E direction

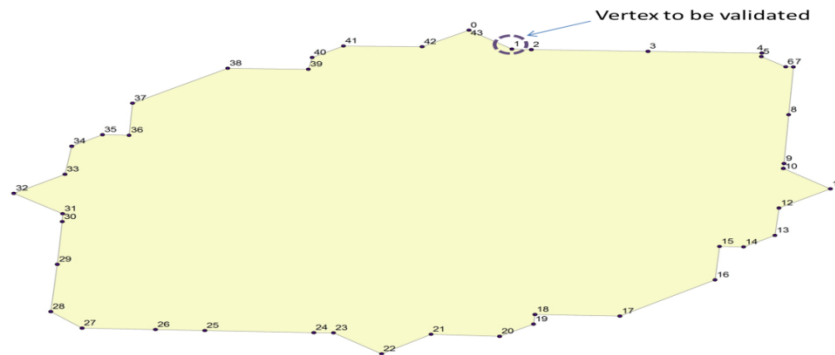
Error in E (m)	Error in N (m)
1.2	0

After analyzing two different vertices of Husky Tower with same vertices from GDB file it was observed that the OBJ file is accurate within metres. Maximum error of 1.2 metres in E and 20 cms in N direction was observed.

Devon Tower

Below is a jpg image of Devon tower obtained from gdb file using ArcGIS. The numbers indicate the vertices ID. Each ID is associated with Lat Long in a file exported using ArcGIS.

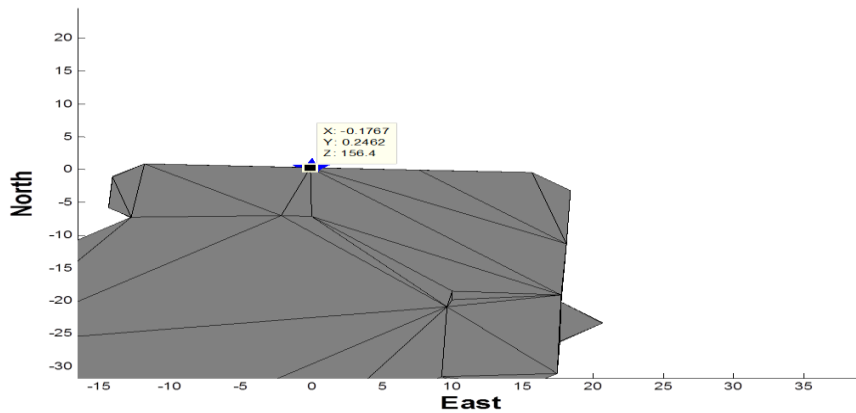
Validation of vertex in N direction



Devon tower's vertices from gdb file. Vertex ID 1 in N direction is used as reference in this case for validation of corresponding vertex from OBJ file

Lat Long for vertex ID 1

Lat	Long	Vertex ID
51.051263	-114.070746	1

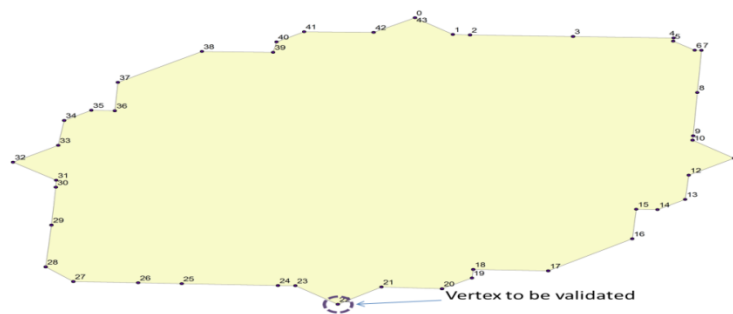


Husky building's vertices obtained from OBJ file. The blue star indicates the reference point (vertex ID 1 from gdb file). The marker indicates the corresponding point in OBJ file for vertex ID 1 (of gdb file).

Error for a vertex in E direction

Error in E (m)	Error in N (m)
0.2	0.2

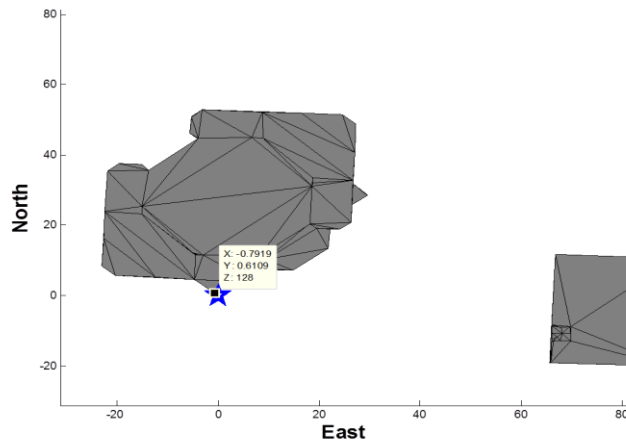
Validation of vertex in S direction



Devon tower's vertices from gdb file. Vertex ID 22 in S direction is used as reference in this case for validation of corresponding vertex from OBJ file

Lat Long for vertex ID 22

Lat	Long	Vertex ID
51.050767	-114.070831	22

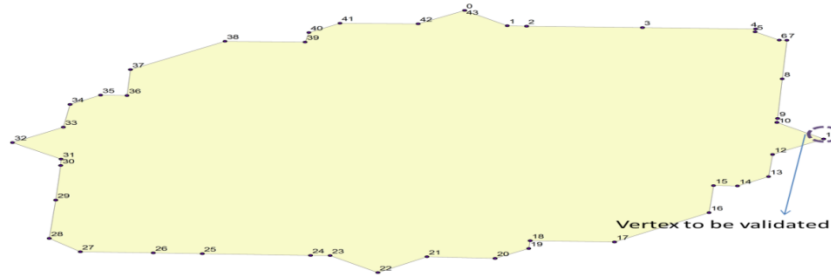


Husky building's vertices obtained from OBJ file. The blue star indicates the reference point (vertex ID 22 from gdb file). The marker indicates the corresponding point in OBJ file for vertex ID 22 (of gdb file).

Table: Error for a vertex in S direction

Error in E (m)	Error in N (m)
0.8	0.6

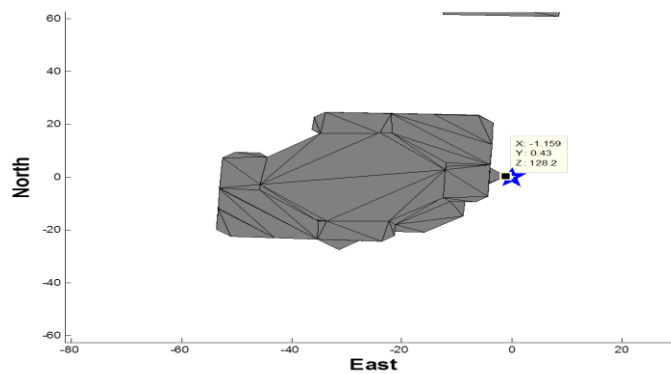
Validation of vertex in E direction



Devon tower's vertices from gdb file. Vertex ID 11 in S direction is used as reference in this case for validation of corresponding vertex from OBJ file

Lat Long for vertex ID 11

Lat	Long	Vertex ID
51.05102	-114.070393	11

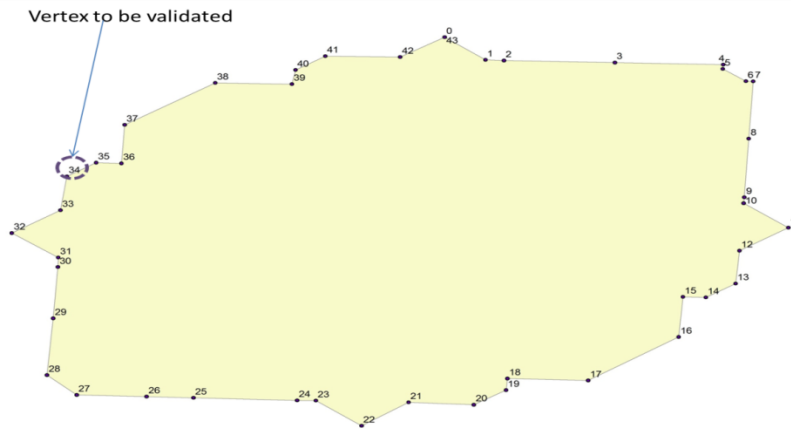


Husky building's vertices obtained from OBJ file. The blue star indicates the reference point (vertex ID 11 from gdb file). The marker indicates the corresponding point in OBJ file for vertex ID 11 (of gdb file).

Error for a vertex in S direction

Error in E (m)	Error in N (m)
1.1	0.4

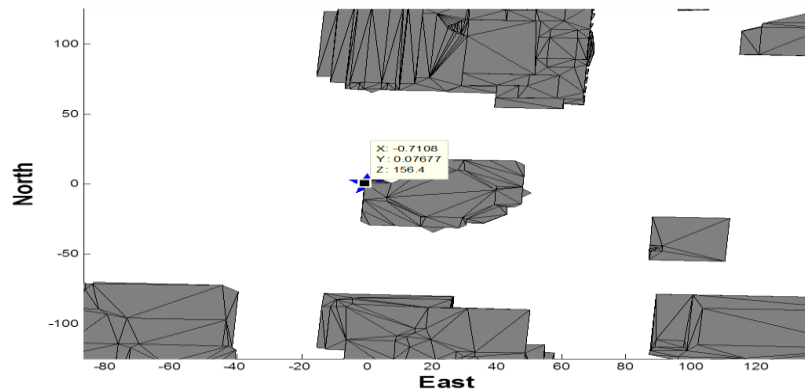
Validation of vertex in W direction



Devon tower's vertices from gdb file. Vertex ID 34 in W direction is used as reference in this case for validation of corresponding vertex from OBJ file

Lat Long for vertex ID 34

Lat	Long	Vertex ID
51.051085	-114.071134	34



Husky building's vertices obtained from OBJ file. The blue star indicates the reference point (vertex ID 34 from gdb file). The marker indicates the corresponding point in OBJ file for vertex ID 34 (of gdb file).

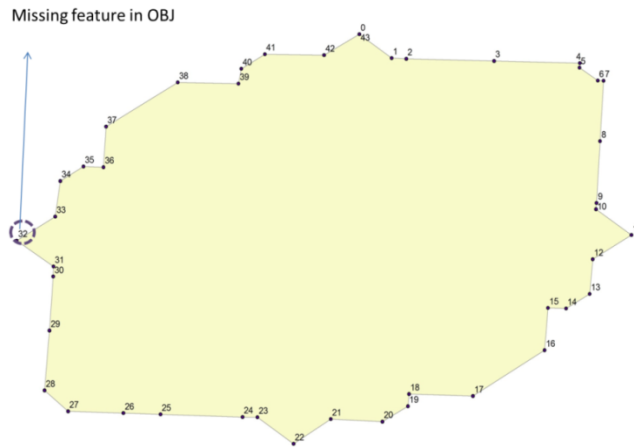
Error for a vertex in S direction

Error in E (m)	Error in N (m)
0.7	0.1

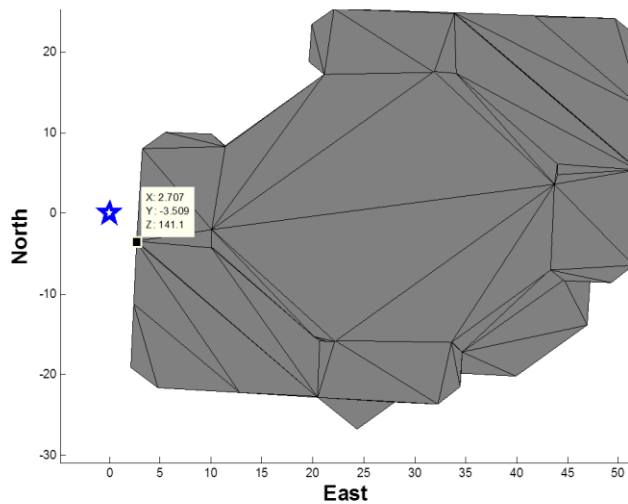
After analyzing four different vertices of Devon Tower with same vertices from GDB file it was observed that the OBJ file is accurate within metres. Maximum error of 1.1 metres in E and 60 cm in N direction was observed.

Missing Features in OBJ file

It is hard to provide any conclusion about error due to missing feature. The error would depend on how many and how large is the feature missing. However, just to give a feel of the error one missing feature from OBJ file is analyzed here.



Devon tower's vertices from gdb file.



Devon tower's vertices from gdb file. Vertex ID 32 is missing in OBJ file.

In this case the missing feature (vertex ID 32 from GDB file) is 2.7 m (E) and 3.5 m (N) away from nearest vertex in OBJ file.

Summary of errors in OBJ file

The table below summarizes the errors in vertices of OBJ file. As mentioned above validation was done only for those vertices which were present in OBJ and GDB files. Hence errors

summarized below correspond to those vertices which are common to both the files (OBJ and GDB).

Building	Vertex location	Error in E (m)	Error in N (m)
Calgary Tower	N	1.2	1.2
	SW	1.0	0.7
	NE	0.2	0.7
Husky Tower	E	0.6	0.2
	W	1.2	0
Devon Tower	N	0.2	0.2
	S	0.8	0.6
	E	1.1	0.4
	W	0.7	0.1

Summary of Validation:

The results presented here were based on those vertices which were present in OBJ and GDB files both. Based on the results presented here it is obvious that the accuracy of the OBJ file is approximately a meter. It was also observed that the accuracy of the OBJ model was better in the N-S direction as compared to the E-W direction. Maximum error of 1.2 metres was observed in the N and E direction. It was observed that there were missing features in the OBJ file. In general, it is hard to tell the error due to missing features, however, a typical example showed an error of 2.7 m and 3.5 m in the E and N direction.